

Earthquake Scaling, Simulation and Forecasting

By

MICHAEL KARL SACHS

B.A. (Virginia Commonwealth University) 1995
Undergraduate Physics (Columbia University) 2007

DISSERTATION

Submitted in partial satisfaction of the requirements for the degree of

DOCTOR OF PHILOSOPHY

in

Physics

in the

OFFICE OF GRADUATE STUDIES

of the

UNIVERSITY OF CALIFORNIA

DAVIS

Approved:

John Rundle, Chair

Donald Turcotte

James Crutchfield

Committee in Charge

2013

Copyright © 2013 by
Michael Karl Sachs
All rights reserved.

*To Amanda: I wish you were here to see both of your smart-ass brothers get
their PhDs.*

*To Adrienne, who, when I said I wanted to quit my secure, well-paying career to
spend the better part of my thirties learning physics, said yes; without even
batting an eye.*

CONTENTS

List of Figures	v
List of Tables	xiii
Abstract	xiv
Acknowledgments	xvi
1 Introduction	1
2 Scaling in Complex Systems	6
2.1 Introduction	7
2.2 Models	8
2.2.1 Slider-block model	8
2.2.2 Forest-fire model	10
2.2.3 Sandpile model	12
2.3 Natural Systems	13
2.3.1 Global seismicity	13
2.3.2 Characteristic earthquakes	15
2.3.3 Volcanic eruptions	21
2.3.4 Wildfires	24
2.3.5 Landslides	25
2.3.6 Floods	26
2.4 Discussion	29
3 Virtual California	32
3.1 Introduction	32
3.2 Ensemble-Domain Verses Time-Domain Simulations	34
3.3 Components of Virtual California	35
3.3.1 Fault Model	36
3.3.2 Element Stress Interactions	38

3.3.3	Event Model	40
3.4	Simulation Computational Overview	44
3.5	Virtual California Simulations	47
3.6	Virtual California on the Web	57
3.7	Conclusion	57
4	Forecast Verification	62
4.1	Introduction	62
4.2	RELM test	65
4.3	The Earthquakes	67
4.4	Submitted Forecasts	72
4.5	Evaluation of Results	76
4.6	Distribution of Cell Probabilities	79
4.7	Discussion	82
4.8	Conclusion	84
4.9	Glossary	84

LIST OF FIGURES

1.1	The destruction caused by the magnitude 9.0 Tōhoku earthquake in Minato Japan. Photo courtesy Wikipedia Commons.	2
1.2	The view from Union Square down Stockton street after the magnitude 7.9 1906 San Francisco earthquake. Photo courtesy Wikipedia Commons.	3
2.1	Illustration of the one-dimensional slider-block model. A linear array of N blocks of mass m are pulled along a surface by a constant velocity V_L loader plate. The loader plate is connected to each block with a loader spring with spring constant k_L and adjacent blocks are connected by springs with spring constant k_C . The frictional resisting forces are F_1, F_2, \dots, F_N	8
2.2	Frequency-size distribution of 10,000 slip events for a “stiff” system with $\alpha = 1000$. The ratio of the number of events N_L of event size L to the total number of events N_T is given as a function of L . The solid line is a power-law dependence with exponent -2.12 . System-wide ($L = 10^2$) dragon-king events are clearly illustrated.	9
2.3	Noncumulative frequency-area distributions for the forest-fire model [1]. The number of fires N_F with area A_F is given. Results are given for sparking frequencies $f_s = 1/125, 1/500, 1/2000$	11
2.4	Noncumulative frequency-area distribution of avalanches for the sandpile model. The number of avalanches N_L with area (number of boxes) A_L is given. The best-fit power-law correlation is given.	13

2.5	Cumulative number of global earthquakes N with magnitude greater than m_w are given as a function of moment magnitudes m_w . Observed values for the period January 1, 1977 to September 30, 2010 are obtained from the global CMT catalog, values for the period October 1, 2010 to August 15, 2011 are obtained from the ANSS catalog. The least-squares best fit of Equation 2.2 to the values in the range $5.5 \leq m_w \leq 7.5$ is given taking $a = 9.643$ and $b = 0.996$. Also included are the 2004 $m_w = 9.0$ Sumatra earthquake and the 2011 $m_w = 9.1$ Tōhoku earthquake.	16
2.6	Seismicity in central California for the period 28 September, 1999 to 28 September 2009. The aftershocks of the 18 September, 2004 Parkfield earthquake are shown in the red elliptical area. Aftershocks of the 2004 San Simeon earthquake and residual aftershocks of the 1983 Coalinga earthquake are clearly seen to the south-west and north-east of the study region.	19
2.7	Cumulative number of earthquakes with magnitude greater than m as a function of m for the Parkfield earthquake cycle 1972 to 2009. The best-fit scaling from Equation 2.4 is also shown. The $m = 5.95$ Parkfield earthquake is shown as a dragon king.	21
2.8	Cumulative number of volcanic eruptions N_c during the period 1800-2002 with dense rock equivalent volume greater than V_{DRE} as a function of V_{DRE} . The best-fit power-law scaling from Equation 2.5 is also shown along with the Toba eruption (red star). . .	23
2.9	Frequency-area statistics for 7,422 wildfires on United States Forest Service lands in California for the period 1970-2006 [2]. The frequency densities $\Delta N_F / \Delta A_F$ are given as a function of burned area A_F . Also shown is the best least-square power-law fit to the data.	25

2.10 Frequency-area statistics for three landslide inventories [3]: (1) 11,111 landslides triggered by the Northridge earthquake, (2) 4,237 landslides triggered by a snowmelt event Italy, (3) 9594 landslides triggered by Hurricane Mitch. The probability density p is given as a function of landslide area A_L . Also shown is the least-squares best-fit gamma distribution.	27
2.11 Dependance of the maximum daily discharge Q associated with time period T for the Colorado River in the Grand Canyon, Arizona [4]. The annual and partial duration flood series at the Lees Ferry gauging station for the water years 1921-1962 are shown. The least-squares power-law fit to the partial duration series and the LP3 fit to the annual series are also given. Points A and B are estimates of two paleo-floods [5].	30
3.1 An illustration of the differences between an actual fault and a back-slip fault. Each image is a view from above of a surface surrounding a fault (which is represented by the gray vertical line in each image). The horizontal lines show the deformation of the surface as forces are applied. Top The earthquake cycle on an actual fault. Bottom The earthquake cycle on a back-slip fault.	35
3.2 Top The ALLCAL2 model used in Virtual California. This particular model is based on the UCERF2 [6] fault model. The section indicated in the image is the creeping section of the San Andreas fault. This section tends to generate a large number of events and was removed from the model in order to speed up the simulation. Bottom A detail view of the Los Angeles area. In both images the meshed fault sections are rendered directly above their actual locations beneath the surface.	37
3.3 The shear and normal greens matrices for the two sections of the Hayward fault from the ALLCAL2 model described in Section 3.3.1.	39

3.4	The σ_{xy} component of the stress tensor generated by a $1\text{km} \times 1\text{km}$ element slipping 10m in the direction indicated by the arrows (right-lateral). Left View of the stress field from above. Right View of the stress field from the side.	40
3.5	Top The CFF for each of the 48 elements that make up the Park-field section of the San Andreas fault. Drops in the CFF correspond to events. Large events are characterized by many elements undergoing large CFF drops. Bottom The sweeps that make up the event at $t = 593.187$. The element that triggers the event is in bold. The initial failure triggers a cascade that results in all elements failing.	43
3.6	Examples of how varying dynamic-triggering η (Equation 3.6) effects Virtual California output. The observed values in the top-left frame are taken from UCERF2 [6]. The observed values in the remaining frames are taken from Wells and Coppersmith (W&C) [7].	45
3.7	Examples of how varying the slip-scaling threshold S_t (Equation 3.5) effects Virtual California output. The observed values in the top-left frame are taken from UCERF2 [6]. The observed values in the remaining frames are taken from Wells and Coppersmith (W&C) [7].	46
3.8	Execution flow of Virtual California on a parallel system.	47
3.9	The total slip on each element that ruptured in a simulated $m \simeq 7.669$ event on the northern portion of the San Andreas fault. The trigger fault is the thick line in the map in the upper right hand corner of the figure.	48
3.10	The surface displacement caused by the simulated $m \simeq 7.669$ event shown in Figure 3.9. The direction of the plotted displacement is shown in the upper right-hand corner of the figure. The direction is roughly looking north along the fault trace at surface level.	49

3.11 The surface displacement caused by the simulated $m \simeq 7.669$ event shown in Figure 3.9 plotted as interference fringes. This is a simulated InSAR interferogram. The direction of the plotted displacement is shown in the upper right-hand corner of the figure. The direction is roughly looking north along the fault trace at surface level.	50
3.12 Histogram of event magnitude by fault section. The fault model used is the ALLCAL2 model described in Section 3.3.1. The simulation was run for 50,000 years with dynamic triggering $\eta = 0.8$ and slip-scaling threshold $S_t = 10$. The first and last 10,000 years were discarded leaving 30,000 years of events.	52
3.13 Left Histogram of average slip for events in a simulation of the ALLCAL2 model described in Section 3.3.1. The simulation was run for 50,000 years with dynamic triggering $\eta = 0.8$ and slip-scaling threshold $S_t = 10$. The first and last 10,000 years were discarded leaving 30,000 years of events. Top left All events. Bottom left Events that involved 10 or more elements. Right Histogram of fault areas for all fault sections in the ALLCAL2 model.	53
3.14 Space-time diagram of 500 years of activity on the San Andreas fault. The fault model used is the ALLCAL2 model described in Section 3.3.1. The simulation was run for 50,000 years with dynamic triggering $\eta = 0.8$ and slip-scaling threshold $S_t = 10$. The first and last 10,000 years were discarded leaving 30,000 years of events. This particular 500 years was selected because of the $m = 7.985$ event on the southern San Andreas at year 41384 (marked with the arrow). This is the largest event in the simulation.	54

3.15 Scaling relations from a Virtual California simulation of the ALL-CAL2 model described in Section 3.3.1. The simulation was run for 50,000 years with dynamic triggering $\eta = 0.8$ and slip-scaling threshold $S_t = 10$. The first and last 10,000 years were discarded leaving 30,000 years of events. In the figures, W&C are observed relations as reported by Wells and Coppersmith [7], and K&A are theoretical relationships as reported by Kanamori and Anderson [8]. UCERF2 are observations of seismicity in California as reported by Field et al. [6]. The scaling relationships are: top left frequency-magnitude, top right average slip-surface rupture length, bottom left magnitude-average slip, and bottom right magnitude-rupture area. In all of the plots except the frequency-magnitude plot, the heavy dark line is a binned average of the Virtual California events.	55
3.16 Observed recurrence intervals compared to simulated recurrence intervals for the ALLCAL2 model described in Section 3.3.1. The simulation was run for 50,000 years with dynamic triggering $\eta = 0.8$ and slip-scaling threshold $S_t = 10$. The first and last 10,000 years were discarded leaving 30,000 years of events. The observed intervals are taken from a compilation of observations in [6].	58
3.17 The user interaction diagram showing the functionality of the Virtual California Web Interface.	59
3.18 The fault view from the Virtual California Web Interface.	60
3.19 The list view from the Virtual California Web Interface.	61
4.1 Map of the test region, the coast of California, major faults, and the 31 earthquakes with $M \geq 4.95$ that occurred in the test region. The earthquakes are listed in Table 4.1. Also shown are the square regions where large scale maps are given in Figures 4.2 to 4.4.	69

4.2 Map of the southeast region around the epicenter of the $M = 7.2$ El Mayor-Cucapah earthquake that occurred on 4 April 2010 (event #22 in Table 4.1, shown as a star). (a) Earthquakes during the period 1 January 2006 through 3 April 2010. (b) Earthquakes during the period 4 April 2010 through 31 December 2010 (includes aftershocks). Included are the test earthquakes given in Table 4.1 as well as background earthquakes with $M \geq 2.0$. More details in the square region are given in the larger scale maps in Figure 4.3. . .	70
4.3 Map of the region in the immediate vicinity of the epicenter of the $M = 7.2$ El Mayor-Cucapah earthquake. (a) Earthquakes during the period 1 January 2006 through 3 April 2010. (b) Earthquakes during the period 4 April 2010 through 31 December 2010. Included are the test earthquakes given in Table 4.1 as well as background earthquakes with $M \geq 2.0$. The association of lettered $0.1^\circ \times 0.1^\circ$ cells in which earthquakes occurred with the numbered earthquakes is illustrated.	71
4.4 Map of the northwest region near Cape Mendocino. Test earthquakes given in Table 4.1 are shown as well as background earthquakes with $M \geq 2.0$	72
4.5 Distribution of forecast probabilities λ_{ei} that an earthquake with $m \geq 4.95$ will occur in cell i . The 7682 forecast cell probabilities are ranked from highest to lowest. In each forecast the sum of the probabilities is unity. The no skill forecast λ_{emi}^{rand} is also included. . .	80

LIST OF TABLES

4.1 Times of occurrence, locations, and magnitudes of the 31 earthquakes in the test region with $M \geq 4.95$ from 1 January 2006 until 31 December 2010. The $M = 7.2$ El Mayor-Cucapah earthquake is in bold.	67
4.2 Values of the submitted conditional probabilities λ_{emi} that an earthquake that has a magnitude in magnitude bin m will occur in spatial cell i . Values are given for the 31 test earthquakes listed in Table 4.1. The first column is the magnitude bin m , the second column is the spatial cell i , and the third column is the earthquake number. Forecast conditional probabilities λ_{emi} are given for 13 forecasts. These are Bird and Liu [9] (B-L), Ebel et al. [10] main shocks+aftershocks (Ebel) and main shock only (Ebel ms), Helmstetter et al. [11] main shocks+aftershocks (Helm) and main shock only (Helm ms), Holliday et al. [12] (Holl), Ward [13] seismic model with $M_{max} = 8.1$ (Ward seis.), Ward geologic model with $M_{max} = 8.1$ (Ward geol.), Ward geodetic model with $M_{max} = 8.1$ (Ward geod.), Ward combined model with $M_{max} = 8.1$ (Ward combo), Ward geodetic model with $M_{max} = 8.5$ (Ward geod. 8.5), Ward simulation model (Ward sim.), Wiemer and Schorlemmer [14] (W-S). The highest (best) forecast probabilities are in bold. The number of winning forecasts and the mean forecast probabilities for all test earthquakes $\bar{\lambda}_{emi}$ are given for each forecast. Also given are the total number of earthquakes forecast N_e .	75

ABSTRACT OF THE DISSERTATION

Earthquake Scaling, Simulation and Forecasting

Earthquakes are among the most devastating natural events faced by society. In 2011, just two events, the magnitude 6.3 earthquake in Christchurch New Zealand on February 22, and the magnitude 9.0 Tōhoku earthquake off the coast of Japan on March 11, caused a combined total of \$226 billion in economic losses [15]. Over the last decade, 791,721 deaths were caused by earthquakes [16]. Yet, despite their impact, our ability to accurately predict when earthquakes will occur is limited. This is due, in large part, to the fact that the fault systems that produce earthquakes are non-linear. The result being that very small differences in the systems now result in very big differences in the future, making forecasting difficult. In spite of this, there are patterns that exist in earthquake data. These patterns are often in the form of frequency-magnitude scaling relations that relate the number of smaller events observed to the number of larger events observed. In many cases these scaling relations show consistent behavior over a wide range of scales. This consistency forms the basis of most forecasting techniques. However, the utility of these scaling relations is limited by the size of the earthquake catalogs which, especially in the case of large events, are fairly small and limited to a few 100 years of events.

In this dissertation I discuss three areas of earthquake science. The first is an overview of scaling behavior in a variety of complex systems, both models and natural systems. The focus of this area is to understand how this scaling behavior breaks down. The second is a description of the development and testing of an earthquake simulator called Virtual California designed to extend the observed catalog of earthquakes in California. This simulator uses novel techniques borrowed from statistical physics to enable the modeling of large fault systems over long periods of time. The third is an evaluation of existing earthquake forecasts, which focusses on the the Regional Earthquake Likelihood Models (RELM) test: the first

competitive test of earthquake forecasts in California.

ACKNOWLEDGMENTS

First and foremost I would like to thank my partner Adrienne Capps. I really couldn't have done this without her. I would also like to thank my family. Mom and Dad for raising me in an environment where curiosity and creativity were encouraged. My brother and sister, Patrick and Amanda, for keeping me on my toes when I was young and for being my friends now that we are older.

Next I would like to thank my academic collaborators. My advisor John Rundle for giving me so many great opportunities and also for being a great advocate. Don Turcotte for being so approachable and generous with his time. I really lucked out getting to work with two excellent scientists like John and Don. I also would like to thank the other members of my research group: James Holliday, Joe Gran, Mark Yoder, Quinn Norris and Eric Heien. It's easy to succeed when you are surrounded by so many brilliant people!

Finally I would like to thank the co-authors of the publications collected here. For the work presented in Chapter 2: Mark Yoder, Don Turcotte, John Rundle, Bruce Malamud, James Holliday, Joe Gran, and Bill Graves. Chapter 3: Eric Heien, Don Turcotte, Mehmet Yikilmaz, John Rundle and Louise Kellogg. Chapter 4: Don Turcotte, Ya-Ting Lee, James Holliday, John Rundle, Chien-Chih Chen, and Kristy Tiampo. I have learned so much from these collaborations, not the least of which is that good science is the product of many hands.

Chapter 1

Introduction

Earthquakes are among the most devastating natural events faced by society. In 2011 the damage resulting from earthquakes accounted for 59% of world wide economic losses due to natural disasters [17]. The magnitude 9.0 Tōhoku earthquake off the coast of Japan on March 11, 2011 caused approximately \$210 billion in damages and killed approximately 16,000 people [15]. Over the past decade events in the Indian Ocean on December 26, 2004 and Haiti on January 12, 2010 caused enormous devastation, totaling roughly 543,898 deaths [18] and \$21.8 billion [19, 20] in economic losses. Overall the deaths caused by earthquakes over the last decade is estimated at 791,721 [16]. A repeat of the magnitude 7.9 1906 San Francisco earthquake could cause as much as \$84 billion in damages [21] which would give this event the dubious distinction of being the third most costly natural disaster ever recorded, beating out Hurricane Katrina.

Aside from the destruction caused by earthquakes, they are also interesting phenomena in their own right. The largest earthquake ever recorded, the 1960, magnitude 9.5 Chilean earthquake released 2.24×10^{23} joules of energy or 5.35×10^7 megatons of TNT. This is $\sim 10,000$ times the destructive power of the world nuclear arsenal and $\sim 56\%$ the energy released in the Chicxulub impact which is thought to be responsible for the Cretaceous-Paleogene extinction [22]. The Tōhoku earthquake released enough energy to slow down the earth's rotation, shortening the length of the day by 1.8 microseconds [23]. Indeed, earthquakes are



Figure 1.1: The destruction caused by the magnitude 9.0 Tōhoku earthquake in Minato Japan. Photo courtesy Wikipedia Commons.

among the most energetic natural events that can be studied at close remove.

Clearly, a better understanding of earthquakes is important. However, earthquakes have a wide range of scales – from seconds to thousands of years in the time domain, and from microscopic to global spatially – a characteristic of non-linear complex systems. These systems often exhibit deterministic chaos – very small fluctuations in the initial state of the system result in very different evolution – making reliable forecasting difficult. This range of scales, and the inaccessibility of the sources of earthquakes, also makes collecting reliable data difficult. Up until recently the best data were a list of recorded events – the earthquake catalog – that consists of times, locations and magnitudes. This was supplemented by a much smaller catalog of historical events that were not directly recorded but were inferred by geologic evidence (the paleoseismic catalog). Starting a few decades ago this catalog data began to be supplemented by ground deformation data collected by GPS arrays and radar interferograms. Currently there are still many gaps and



Figure 1.2: The view from Union Square down Stockton street after the magnitude 7.9 1906 San Francisco earthquake. Photo courtesy Wikipedia Commons.

inconsistencies in this new data, however over the next decade or so the quality and quantity of this new data will continue to increase.

The time where the study of earthquakes becomes a data-rich science is quickly approaching. This deluge of data will necessitate new models and innovative approaches to studying earthquake phenomena. In some ways, the study of earthquakes is currently in the state that cosmology was before the Kobe and WMAP microwave background data became available. That data changed our understanding of the evolution of the universe and challenged many theoretical assumptions. The theoretical basis for earthquake science is many decades old, and based on old data and methods. New ideas are emerging that borrow heavily from the study of phase transitions and nucleation in statistical physics. These approaches model faults as systems in a critical state – much like the critical point in water. At the

correct temperature and pressure water exists in a strange mix of vapor and liquid, with fluctuations between the two occurring over a wide range of scales. This self-similarity is the hallmark of systems at their critical point and is similar to the power-law scaling seen in the relationship between small and large earthquakes.

With the connection to statistical physics, come a host of new modeling techniques. Sometimes called “ensemble-domain” models, these techniques attempt to explore probable states of physical systems instead of explicitly calculating their time evolution. The Metropolis algorithm [24] is an example of this. There is often a computational advantage to these models. Because they don’t try to solve sets of linked differential equations – the “time-domain” approach – these models can simulate very large systems and explore a very large number of states. The ensemble-domain approach also has the advantage of not relying on a precise definition of initial conditions, which for complex systems like earthquake faults can be extremely difficult.

Using an ensemble-domain model, large systems of faults can be simulated with only basic data about the current state of the system. These simulations produce many thousands of years of events, providing a rich dataset from which to explore the statistics of the fault systems. These data can be used to explore theoretical questions about the dynamics of fault systems (for example [25–28]) but also to develop better forecasting techniques.

In California, the need for better earthquake forecasting is critical. The official California earthquake hazard report is the Uniform California Earthquake Rupture Forecast (UCERF). This report is produced by the Working Group on California Earthquake Probabilities which is a collaboration between the U.S. Geological Survey, California Geological Survey, and the Southern California Earthquake Center. The results of this report are used in many areas ranging from building codes to disaster preparedness to earthquake insurance rates. In its current version, UCERF2 [6], the report is based to a large degree on expert opinion. However, in future versions computer simulations will play an increasingly important role. It is hoped

that by studying the output of these simulations the role of expert opinion can be reduced and a more systematic approach to forecasting can be developed.

The work that I present here focusses on three areas of earthquake science compiled from 11 papers published over the last three years. In Chapter 2, I discuss scaling behavior in complex systems and where this behavior breaks down. Chapter 3 describes the development of a working earthquake simulator – called Virtual California – that reproduces observed seismicity yet also extends the observed catalog of events. Chapter 4 is concerned with earthquake forecasting and forecast verification.

Chapter 2

Scaling in Complex Systems

Many complex systems exhibit power-law scaling behavior. This type of behavior is sometimes called scale-free because the observed properties of the system are the same over a wide range of scales of some variable (for example length or time). There is some debate about why these systems behave this way [29–32]. In many cases it can be argued that some underlying fractal structure gives rise to scale invariance [32]. In other cases a connection to phase transitions in statistical mechanics is cited as the cause [29].

Regardless of the reasons behind power-law scaling, the fact that these systems behave this way is a powerful predictive tool. Imagine a system where our observations are a count of events of varying sizes (the case with all of the systems described here). If this system behaves in a scale-free way, the number of events of one size will have a well defined relationship with the number of events of other sizes. So, even if we have no knowledge of the underlying processes that produce the events, we can predict that given a certain number of small events we can expect a certain number of large events.

Of course the utility of this approach is only valid if we know the system behaves this way at all relevant scales. The work presented in this chapter is a survey of many systems, both models and physical systems, that exhibit some form of power-law scaling. In many cases this scaling is preserved over all of the scales in the system. In some cases however, there are extreme events that occur

that do not follow from power-law scaling. This work was originally published in The European Physical Journal Special Topics [33] and in a book entitled “Self-Organized Criticality Systems” [34].

2.1 Introduction

The statistics of extreme events have been studied extensively [35]. Applications include floods, wars, financial crashes, and many others. Extreme events that change global society were characterized as black swans by Taleb [36]. The frequency-size distributions associated with many natural hazards satisfy power-law (fractal) statistics to a good approximation [37]. Examples include earthquakes, landslides, volcanic eruptions and wildfires. We will argue that floods also fit into this category. An important question in probabilistic hazard assessment is whether future extreme events can be forecast by extrapolating the power-law behavior.

In some cases small events satisfy power-law scaling but one or more extreme events are significantly larger than the extrapolation of the power-law scaling. Sornette [38] refers to this class of extreme events as dragon kings. Examples of dragon kings would be the population of London and Paris relative to the power-law distribution of the population of the other cities in the U.K. and France. Another example of dragon-king behavior is material fracture. When stress on a brittle material is increased there is often a power-law distribution of acoustic emissions before an unstable fracture propagates through the sample [39]. The precursory emissions are a nucleation process and the fracture can be classified as a phase change [40].

In this chapter we will address the question: Are dragon kings relevant to probabilistic hazard assessment? Our discussion will emphasize seismic hazard. On relatively large geographic scales the frequency-rupture-area statistics of earthquakes are well represented by power-law statistics even for the largest events. However, this behavior does not seem to be the case locally. On major faults, such as the San Andreas in California, seismic activity is dominated by great earthquakes, like

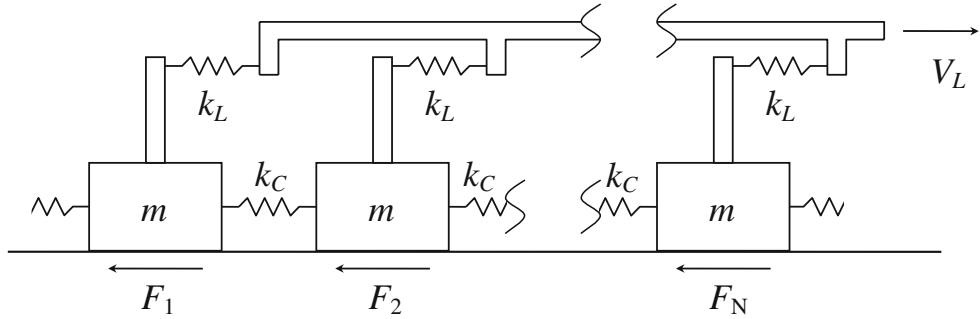


Figure 2.1: Illustration of the one-dimensional slider-block model. A linear array of N blocks of mass m are pulled along a surface by a constant velocity V_L loader plate. The loader plate is connected to each block with a loader spring with spring constant k_L and adjacent blocks are connected by springs with spring constant k_C . The frictional resisting forces are F_1, F_2, \dots, F_N .

the 1906 San Francisco earthquake. These are known as “characteristic” earthquakes and we will argue that characteristic earthquakes are dragon kings. As a specific example we will consider a characteristic earthquake cycle on the Park-field segment of the San Andreas fault. We will then consider in some detail the use of slider-block models to represent seismicity. We will show that dragon-king behavior can be generated by these models.

We will then extend our studies to volcanic eruptions, landslides, and wildfires. These exhibit power-law scaling and we will discuss their extrapolation to the largest events. The statistics of extreme floods have been the subject of many studies. We will discuss the extrapolation of small flood observations to large floods in some detail.

2.2 Models

2.2.1 Slider-block model

The multiple slider-block model has been proposed as a deterministic example of self-organized critical behavior [41]. This model had previously been proposed as a simple model of earthquake behavior [42]. Utilizing the multiple slider-block simulations of Abaimov et al. [43] we will demonstrate dragon-king behavior.

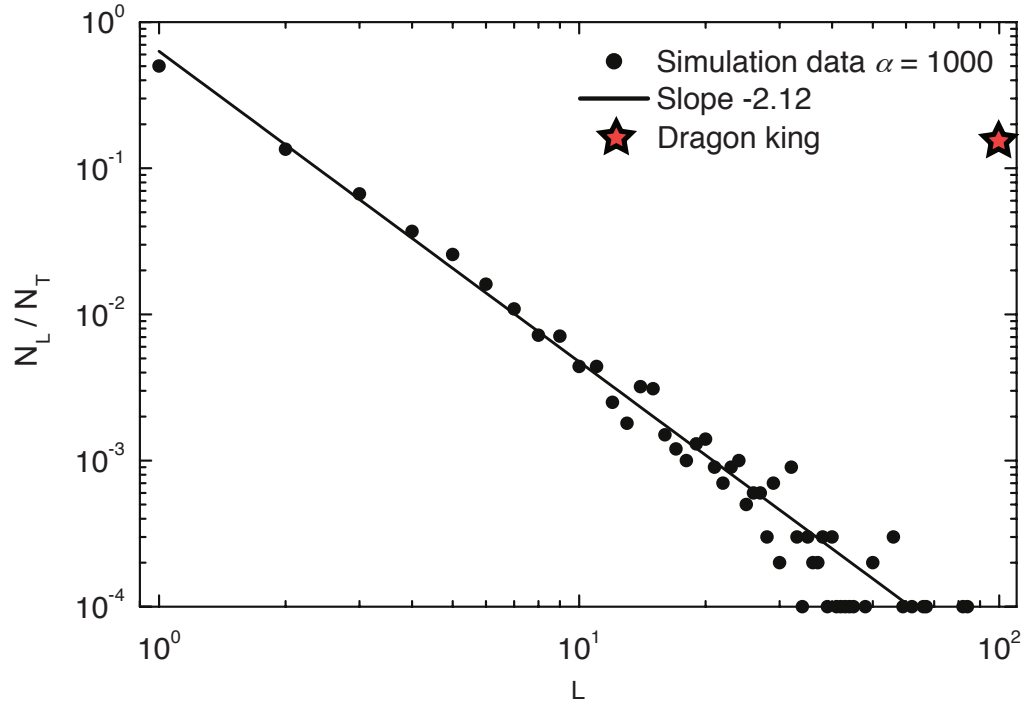


Figure 2.2: Frequency-size distribution of 10,000 slip events for a “stiff” system with $\alpha = 1000$. The ratio of the number of events N_L of event size L to the total number of events N_T is given as a function of L . The solid line is a power-law dependence with exponent -2.12 . System-wide ($L = 10^2$) dragon-king events are clearly illustrated.

A linear chain of 100 slider blocks was pulled over a surface at a constant velocity by a loader plate as illustrated in Figure 2.1. Each block is connected to the loader plate by a spring with spring constant k_L and adjacent blocks are connected to each other by springs with spring constant k_C . An important parameter in the problem is the ratio of spring constants $\alpha = k_C/k_L$. This is a measure of the stiffness of the system. The blocks interact with the surface through a static-dynamic friction law. With the static coefficient of friction larger than the dynamic (sliding) coefficient of friction, stick-slip behavior is observed. The size of a slip event is given by the number of blocks L that slip simultaneously in the event.

The stiffness α acts as a tuning parameter in this problem. For soft systems (small α) only small slip events occur, there is an exponential decay for larger slip events. As α is increased system wide ($L = 100$) events begin to occur. The

frequency-size distribution of the slip events for a stiff system ($\alpha = 1000$) is given in Figure 2.2. Statistics for 10,000 events are given and about 1,500 are system wide ($L = 100$) events. The small events are well approximated by the power-law relation

$$\frac{N_L}{N_T} = 0.8L^{-2.12}. \quad (2.1)$$

where N_L is the number of events with L blocks slipping and $N_T = 10,000$ is the total number of events. However, the large number of system wide events ($L = 100$) do not scale with the smaller events. The results are clearly an example of dragon-king behavior. The occurrence of the dragon kings is determined by the size of the system. They are not a finite-size effect in that they do not disappear as the system becomes very large. This behavior has been discussed for earthquakes and other systems [44, 45] and for epileptic seizures [46]. The system wide events are quite analogous to the characteristic earthquakes on a fault, again an effect related to system size.

2.2.2 Forest-fire model

The power-law scaling of wildfires is associated with the behavior of the forest-fire model [1]. The standard forest-fire model [47] consists of a square grid of sites. At each time step either a model tree or match is dropped on a randomly chosen site. A tree is “planted” only if the site is unoccupied. If a match is dropped on an occupied site, that tree and all adjacent trees “burn” and are removed from the grid. The governing parameter in this model is the firing frequency f_s : the fraction of time steps in which matches are dropped. If $f_s = 1/125$ there have been 124 attempts to plant trees before a match is dropped on the 125th time step. After specifying the size of the square grid N_G and the firing frequency f_s a simulation is run for N_S time steps. The number of trees that burn in model fires is determined. Taking $N_G = 16,384$ (128×128), $f_s = 1/125$, $1/500$, and $1/2000$ and $N_S = 10^9$ we plot the fraction of time steps on which fires of area A_F occur: N_F/N_S , against A_F in Figure 2.3.

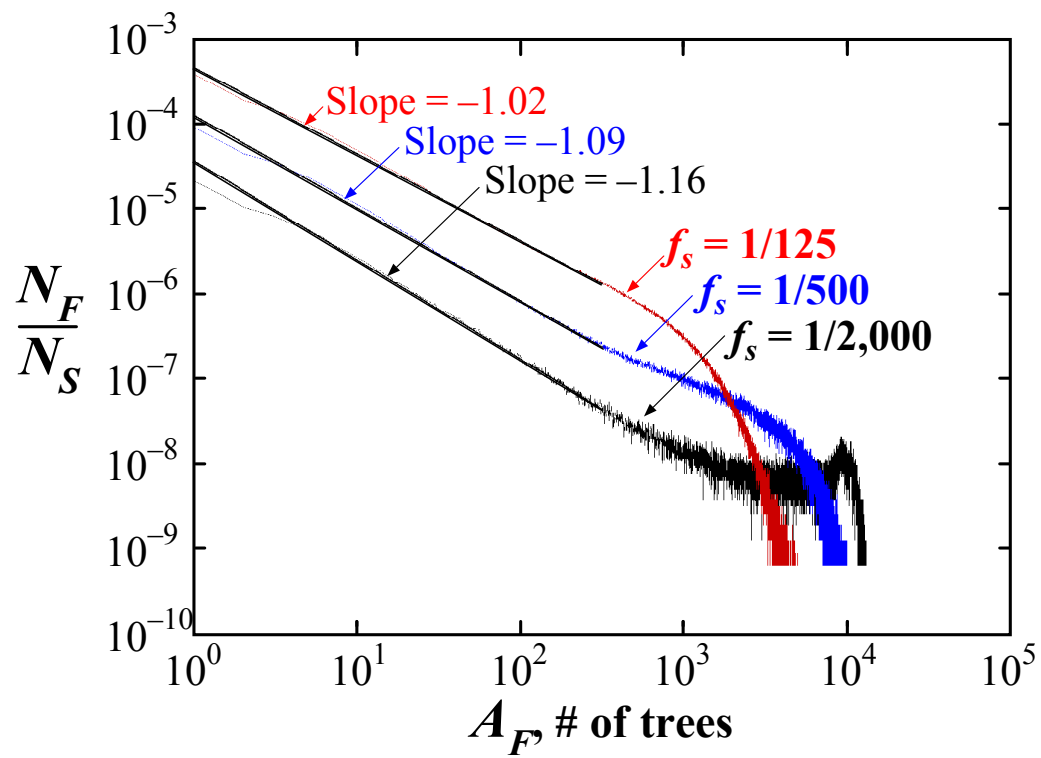


Figure 2.3: Noncumulative frequency-area distributions for the forest-fire model [1]. The number of fires N_F with area A_F is given. Results are given for sparking frequencies $f_s = 1/125, 1/500, 1/2000$.

The behavior of this model is very similar to the behavior of the slider-block model described above. The roles of the stiffness parameter α in the slider-block model and the firing frequency in the forest fire model are virtually identical. For large firing frequencies only small fires occur, there is an exponential decay for larger fires. As f_s is decreased fires begin to span the grid. They are an effect associated with the size of the grid of planting sites. For very small firing frequencies this behavior occurs in the forest-fire model just as in the slider-block model illustrated in Figure 2.2. In the limit of a near zero firing frequency all fires will burn all sites on the grid.

It is interesting to note that the data represented in Figure 2.9 shows evidence of neither roll over (high firing frequency) nor system size effects (low firing frequency) for fires in California. It is unclear at this time to what extent this is evidence of a dynamic effective firing frequency f_s , presumably related to regional fuel density and fire susceptibility in general, or simply an incomplete historical record. Frequency-area distributions of wildfires in Canada do, in fact, demonstrate large area truncation [48].

2.2.3 Sandpile model

The concept of self-organized criticality was originally based on the “sandpile” model proposed by Bak et al. [29]. In this model there is a square grid of boxes. At each time step a particle is dropped into a randomly selected box. When a box accumulates four particles they are redistributed to the four adjacent boxes, or in the case of edge boxes, are lost from the grid. These redistributions can lead to further instabilities and “avalanches” of particles are lost from the grid. A measure of the size of a model avalanche is the number of boxes (area) A_L that participate in an avalanche. The noncumulative frequency-area distribution of avalanches for a simulation on a 50×50 grid is given in Figure 2.4. Good agreement with a power-law distribution is obtained with an exponent of 1.03.

The behavior of the sandpile model illustrated in Figure 2.4 is quite different than the behavior of the slider-block and forest-fire models in Figures 2.2 and 2.3.

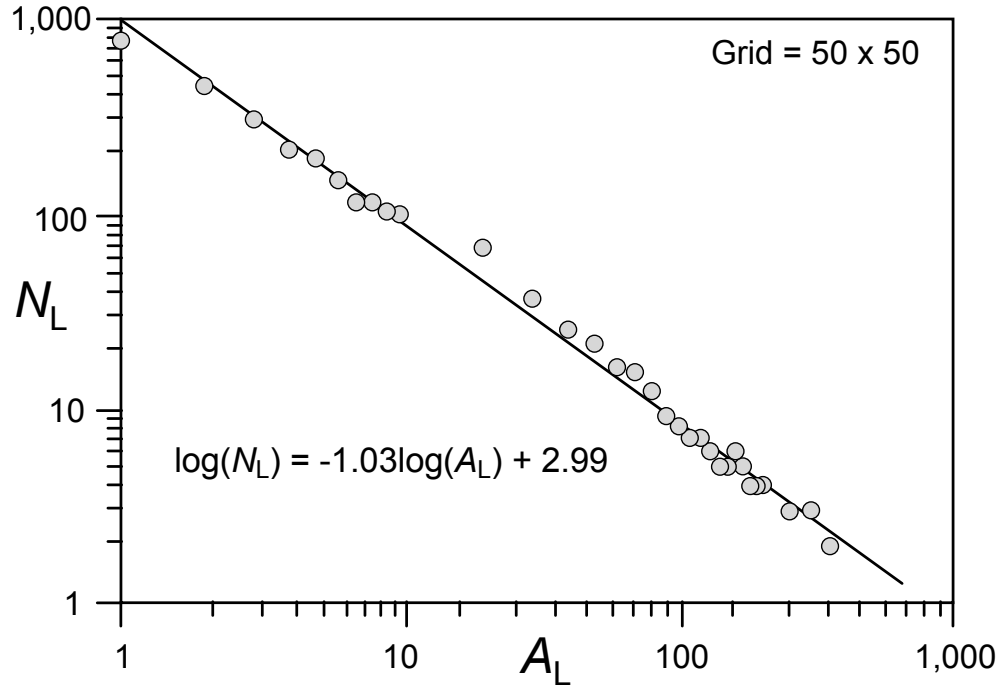


Figure 2.4: Noncumulative frequency-area distribution of avalanches for the sandpile model. The number of avalanches N_L with area (number of boxes) A_L is given. The best-fit power-law correlation is given.

The sandpile model does not have a tuning parameter. All three models exhibit power-law scaling with exponents near unity and thus all three are referred to as examples of self-organized criticality. However, the sandpile model, unlike the others, does not exhibit dragon-king behavior. This difference can be attributed to the lack of a tuning parameter. In the sandpile model the power-law behavior extends to the size of the grid. However, in the slider-block and forest-fire models the range of power-law behavior is a function of the value of the control parameter.

2.3 Natural Systems

2.3.1 Global seismicity

The frequency-magnitude statistics of earthquakes have been recognized to satisfy log-linear scaling both globally and regionally. It is accepted that earthquakes satisfy the Gutenberg-Richter (GR) scaling relation [49]

$$\log N_c = -bm + a. \quad (2.2)$$

where N_c is the cumulative number of earthquakes in a region and time interval with magnitudes greater than m . The scaling relation given in Equation 2.2 has been shown to be equivalent to a power-law scaling between N and A_r , the earthquake rupture area [37].

$$N_c = \alpha A_r^{-b}. \quad (2.3)$$

Thus earthquakes satisfy power-law scaling. Great earthquakes will be dragon kings if their magnitudes exceed significantly the extrapolated scaling relation given in Equation 2.3.

In this section we will consider global seismicity. Because of the many problems associated with the magnitudes of large earthquakes, the preferred approach to global seismicity is to use the Global Central Moment Tensor catalog (www.globalcmt.org) [50, 51]. We utilize this catalog for the period January 1, 1977 to September 30, 2010. In order to update our results through August 15, 2011 we use moment magnitudes given in the ANSS catalog (www.ncedc.org/cnss/). Using these catalogs the cumulative number of global earthquakes with magnitudes greater than m for the period 1977 to August 15, 2011 is given in Figure 2.5. The roll over for small magnitudes $m_w < 5.25$ is attributed to the sensitivity limit of the global network used to obtain moment magnitudes m_w [52]. The roll over for $m_w > 7.5$ is more controversial [53, 54]. It is usually attributed to the transition from small earthquakes with near equal lengths and depths to large earthquakes with lengths much larger than depths.

Included in Figure 2.5 is the least squares fit of Equation 2.2 to the data taking $a = 9.643$ and $b = 0.996$. The fit is carried out between $m = 5.6$ and 7.5 and includes some 30,000 earthquakes. Also included in Figure 2.5 are the $m_w = 9.0$ Sumatra earthquake on December 26, 2004 and the $m_w = 9.1$ Tōhoku (Japan) earthquake on March 11, 2011. These were the largest earthquakes during the

study period. The tsunami generated by the Sumatra earthquake killed some 230,000 people. The earthquake and tsunami generated by the Tōhoku earthquake killed some 22,000 people. In addition the tsunami resulted in a nuclear meltdown at the Fukushima I power plant. This meltdown created serious economic disruption in Japan and threatens to curtail the global use of nuclear power plants to reduce the emission of greenhouse gasses. The size and impact of the Sumatra and Tōhoku earthquakes clearly qualify them as black swans. However, since they lie below the extrapolation of the power-law scaling they are not dragon kings on a global scale. We will argue in the next section that earthquakes do exhibit dragon-king behavior on a regional scale.

2.3.2 Characteristic earthquakes

There are two limiting hypotheses for the behavior of faults. In the first, each fault (or fault segment) has a sequence of earthquakes that rupture the entire fault (or fault segment). The global GR (power-law, fractal) distribution of earthquakes illustrated in Figure 2.5 is attributed to a power-law (fractal) distribution of fault areas. Each fault has an earthquake with rupture area equal to the area of the fault. In seismology these are known as “characteristic” earthquakes. The other limiting hypothesis is that every fault has a GR distribution of earthquake magnitudes. The global GR scaling is the sum of the GR scaling on individual faults. The actual behavior of the earth lies between these two limits [55].

Ideally, observations would discriminate between the two limiting hypotheses. However, it is impossible to attribute smaller earthquakes to specific faults because only the largest faults can be mapped and identified. Also, location errors of smaller earthquakes make their association with each other and individual faults very difficult. The generally accepted view in seismology is that smaller earthquakes on a fault obey power-law (GR) scaling but a large fraction of the deformation on the fault is associated with large quasi-periodic “characteristic” earthquakes. Thus these large “characteristic” earthquakes satisfy the condition to be dragon kings. In a paper entitled “The Gutenberg-Richter or characteristic

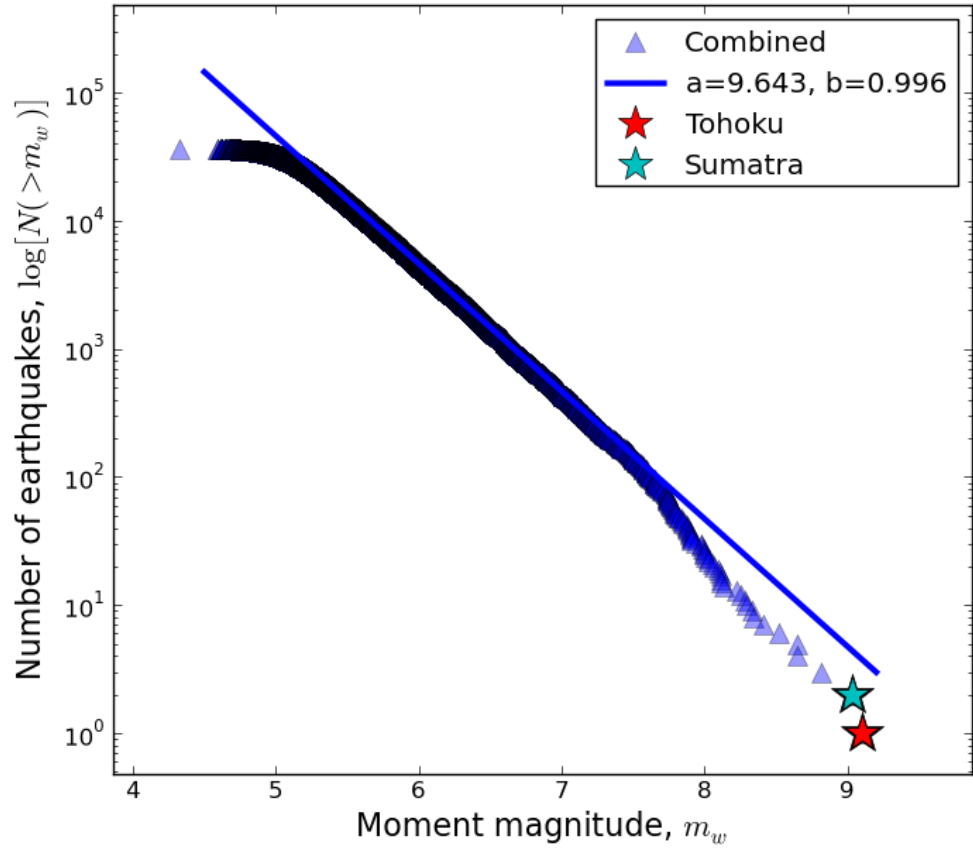


Figure 2.5: Cumulative number of global earthquakes N with magnitude greater than m_w are given as a function of moment magnitudes m_w . Observed values for the period January 1, 1977 to September 30, 2010 are obtained from the global CMT catalog, values for the period October 1, 2010 to August 15, 2011 are obtained from the ANSS catalog. The least-squares best fit of Equation 2.2 to the values in the range $5.5 \leq m_w \leq 7.5$ is given taking $a = 9.643$ and $b = 0.996$. Also included are the 2004 $m_w = 9.0$ Sumatra earthquake and the 2011 $m_w = 9.1$ Tōhoku earthquake.

earthquake distribution, which is it?”, Wesnousky [55] has given data to support the generally accepted view that a working definition of characteristic earthquakes is that they are large earthquakes on plate-boundary faults. As examples we consider two major plate-boundary faults: (1) The San Andreas fault in California is a major boundary fault between the Pacific and North American plates and (2) the subduction zone fault (unnamed) above the Pacific plate as it is being subducted beneath Japan.

A comprehensive study of characteristic earthquakes has been carried out on the southern section of the San Andreas fault. Paleoseismic studies using radiocarbon dating of fluidized sediments at the Wrightwood site [56] date characteristic earthquakes at (in years CE): 534 (407-628), 634 (551-681), 697 (657-722), 722 (695-740), 781 (736-811), 850 (800-881), 1016 (957-1056), 1116 (1047-1181), 1263 (1191-1305), 1487 (1448-1518), 1536 (1508-1569), 1685 (1647-1717), 1812 (historic), 1857 (historic). The ranges of values are the 95% confidence intervals on the radiocarbon dates. The 1857 earthquake was an historic earthquake that ruptured some 400km of the fault from central California to the Los Angeles area. No seismic recordings were available at the time of this earthquake but measurements of surface displacements indicate a magnitude $m \approx 7.9$. In the past 75 years no earthquake with $m > 5.5$ has occurred on this fault segment. If GR scaling were valid for this fault $m > 5.5$ earthquakes would be expected every year. For GR scaling to be valid there should be 100 $m > 6$ earthquakes for each $m = 8$ earthquake. Seismologists generally accept that the sequence of paleo-earthquakes listed above are characteristic earthquakes [55]. Similarly the 1906 earthquake that destroyed San Francisco is generally accepted to be a characteristic earthquake on the northern San Andreas fault. However, paleoseismic sites are not available on the rupture zone of this earthquake.

Similar paleoseismic studies have dated characteristic earthquakes on the southern Nankai Trough segment of the subduction zone beneath Japan. Characteristic earthquakes occurred in 684, 887, 1099, 1361, 1605, 1707, 1854, and 1946. The

dates for these earthquakes were obtained using a variety of historic and other records [57]. The Tōhoku earthquake was a characteristic earthquake on the northern section of this fault and is similar to the San Francisco earthquake in that paleoseismic data are not available [55].

The best documented sequence of characteristic earthquakes occurred on the Parkfield segment of the San Andreas fault in California. Evidence suggests that earthquakes with $m \approx 6$ occurred in 1857, 1881, 1901, 1922, 1934, 1966, and 2004 [58]. Based on seismograms the 1922, 1934, 1966, and 2004 events were remarkably similar in magnitude. The Parkfield earthquakes are globally unique in that they are a sequence of relatively small plate-boundary “characteristic” earthquakes. Thus they occur frequently and a complete “characteristic” earthquake cycle can be studied. In order to study the seismicity associated with the 2004 “characteristic” earthquake we consider earthquakes during the period 1972 (five years after the $m = 6.0$, June, 1966 earthquake) to 2009 (five years after the $m = 5.95$, 28 September, 2004 earthquake). To isolate seismicity associated with the characteristic Parkfield earthquake we confine our study to the region where aftershocks of the 2004 earthquake were concentrated [59].

The region is elliptical, centered at 35.9° N and -120.5° W with semi-major and semi-minor axes of 0.4° and 0.15° respectively, oriented at 137° NW. Both the aftershocks and the elliptical region are shown in Figure 2.6. It is standard practice to associate the aftershock regions with correlated seismicity to study a characteristic earthquake [55, 60, 61]. Another advantage of the Parkfield region is the localization of the correlated seismicity. This region clearly excludes the aftershocks of the $m = 6.5$ (2004) San Simeon earthquake (lower left hand corner in Figure 2.6) and the aftershocks of the $m = 6.5$ (1983) Coalinga earthquake (just above the red elliptical area).

Parkfield is the site of the highest quality local seismic network in the world [58]. This network was constructed by the U.S. Geological Survey in the 1980’s in the expectation that the next characteristic earthquake would occur. In our

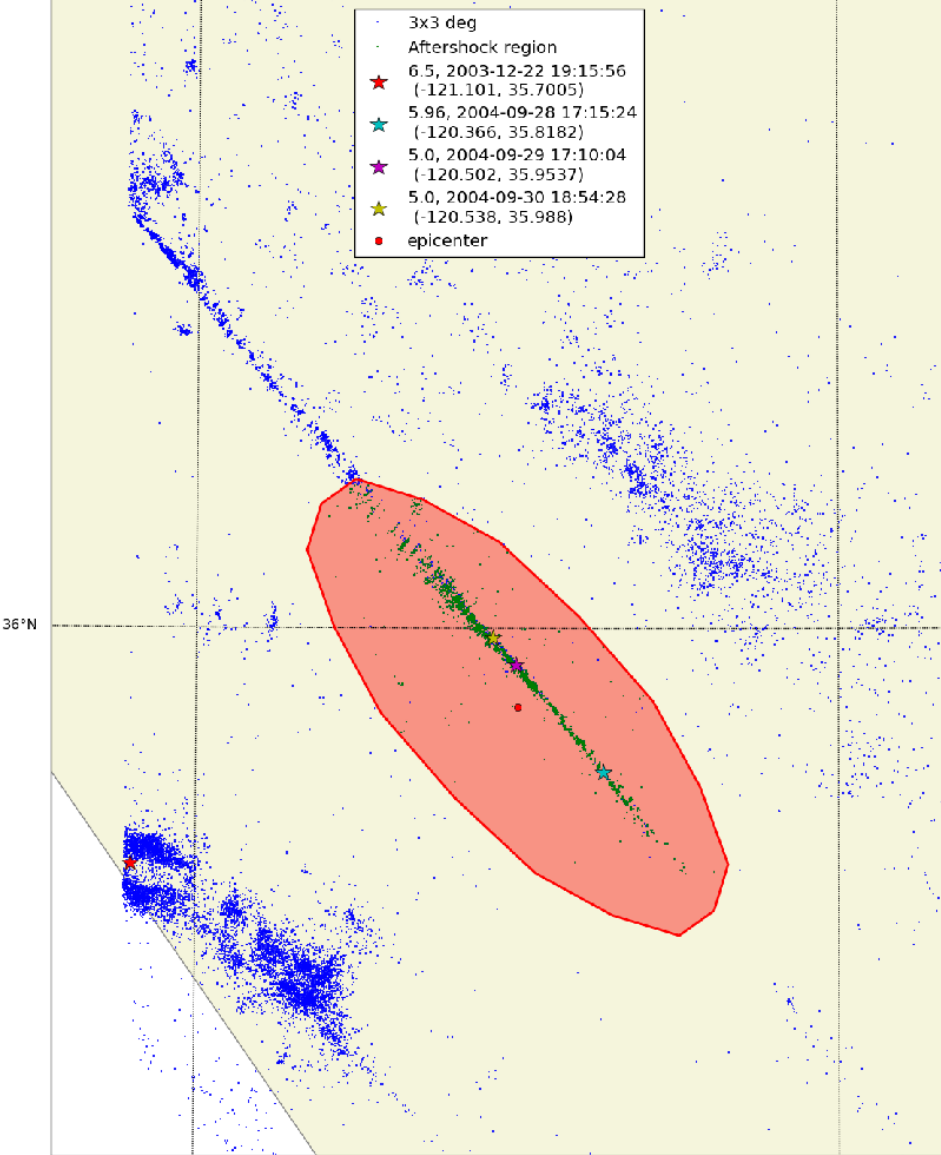


Figure 2.6: Seismicity in central California for the period 28 September, 1999 to 28 September 2009. The aftershocks of the 18 September, 2004 Parkfield earthquake are shown in the red elliptical area. Aftershocks of the 2004 San Simeon earthquake and residual aftershocks of the 1983 Coalinga earthquake are clearly seen to the south-west and north-east of the study region.

analysis we have used the catalog provided by the Northern California Earthquake Data Center (NCSN catalog, quake.geo.berkeley.edu/ncedc/).

The cumulative frequency-magnitude distribution of earthquakes in the Parkfield aftershock region for the period 1972 to 2009 is given in Figure 2.7. The best-fit scaling to this distribution is given by

$$N = 4.47 \times 10^5 10^{-m}. \quad (2.4)$$

This is the least-squares best fit to the data in the range $2.5 < m < 4.5$. Over this range there are some 3,000 data points. The roll over for $m < 2.5$ is attributed to a lack of sensitivity of the network for small magnitudes [59]. The roll over for $m > 4.5$ is attributed to the relatively small number of earthquakes: $N \simeq 10$ [59]. If this scaling was applicable to the characteristic earthquake ($N = 1$) it's magnitude would have been $m = 5.65$. The $m = 5.95$ Parkfield main shock clearly lies above the extrapolation of the power-law correlation of the smaller earthquakes. An important question is whether the difference between $m = 5.65$ and $m = 5.95$ can be attributed to the statistical variability of the characteristic earthquakes. Excellent seismic records are available for the 1934, 1966, and 2004 characteristic earthquakes. The magnitudes are $m = 6.0 \pm 0.1$. In addition the seismic records of the 1934 and 1966 earthquakes are essentially identical indicating near identical points of rupture initiation and propagation pattern. The 2004 earthquake has a somewhat different rupture pattern but the rupture zone is considered to very nearly identical to the earlier earthquakes. The evidence is that these are truly characteristic earthquakes that rupture the same specified segment of the San Andreas fault. The possibility that one of these characteristic earthquakes could have had a magnitude as low as 5.65 is excluded by the available data. Thus we conclude that the sequence of characteristic earthquakes of the Parkfield segment are dragon kings. Although the $\Delta m = 0.3$ difference between the 2004 Parkfield event and what one would expect from extrapolating the scaling relation in Equation 2.4 may not seem large, it represents about a factor of three difference in energies which does set it above the extrapolated GR background.

For reasons stated above the Parkfield characteristic earthquake cycle is the only such cycle that can be studied in detail using a high quality earthquake catalog. However, based on the absence of earthquakes adjacent to other segments of the San Andreas fault and other faults where characteristic earthquakes occur,

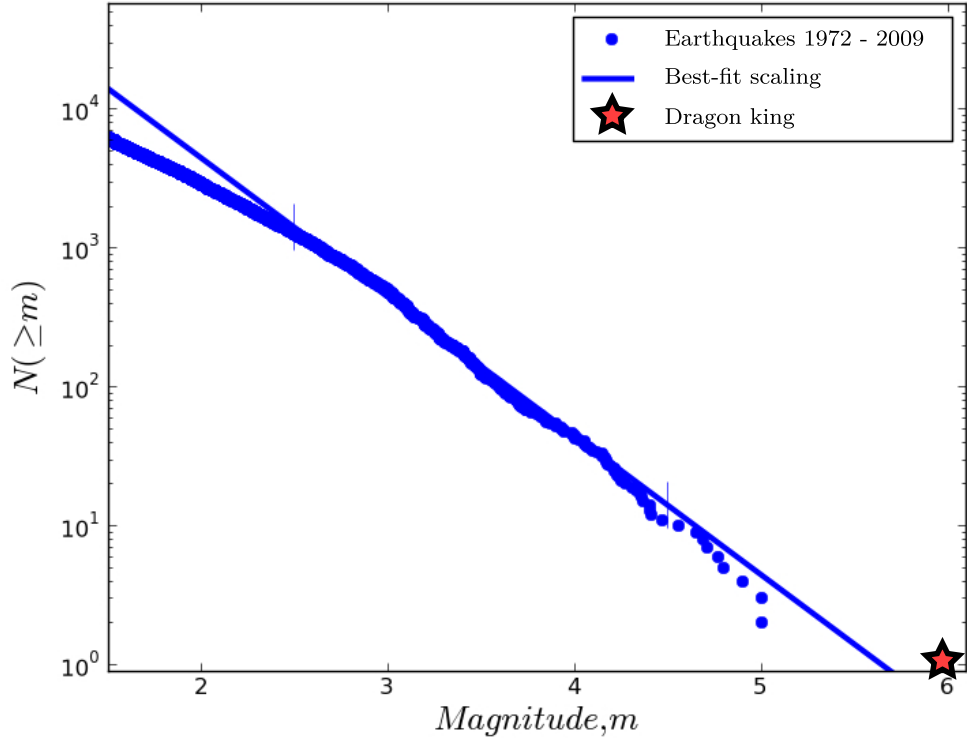


Figure 2.7: Cumulative number of earthquakes with magnitude greater than m as a function of m for the Parkfield earthquake cycle 1972 to 2009. The best-fit scaling from Equation 2.4 is also shown. The $m = 5.95$ Parkfield earthquake is shown as a dragon king.

we conclude that characteristic earthquakes are dragon kings with respect to the correlated seismicity (including aftershocks). The background seismicity satisfies power-law Gutenberg-Richter statistics but the characteristic earthquakes lie above the extrapolation as shown in Figure 2.7.

2.3.3 Volcanic eruptions

Volcanic eruptions are quantified in terms of the dense rock equivalent volume V_{DRE} . This is the volume of magma ejected as tephra (pumice and ash) during an explosive eruption and/or the volume of lava extruded.

In April 1815 an eruption on Mount Tambora in Indonesia resulted in the generation of about $V_{DRE} = 32 \text{ km}^3$ of ash [62]. This ash and associated gases resulted in global cooling, 1816 was known as the year without a summer. In the

northeastern United States snow or frost occurred in every month of the year and a global famine resulted. Certainly this event could be called a black swan.

The frequency-volume distribution of major eruptions is given in Figure 2.8 for the period 1800 to 2002. The cumulative number per year N_C is given as a function of dense rock equivalent volume V_{DRE} [63]. It is seen that this data are well approximated by the power-law (fractal) relation

$$N_c = 0.0586 V_{DRE}^{-0.616}. \quad (2.5)$$

with V_{DRE} in km^3 . The Tambora eruption with $V_{DRE} = 32 \text{ km}^3$ was the largest eruption since 1800 but does not deviate significantly from the power-law scaling. Thus while the eruption was certainly a black swan in terms of global impact it was not a dragon king in terms of being unexpected.

From Figure 2.8 we see that the power law frequency-volume relation for volcanic eruptions is a good approximation in the range $0.04 < V_{DRE} < 10 \text{ km}^3$. An important question is whether this scaling can be extrapolated to longer time frames, i.e. the dashed line in Figure 2.8. Certainly, just as in the case of earthquakes the power-law scaling must roll over for very large events. An eruption cannot be larger than the size of the earth.

Another catastrophic eruption at Lake Toba, Sumatra is estimated to have erupted $V_{DRE} = 2,750 \pm 250 \text{ km}^3$ of dense rock equivalent 73,500 ± 500 years ago [64]. There is evidence that this eruption had a strong impact on human evolution [65] and could certainly be called a black swan. Taking $V_{DRE} = 2,750 \text{ km}^3$ and assuming that this is an eruption that would occur only once in 73,500 years, i.e. $N_c = 73,500^{-1} \text{ yr}^{-1} = 1.36 \times 10^{-5} \text{ yr}^{-1}$ we also show this eruption in Figure 2.8. From Equation 2.5 the largest eruption expected in 73,500 years ($N_c = 1.36 \times 10^{-5} \text{ yr}^{-1}$) would have volume $V_{DRE} = 7.9 \times 10^6 \text{ km}^3$. This is a 200 km cube of rock. Such an eruption is clearly impossible so that power-law scaling must roll over on a time scale considerably less than 75,000 years. We conclude that although the Lake Toba eruption was certainly a black swan, the eruption

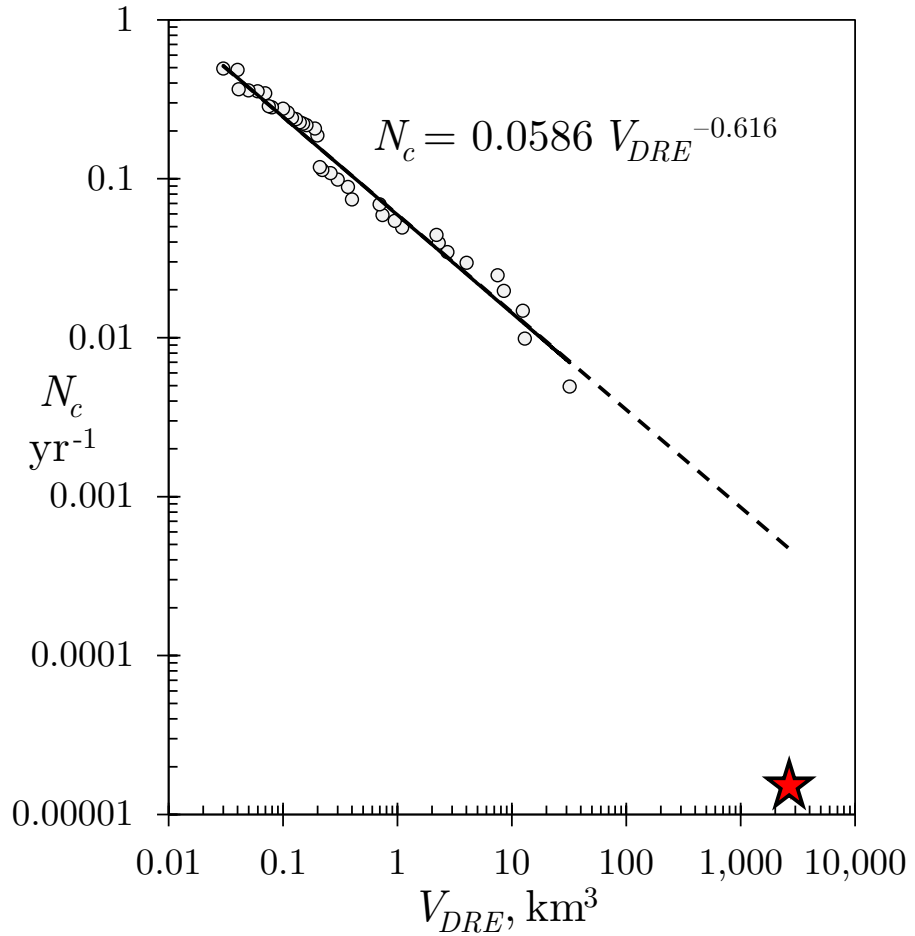


Figure 2.8: Cumulative number of volcanic eruptions N_c during the period 1800-2002 with dense rock equivalent volume greater than V_{DRE} as a function of V_{DRE} . The best-fit power-law scaling from Equation 2.5 is also shown along with the Toba eruption (red star).

was not unexpected in terms of the power-law scaling given in Equation 2.5 and cannot be considered a dragon king. We would suggest an exponential roll over in Figure 2.8 for volumes greater than $V_{DRE} \approx 10^2 \text{ km}^3$. Volcanoes capable of producing dense rock equivalent eruptions with volumes greater than $1,000 \text{ km}^3$ are known as supervolcanoes. In addition to Lake Toba, other supervolcanoes are Taupo, New Zealand and Yellowstone, U.S.A.

An interesting question is whether characteristic eruptions occur on individual volcanoes in analogy to characteristic earthquakes on faults. Also, whether smaller eruptions on a volcano satisfy power-law frequency-magnitude statistics. Unfortunately there are not sufficient data available to answer these questions.

2.3.4 Wildfires

Many studies have been carried out on the frequency-area statistics of wildfires [1, 30, 66]. The general consensus is that they are well approximated by power-law distributions. As an example we give the frequency-area statistics for 7,422 wildfires in California in Figure 2.9. These fires were on United States Forest Service lands during the period 1970 to 2006 [2]. The frequency densities of fires $\Delta N_F / \Delta A_F$ are given as a function of burned areas A_F . Also included is the best fit power-law distribution given by

$$\frac{dN_F}{dA_F} = 498 A_F^{-1.48}. \quad (2.6)$$

with A_F in km^2 . An excellent power-law scaling is seen. There is no evidence for anomalously large fires, i.e. dragon kings, in the data set and in the many other power-law correlations that have been published (i.e. [1, 30, 65]).

Fire suppression appears to increase the occurrence of large fires. Minnich [67, 68] studied this effect by comparing the frequency-area distribution of wildfires in southern California, where anthropogenic fire suppression was extensive, with distributions in Baja California, where suppression is uncommon. Both distributions were in reasonably good agreement with power laws but with a larger slope (fewer large fires) in Baja California. This analysis is consistent with studies of

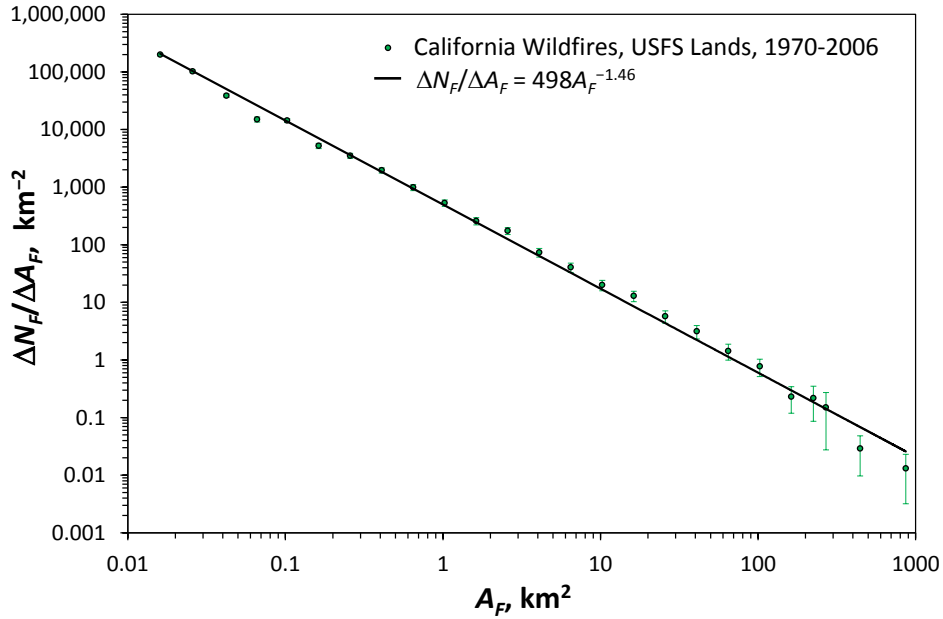


Figure 2.9: Frequency-area statistics for 7,422 wildfires on United States Forest Service lands in California for the period 1970-2006 [2]. The frequency densities $\Delta N_F / \Delta A_F$ are given as a function of burned area A_F . Also shown is the best least-square power-law fit to the data.

fire return intervals (FRI) and fire intensities in the Klamath National Forest area [69–71], particularly in conjunction with numerical modeling [72]. Collectively, these studies indicate that fire suppression changes the exponent in the power-law correlations but does not lead to large dragon-king fires.

2.3.5 Landslides

Relatively few inventories of landslide frequency-area distributions are available. One reason is that landslide scars are subject to relatively rapid erosion. A number of triggered landslide events have been analyzed while still fresh. Three examples [3] are given in Figure 2.10. These are:

1. 11,111 landslides triggered by the 17 January 1994 Northridge, California earthquake.

2. 4,237 landslides triggered by a snowmelt event in the Umbria region of central Italy in January 1997.
3. 9,594 landslides triggered by heavy rains from Hurricane Mitch in Guatemala in late October and early November 1998.

The probability densities p of the distributions are given as a function of landslide area A_L in Figure 2.10. Also shown in Figure 2.10 is the least-squares best-fit gamma distribution. For large landslides ($A_L > 200 \text{ m}^2$) this best-fit distribution reduces to the power-law correlation

$$p(A_L) = 10^{-4} A_L^{-2.4}. \quad (2.7)$$

with A_L in km^2 .

The frequency-area distributions for the larger landslides generally satisfy power-law correlations to a good approximation [3]. There is no evidence for anomalously large dragon-king landslides in these distributions. Certainly many large landslides have been documented and some of these could be dragon kings. However, relevant inventories are not available so a statistical study such as illustrated in Figure 2.10 cannot be carried out. It is also relevant to note that rock falls must be considered separately as their statistics are different than landslides [3].

2.3.6 Floods

Floods are a major hazard to many cities and estimates of flood risk have serious economic consequence. Floods are quantified in terms of the volumetric discharge at a point on a river. The discharge $Q(T)$ is the maximum discharge associated with a recurrence interval of T years, that is $Q(100)$ is the maximum flow expected once every 100 years, i.e. the 100 year flood. Flood-frequency estimates are empirical and a wide variety of statistical distributions have been used [73]. Record floods can cause large loss of life, property damage, and crop damage. Thus record floods can be classified as black swans. Record floods appear to occur more often than predicted by flood frequency estimates. Thus they may be dragon kings.

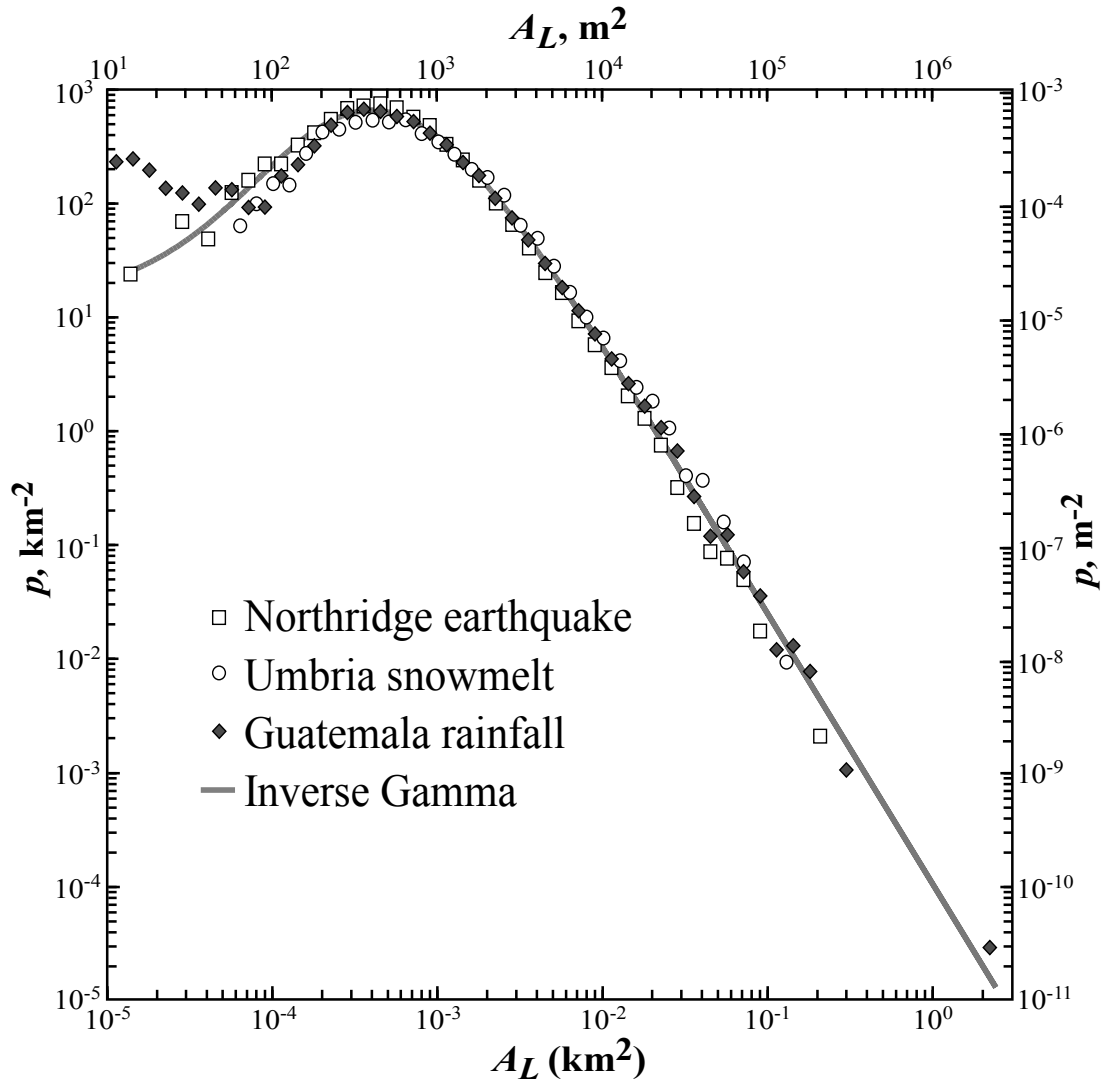


Figure 2.10: Frequency-area statistics for three landslide inventories [3]: (1) 11,111 landslides triggered by the Northridge earthquake, (2) 4,237 landslides triggered by a snowmelt event Italy, (3) 9594 landslides triggered by Hurricane Mitch. The probability density p is given as a function of landslide area A_L . Also shown is the least-squares best-fit gamma distribution.

In our discussion we will focus our attention on floods that have occurred on the Colorado River [74], in particular on paleo-floods that occurred up to 1,400 years ago. We first consider discharge obtained at the Lees Ferry gauge during the period 1921-1962 (more recent observations were influenced by the construction of the Glen Canyon Dam). Federally mandated flood frequency forecasts in the United States utilize the sequence of maximum annual floods at a gauging station. This flood is the peak discharge $Q(1)$ during a water year: October 1 of the previous year to September 30 of the year in question. The yearly floods are ranked from largest to smallest. For the 42 year record at the Lees Ferry gauge the largest flood is given a period $T = 42$ years, the second largest flood a period of $T = 21$ years, and so forth to the smallest annual flood with a period of $T = 1$ year. These values are given in Figure 2.11.

The federally mandated forecasts utilize the log Pearson type 3 (LP3) distribution to fit the annual values. This distribution is then extrapolated to forecast future floods. This mandated forecast is also illustrated in Figure 2.11.

A major problem with the annual flood series is that several statistically independent floods in a water year may be larger than the annual flood in another water year. To overcome this difficulty the partial duration flood series was introduced [74]. In this flood series a peak flow must be separated by at least 30 days to be defined as an independent flood. For the 42 year Colorado River sequence the largest 42 independent peak flow are taken to be the partial duration flood series. The partial duration flood series for the Lees Ferry gauge data is also shown in Figure 2.11. The two flood series strongly diverge for periods less than five years and for future extrapolations.

The LP3 distribution is a relatively thin-tailed distribution. The applicability of the fat-tailed power-law distribution to floods has been suggested [4]. In this case we have

$$Q(T) = CT^\alpha. \quad (2.8)$$

Instead of using the annual floods for analysis, the partial-duration flood series is used. The best fit of Equation 2.8 to the Lees Ferry data requires $C = 3.28$ and $\alpha = 0.28$, this fit is illustrated in Figure 2.11.

Two paleo-flood discharge estimates on this section of the Colorado River were obtained by O'Connor et al. [5]. The levels of flood debris were used to estimate discharge and radiocarbon dates on the debris were obtained. The results are shown as points A and B in Figure 2.11. Point A is interpreted as the historic Colorado River flood of 1884. The discharge is estimated to be $Q = 8,800 \text{ m}^3\text{s}^{-1}$ and it is assigned a recurrence interval of $T = 112$ years. Point B is estimated to have had a discharge $Q = 14,000 \text{ m}^3\text{s}^{-1}$ with an age 1200-1600 years BP, it is assigned a recurrence interval $T = 1400$ years. While the paleo-floods exceed the LP3 fit by a considerable amount, they are quite close to the power-law fit. Since the definition of a dragon king implies the extrapolation of power law scaling, we conclude that the two paleo-floods were not dragon kings. While we have only given one example, other studies [4] indicate extreme floods are well estimated by the power-law scaling as defined in Equation 2.8.

2.4 Discussion

The clearest example of dragon king behavior given in this paper is the stiff slider-block model illustrated in Figure 2.2. The small slip events satisfy power-law (fractal) statistics, but an anomalously large number of system-wide events occur. There are two scaling parameters in the slider-block model, the stiffness of the system $\alpha = k_C/k_L$ and the size of the system L . With fixed L , the range of power-law behavior increases with increasing stiffness. When this range extends to the system size L , system wide events occur. The larger the system size L , the larger the stiffness parameter α required to get system wide events. Very stiff systems exhibit well defined dragon-king behavior. We have also shown that the forest-fire model exhibits dragon-king behavior as illustrated in Figure 2.3. The extrapolation is identical to that of the slider-block model with the firing frequency

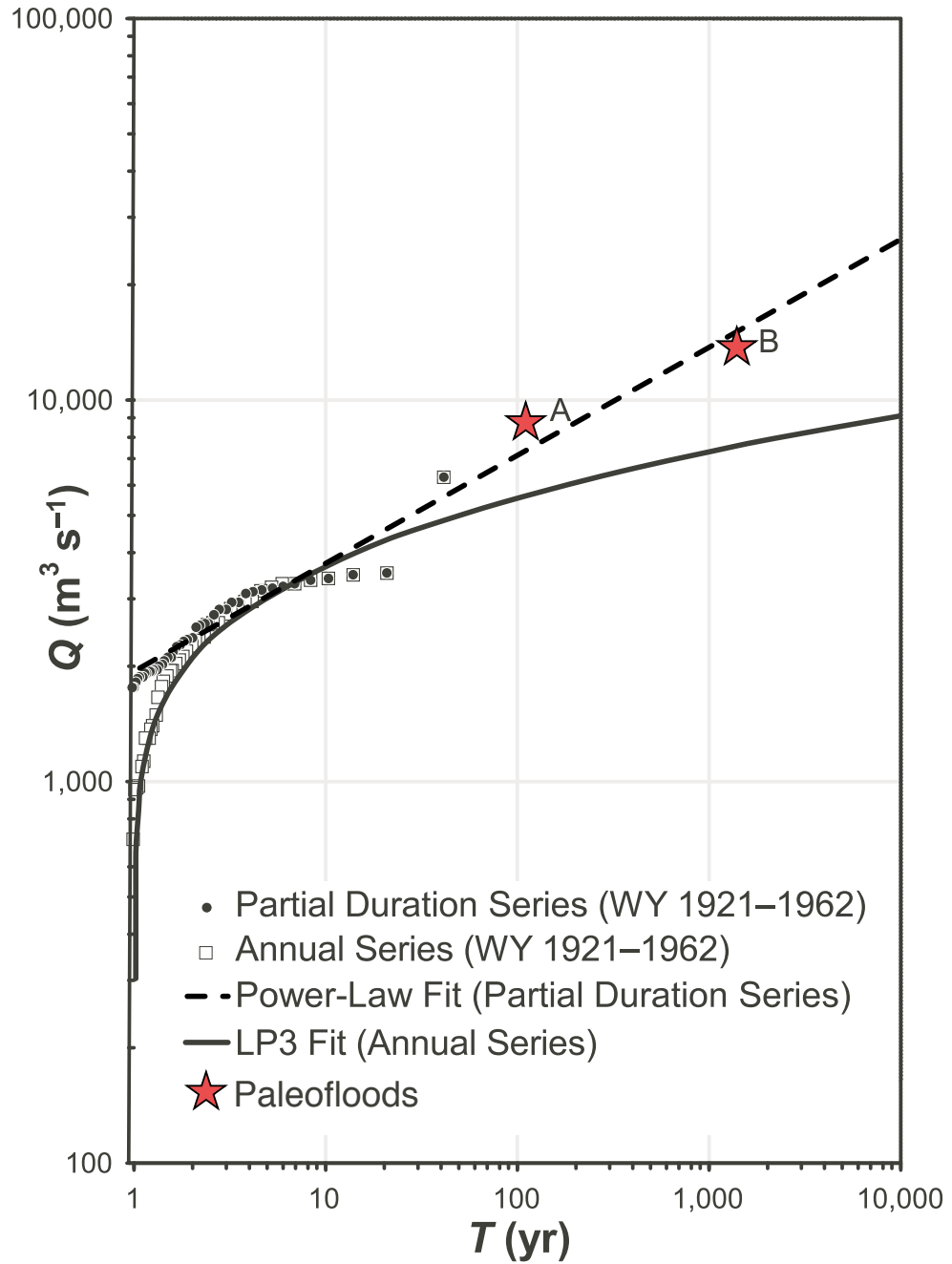


Figure 2.11: Dependence of the maximum daily discharge Q associated with time period T for the Colorado River in the Grand Canyon, Arizona [4]. The annual and partial duration flood series at the Lees Ferry gauging station for the water years 1921–1962 are shown. The least-squares power-law fit to the partial duration series and the LP3 fit to the annual series are also given. Points A and B are estimates of two paleofloods [5].

f_s playing the role of the stiffness. However, as shown in Figure 2.4, the sandpile model does not have anomalously-large system-wide events. This is because there is no tuning parameter in this model.

In terms of the natural phenomena considered in this paper, characteristic earthquakes on faults can be associated with dragon-king behavior. We have illustrated this with the characteristic earthquake on the Parkfield segment of the San Andreas fault. The smaller earthquakes on and adjacent to the fault satisfy power-law statistics but the magnitude of the characteristic earthquake lies above the extrapolation of the power-law behavior as illustrated in Figure 2.7. This behavior is generally accepted by seismologists [55]. This led to the concept of characteristic earthquakes: the large set of quasi-periodic earthquakes that occur on recognized faults.

We have shown that global frequency-size distributions of earthquakes and volcanic eruptions exhibit power-law behavior for smaller sizes but have roll over for large events similar to the behavior of the forest-fire model for small firing frequencies. The data for wildfires, landslides, and floods are more limited and neither roll over nor dragon king behavior has been observed.

The applicability of power-law statistics to natural hazards has important practical implications. For example, probabilistic seismic hazard studies extrapolate the rate of occurrence of small earthquakes to quantify the probability of occurrence of large earthquakes. This extrapolation would not be valid if dragon king earthquakes occur.

Chapter 3

Virtual California

Over the past three decades computer simulation has played an increasingly important role in studying complex natural phenomena. Examples range from climate modeling to star and galaxy formation in the early universe. However, despite the importance of computer simulation in many fields, seismology has been somewhat slow to adopt the practice. The reasons for this are many, but the difficulty of creating large simulations of interacting faults and the uncertainty of the exact physics involved in earthquakes are both major factors. Both of these issues are beginning to be addressed in a new generation of seismic simulators. These simulators borrow techniques from statistical physics to simplify the complicated geomechanics of rupturing fault systems. They are also designed to take advantage of recent advances in computer hardware and software.

This chapter describes a next generation seismic simulator called Virtual California, which is part of a larger effort to develop simulation-based forecasting of seismicity in California [75–77].

3.1 Introduction

Earthquakes typically occur on preexisting faults. Displacements on these faults are governed by “stick-slip” behavior and “elastic rebound.” Because of the relative motion of the tectonic plates, stress on a fault increases. The fault “sticks” until the stress reaches the frictional strength of the fault, the fault then “slips” and

“elastic rebound” occurs. Fault systems, however, are difficult to study. They are affected by dynamics at many different scales both in time and space, and they are physically inaccessible making direct measurements of their properties problematic.

Earthquake fault systems are chaotic and highly unpredictable, similar to the behavior of the atmosphere, for which weather forecasts and global climate models rely heavily on simulations. Because of this similarity, computer simulations are an invaluable tool in better understanding how fault systems operate. Virtual California is a computer simulation which models the earthquake fault system in California [27, 78] – although the core of the simulation code can be used for any fault system. We will describe the various elements of the Virtual California code and discuss results from a simulation. We also discuss details of implementing the code and optimizations to improve simulation performance.

The model that would eventually become Virtual California started as a limited simulation model for the distributed seismicity on the San Andreas and adjacent faults in southern California developed by Rundle [79, 80]. This model included stress accumulation and release as well as stress interactions between faults. An updated version of this model was developed [81–83] including the major strike-slip faults in California and was called Virtual California. Details of the model were given in [78, 84]. Yakovlev et al. [25] utilized Virtual California simulations to examine the recurrence time statistics on faults in California. They concluded that the distribution of return times on a fault is well approximated by a Weibull distribution. Yikilmaz et al. (2010) [26] used Virtual California to simulate earthquakes on the Nankai Trough, Japan and found an excellent agreement with the historical sequence of 13 great earthquakes. Yikilmaz et al. (2011) [27] gave a composite simulation of seismicity in Northern California utilizing Virtual California for earthquakes on mapped faults, a random background of smaller earthquakes, and a BASS simulation of aftershocks. In its current incarnation, Virtual California is a sophisticated tool for simulating earthquakes on a wide variety of fault

geometries in a high performance computing environment, and is part of a larger effort by the Southern California Earthquake Center to unify the results from several different earthquake simulators. A description of this effort and a comparison of the results from different simulators can be found in [76] and [77] respectively.

3.2 Ensemble-Domain Verses Time-Domain Simulations

Earthquake fault simulations generally fall into one of two categories: ensemble-domain and time-domain. Before we describe Virtual California in detail it is important to draw a distinction between these two types of simulations. A time-domain fault simulation attempts to solve a set of differential equations that govern the evolution of the system. These simulations usually employ an approximation scheme like finite-element analysis. The result of these solutions is a function which has time as an independent variable, so in principle the state of the system at any given time is encoded in the solution. Aside from the considerable computational difficulty of applying the time-domain approach to fault systems, problems arise from the sensitivity of these solutions to initial conditions. As mentioned above, collecting information about the current state of a fault is difficult which makes precise definitions of initial conditions difficult.

An ensemble-domain simulation sidesteps the problem of initial conditions by looking for the most likely states of the system given some set of external parameters. Instead of generating a single “history” of the system, many histories are created – a so-called ensemble. This ensemble is then the basis of a statistical analysis. Because the ensemble is a combination of many different paths the system can take, it is less sensitive to where those paths begin. A familiar example of this approach is the Metropolis Monte Carlo algorithm [24]. Virtual California as well as several other simulators [85–87] are examples of an ensemble-domain simulation.

3.3 Components of Virtual California

The underlying structure of Virtual California is based on the cellular automaton (CA) slider block model of Rundle and Jackson [88]. In this model, an array of blocks are pulled across a surface by a loader plate that moves at a constant velocity. The blocks are connected to the loader plate by one set of springs and to each other by another set of springs (Figure 2.1). These systems have been studied extensively and have been shown, under certain circumstances, to reproduce some of the observed scaling properties of fault systems [41, 89].

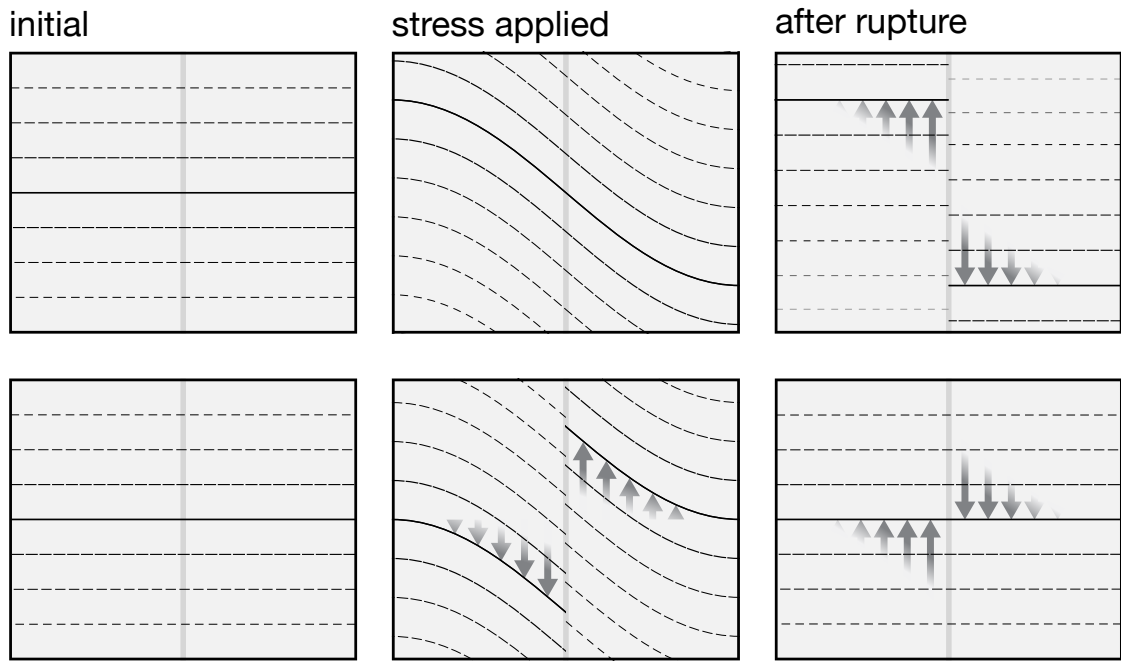


Figure 3.1: An illustration of the differences between an actual fault and a back-slip fault. Each image is a view from above of a surface surrounding a fault (which is represented by the gray vertical line in each image). The horizontal lines show the deformation of the surface as forces are applied. **Top** The earthquake cycle on an actual fault. **Bottom** The earthquake cycle on a back-slip fault.

In order to apply the slider block model to an earthquake fault system, a technique called “back-slip” must be employed. In an actual fault system, long-range plate motions cause stresses to build up along faults. When the stresses exceed a failure threshold, the faults break and the ground displaces on either side of the fault. This situation is illustrated in the top of Figure 3.1. Difficulties

arise in modeling this behavior because of the change in geometry after a fault ruptures. The dynamics of crack propagation are complicated and because of the relative scales involved are a minor effect. For example, in the fault model of California described in Section 3.3.1, the average slip over 10,000 years results in only \sim 55 meters of displacement, \sim .1% the size of an individual 3km \times 3km fault element. Therefore, for the sake of computational simplicity, it is desirable to develop a model where fault geometries remain fixed during ruptures. Back-slip models avoid the problems associated with changing fault geometries by treating faults like leaf springs. Stress buildup along the fault is modeled as the stretching of these springs in the opposite direction of the plate motions that cause stress in an actual fault. Once the springs reach a failure threshold they are allowed to snap back to their equilibrium position (see the bottom of Figure 3.1).

By using the back-slip approach, Virtual California can be implemented in three components: a fault model, an interaction model, and an event model.

3.3.1 Fault Model

As mentioned above, the fault model is the only component of Virtual California that is specific to California. The model that is currently in use is based on the Uniform California Earthquake Rupture Forecast version 2 (UCERF2) [6] fault model developed by the Working Group on California Earthquake Probabilities (WGCEP). The model – called ALLCAL2 – includes 181 fault sections roughly corresponding to known faults in California, with some faults modeled by multiple sections. Each fault section is meshed into square elements that are roughly 3km \times 3km, for a total of 14474 elements. In the present version of our model the creeping section of the San Andreas fault is removed (Figure 3.2 top). This section produces many events, slowing the simulation down considerably. Each element in the model is given a constant back-slip velocity along a fixed rake vector and a failure stress. The rake vector always lies in the plane of the element, and the angle of the vector relative to the top edge of the element, along with the rate of slip, are quantities that are taken from the UCERF2 model. The failure stresses, which are

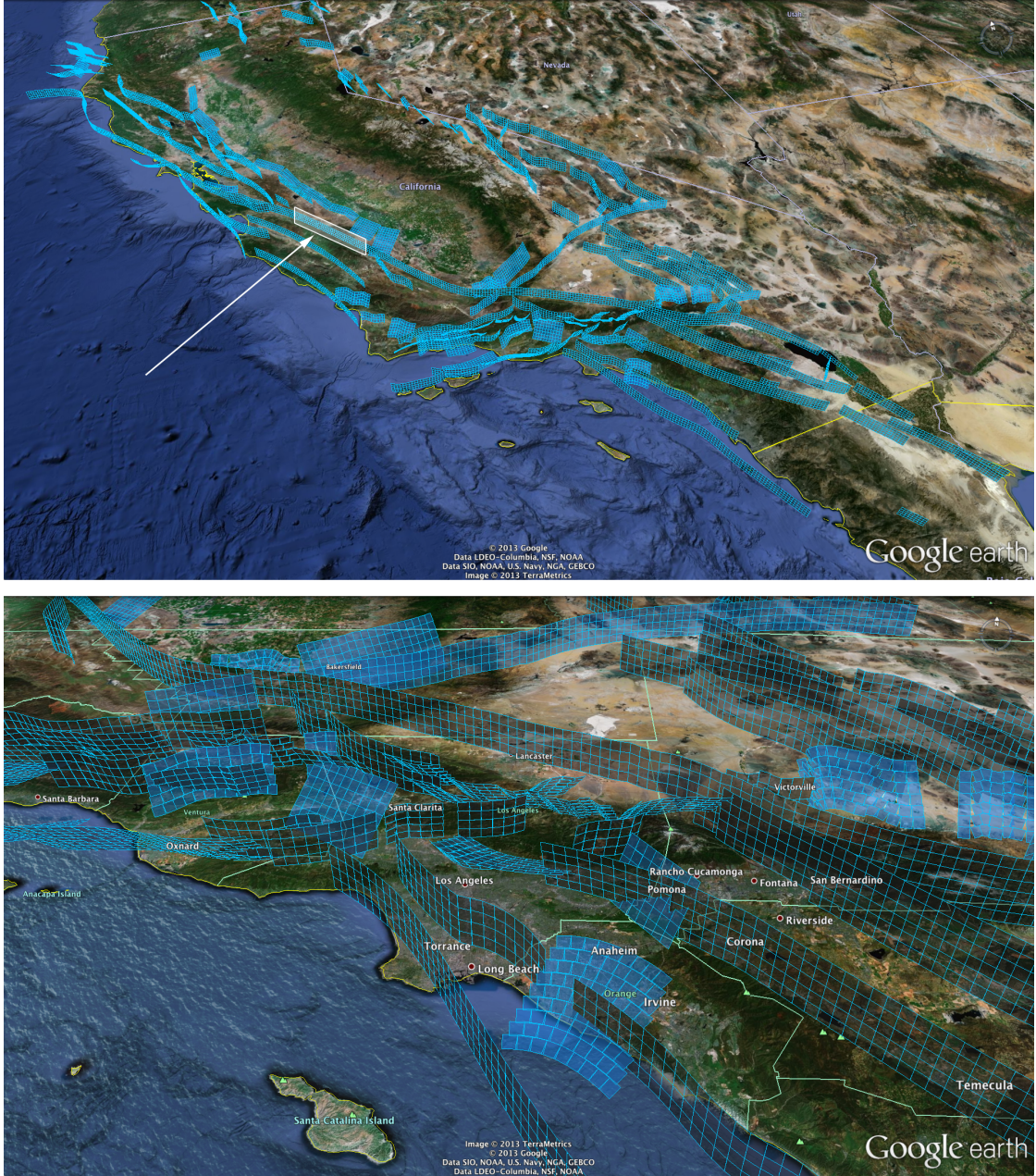


Figure 3.2: **Top** The ALLCAL2 model used in Virtual California. This particular model is based on the UCERF2 [6] fault model. The section indicated in the image is the creeping section of the San Andreas fault. This section tends to generate a large number of events and was removed from the model in order to speed up the simulation. **Bottom** A detail view of the Los Angeles area. In both images the meshed fault sections are rendered directly above their actual locations beneath the surface.

also required for the model, are derived from paleoseismic event recurrence times where available or are set using area-magnitude statistics like the ones described

in [8] and a typical earthquake size for each section.

3.3.2 Element Stress Interactions

Unlike actual fault systems where the fault geometry is dynamic, the fault geometry used by Virtual California is static. This static geometry allows Virtual California to avoid the considerable complexities involved in modeling evolving fault systems. In this sense Virtual California is designed to explore seismicity in fault systems as they exist now. Because the faults don't actually move, back-slip is used to model the effects of stress buildup and release along the fault plane. In a back-slip model the equilibrium position for a failed element is the same as its initial position, so failed elements do not actually change their position.

The static, back-slip approach greatly simplifies how interactions between fault elements are calculated. In general, how back-slip on one element effects stress on another element depends on the position and orientation of both elements. Because the fault geometry is static, these interactions, or stress Green's functions, only need to be calculated once. In order to calculate the stress Green's functions, every element is back-slipped by a unit distance along its slip velocity vector and the changes of stress are calculated for every other element. The stress changes at any location \mathbf{x} in the simulation due to changes on all other elements is given by [78, 84]:

$$\sigma_{ij}(\mathbf{x}, t) = \int dx'_k T_{ij}^{kl}(\mathbf{x} - \mathbf{x}') s_l(\mathbf{x}', t), \quad (3.1)$$

where $s_l(\mathbf{x}', t)$ is the three-dimensional “slip density” at \mathbf{x}' in the l direction and $T_{ij}^{kl}(\mathbf{x} - \mathbf{x}')$ is the Green's function tensor. The Einstein summation convention is assumed. The indices i , j , k and l run over the cartesian coordinate axes, x , y , and z . In the case of Virtual California, the field is only evaluated at the centers of elements and slip is uniform across the surface of an element and is allowed only along the element's rake angle, which is defined by the model. Under these conditions Equation 3.1 simplifies to:

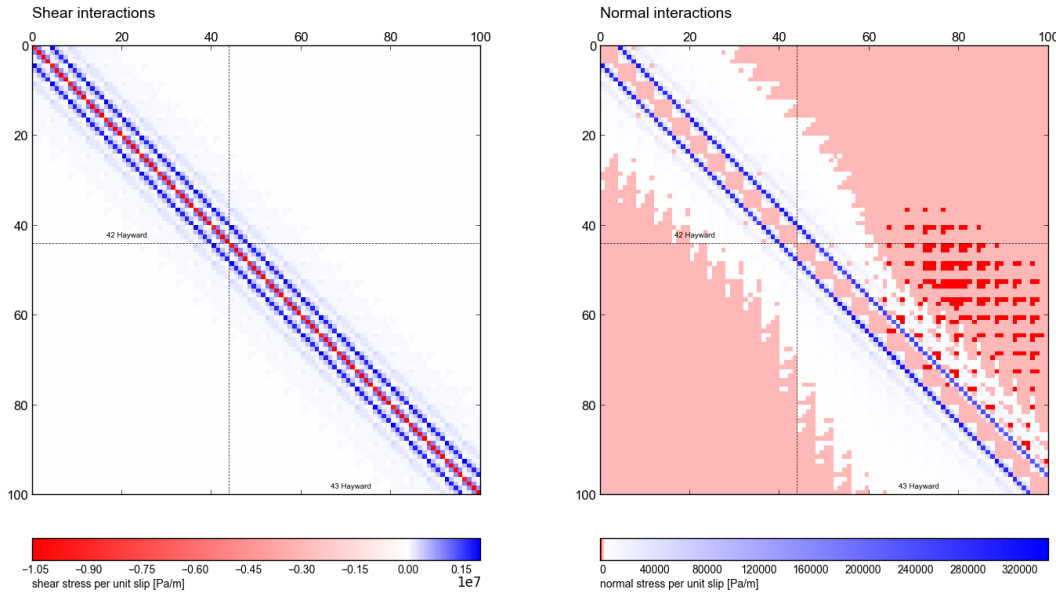


Figure 3.3: The shear and normal greens matrices for the two sections of the Hayward fault from the ALLCAL2 model described in Section 3.3.1.

$$\sigma_{ij}^A(t) = T_{ij}^{AB} s_B(t), \quad (3.2)$$

where A and B run over all elements. Lastly, because we are only interested in the shear stress along the rake vector and the normal stress perpendicular to the plane of the element, the 9 elements of the tensor T_{ij} reduce to T_s for the shear stresses, and T_n for the normal stresses. The final stresses are determined by:

$$\begin{aligned} \sigma_s^A(t) &= T_s^{AB} s_B(t) \\ \sigma_n^A(t) &= T_n^{AB} s_B(t) \end{aligned} \quad . \quad (3.3)$$

So, if there are N elements in a model, Virtual California needs two $N \times N$ matrices to govern all interactions. An example of these matrices is shown in Figure 3.3.

The actual values of the Green's functions are calculated using an implementation of Okada's half-space deformations [90]. An example of the stress field produced by this implementation are shown in Figure 3.4.

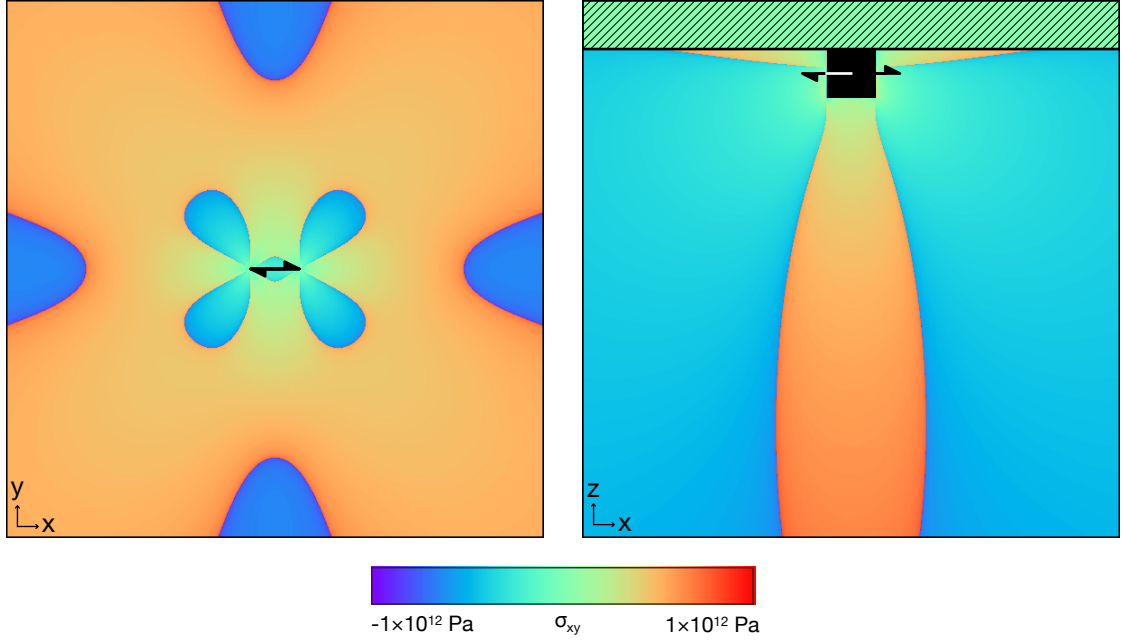


Figure 3.4: The σ_{xy} component of the stress tensor generated by a $1\text{km} \times 1\text{km}$ element slipping 10m in the direction indicated by the arrows (right-lateral). **Left** View of the stress field from above. **Right** View of the stress field from the side.

3.3.3 Event Model

Virtual California uses a static-dynamic friction law to determine when an element fails. This law is implemented by a Coulomb failure function (CFF):

$$CFF^A(t) = \sigma_s^A(t) - \mu_s^A \sigma_n^A(t), \quad (3.4)$$

where μ_s^A is the static coefficient of friction calculated from the model element strengths. When $CFF^A(t_f) = 0$ the element A fails. To simplify the notation we will remove the element label A from the CFF function and just assume that it refers to a single element.

Elements in Virtual California gain and release stress through an event model that consists of two phases. A long term slip phase and a rupture propagation phase. The long-term slip phase models the time between earthquakes when stress builds up on the faults due to tectonic plate movement. This involves applying back-slip to all elements at their model defined back-slip velocities. The long term slip phase ends at time $t = t_f$, when one or more elements CFF becomes 0:

$CFF(t_f) = 0$. Because the interactions in Section 3.3.2 are elastic, the relationship between slip and stress is known (Equation 3.3), and it is not necessary to evolve the system step-by-step during this phase. Rather, the simulation time is directly advanced to the point at which the next element fails and then the rupture propagation phase begins.

During the rupture propagation phase the system releases accumulated stress through a cascading series of fault element failures. Virtual California uses a “cellular automata” approach to modeling rupture propagation. Because of this, ruptures are not a dynamic process in the sense that there are no time domain solutions to differential equations governing them. Instead, given an initial failure and stress state, the system iteratively slips elements to find the final stress state. Equations 3.5 and 3.6 described below are meant to approximate dynamical considerations and generate better output statistics.

When a rupture begins the first element to fail is allowed to slip back toward its equilibrium position. The amount the element slips, Δs , is related to stress-drop defined for the element in the model, $\Delta\sigma$, by [78, 84]:

$$\Delta s = \begin{cases} \frac{1}{K_L} \frac{N_{ef}}{S_t} (\Delta\sigma - CFF), & \text{if } N_{ef} \leq S_t \\ \frac{1}{K_L} (\Delta\sigma - CFF), & \text{otherwise.} \end{cases} \quad (3.5)$$

K_L is the element’s stiffness or self-stress defined (for element A) as: $K_L = T_s^{AA} - \mu_s^A T_n^{AA}$, where T_n and T_s are the normal and shear Green’s matrices described in Equation 3.3. The factor $\frac{N_{ef}}{S_t}$ is related to the current size of the rupture: N_{ef} is the number of failed elements on a particular fault and S_t is the slip-scaling threshold. The slip-scaling threshold is set as an external parameter. This factor is used to prevent small ruptures from slipping too much.

After the initial element slips, a new stress state is calculated for the entire system using Equation 3.3. Additional elements will fail if their $CFF = 0$. In order to encourage rupture propagation a dynamic triggering mechanism is used. Elements on the same fault and physically close to a failed element are allowed

to fail at a lower stress than the defined failure stress, provided that the amount of stress accumulated during the rupture is greater than a pre-defined dynamic triggering factor η :

$$\frac{CFF_{init} - CFF_{final}}{CFF_{init}} > \eta. \quad (3.6)$$

The dynamic triggering factor approximates the stress intensity factor at the tip of a propagating rupture [91, 92].

If failed elements have not slipped back to their equilibrium points due to their initial failures, they are allowed to fail again and release more stress into the system. They are not, however, allowed to slip away from their equilibrium point. This means that they will not absorb any stress released from newly failed elements. This behavior reflects the fact that during a rupture, failed elements are not allowed to heal, but also may not release their accumulated stress all at once. This process continues until there are no more failures, at which point the event is over. It is important to note that elements may not release all of their accumulated stress during a rupture. This is partially due to the slip-scaling threshold (Equation 3.5) and dynamic triggering (Equation 3.6), but also partially due to the overall stress state of the system when the rupture begins. If the system is in a high stress state then very small initial changes in stress can cause a cascading series of failures that result in the release of large amounts of stress (this effect can be seen in Figure 3.5 top). However, if the system is in a low stress state these small initial stress changes will not trigger additional failures.

Figure 3.5 top shows an example of how stress is released and accumulated over multiple event cycles. Figure 3.5 bottom shows how a single element failure can lead to a cascading series of failures in a single event. Figure 3.5 bottom also shows that elements can fail multiple times during an event but will not accumulate additional stress after they fail.

In order to illustrate the effect of the dynamic triggering η , and the slip threshold S_t on the output of Virtual California, we explored the parameter space by

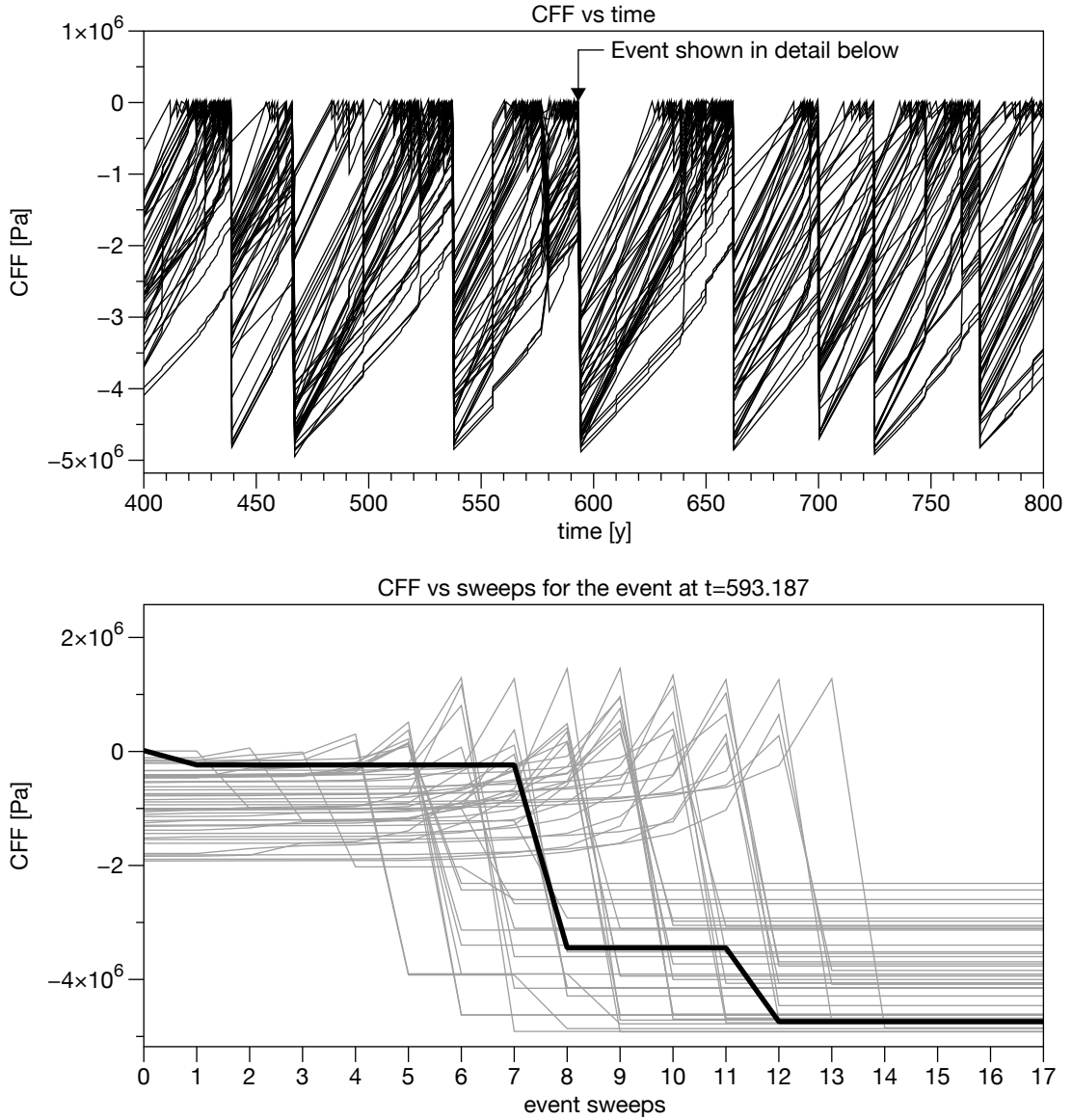


Figure 3.5: **Top** The CFF for each of the 48 elements that make up the Parkfield section of the San Andreas fault. Drops in the CFF correspond to events. Large events are characterized by many elements undergoing large CFF drops. **Bottom** The sweeps that make up the event at $t = 593.187$. The element that triggers the event is in bold. The initial failure triggers a cascade that results in all elements failing.

varying $\eta \in [0.3, 0.9]$ in increments of 0.1, and $S_t \in [0, 40]$ in increments of 10. The result was 36 simulations, each run for 50,000 years using the model described in Section 3.3.1. Results from these simulations are shown in Figures 3.6 and 3.7. As can be seen in the Figure 3.6, η has the effect of encouraging larger ruptures at the expense of smaller ones (top left frame in Figure 3.6), but has a relatively

small effect on the amount of slip in events. The effect of S_t is more complex (Figure 3.7). Without S_t there is a hard lower limit to the magnitude of events that Virtual California can produce. This is because both the size of the elements and the amount by which they slip during an event are fixed by the model. Once S_t is enabled however, the amount of slip during an event varies. This allows smaller events to be produced. Also, because smaller events will release less stress, larger values of S_t produce more large events when the extra accumulated stress is released. Lastly, by reducing the amount of slip for small ruptures, S_t prevents over slipping (top right frame in Figure 3.7).

3.4 Simulation Computational Overview

Next we outline the computational flow of Virtual California. Figure 3.8 shows the path of execution in a parallel simulation running on multiple processors either on a cluster or multicore machine. The execution is divided into three distinct phases - initialization, long term stress interaction and rupture propagation. A straight forward implementation of this simulation would be heavily bound by computation and communication, thus Virtual California uses techniques described in [93] to make this more tractable.

The initialization phase begins by parsing the specified model and simulation parameters. If the simulation is running on multiple processors it partitions the fault elements. This partitioning tries to ensure that each processor is responsible for roughly an equal number of elements and that elements on the same processor are on the same fault or geographically close to each other. Next, each processor calculates stress influences by all model elements upon the local elements as described in Section 3.3.2.

The core of the simulation involves cycling between two phases – the first determines long term stress buildup in the system and the second propagates a rupture through the system – indicated by blue and purple in Figure 3.8. The simulation begins in the long term stage by calculating the rate of long-term stress

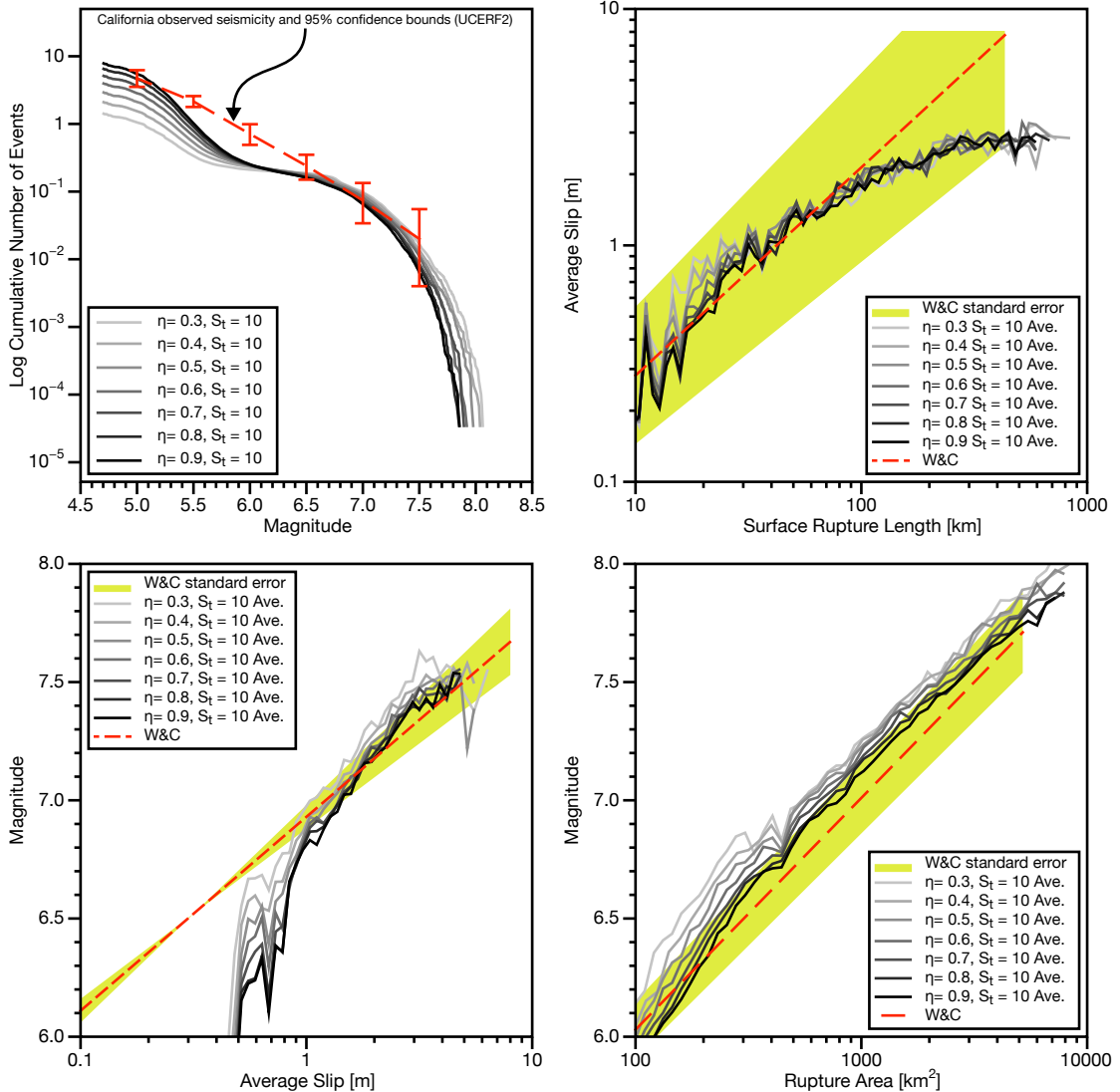


Figure 3.6: Examples of how varying dynamic-triggering η (Equation 3.6) effects Virtual California output. The observed values in the top-left frame are taken from UCERF2 [6]. The observed values in the remaining frames are taken from Wells and Coppersmith (W&C) [7].

buildup for each element. In a parallel simulation each processor determines when each of the local elements will rupture, which is then globally reduced to find when and where the first rupture will occur.

Once this is determined, the rupture is propagated through the system using the mechanisms described in Section 3.3.3. First, the ruptured elements are processed and their new stresses are communicated through the system. Each

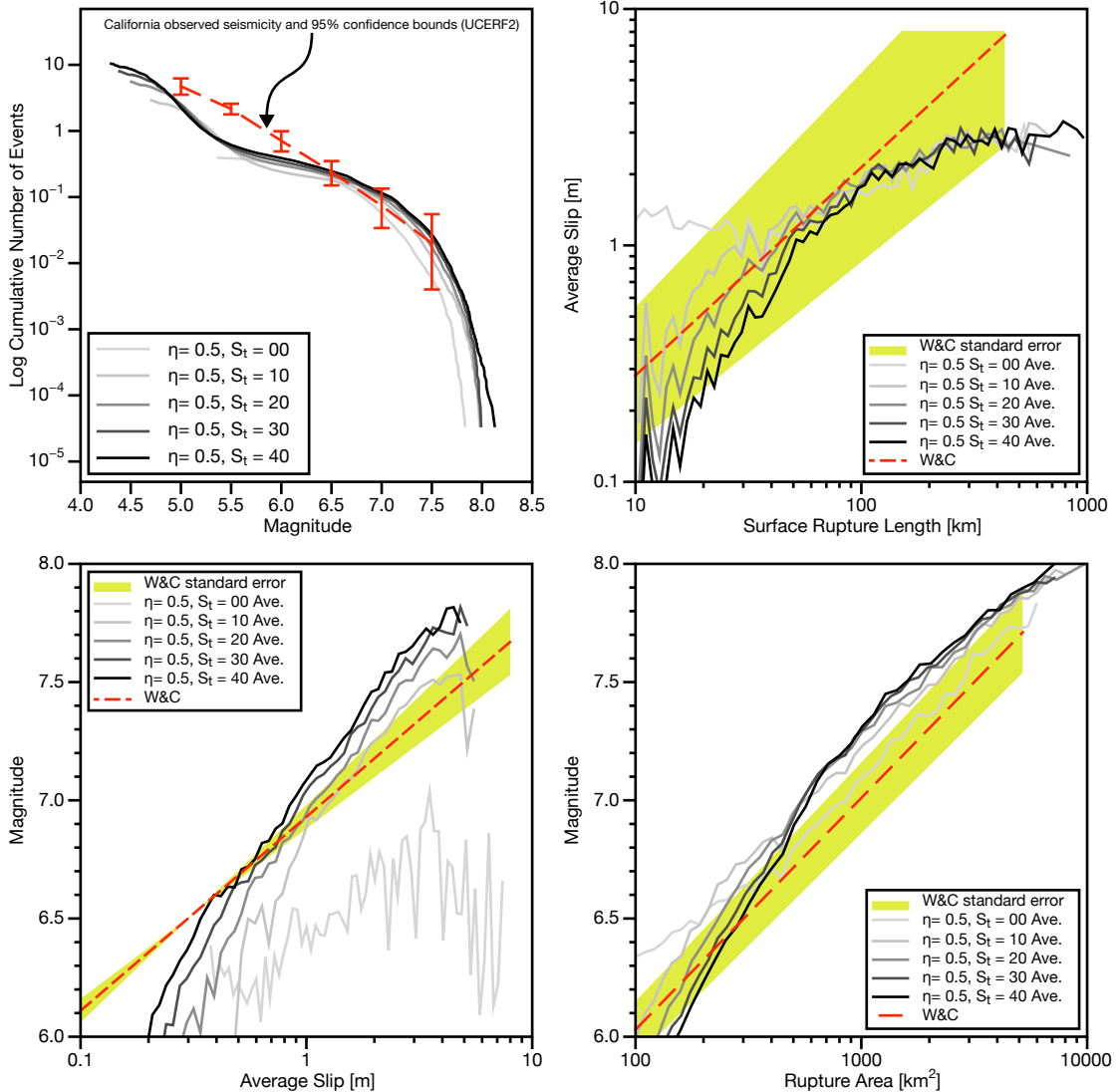


Figure 3.7: Examples of how varying the slip-scaling threshold S_t (Equation 3.5) effects Virtual California output. The observed values in the top-left frame are taken from UCERF2 [6]. The observed values in the remaining frames are taken from Wells and Coppersmith (W&C) [7].

processor recalculates the effects of this change on the stresses of their local elements and determines which (if any) ruptured. If any processors experience further ruptures the rupture propagation phase continues. This phase generally involves multiple propagation steps until the earthquake is finished. Once there are no more ruptures, the simulation returns to the long-term stress calculation. After the specified number of simulation years have elapsed the simulation is ended.

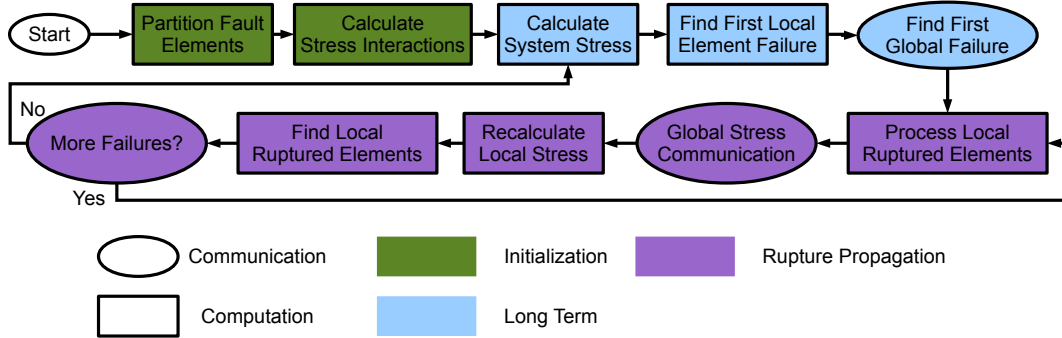


Figure 3.8: Execution flow of Virtual California on a parallel system.

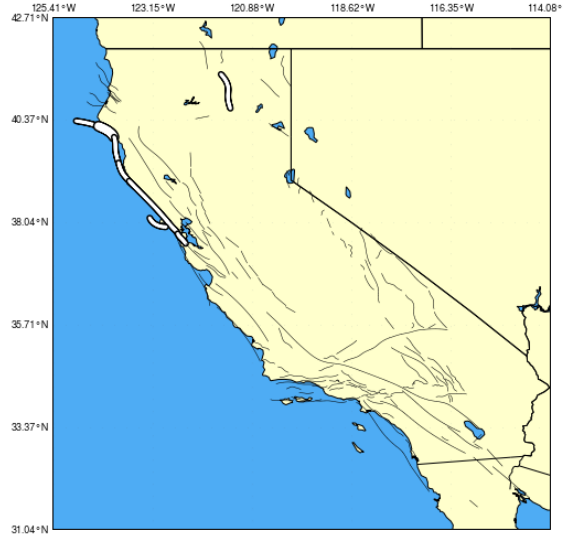
3.5 Virtual California Simulations

The output of Virtual California is a catalog of simulated events. Each event is essentially a list of ruptured elements and the stress and slip changes that occurred on each element during the event. An example of the slip on each element during an event on the northern San Andreas fault is shown in Figure 3.9. The $m \simeq 7.7$ event began on a section of the fault that lies off the coast of Cape Mendocino (the section named SAF-N_Mendocin in the figure). It then ruptured the rest of the northerly section of the fault and proceeded south through Sonoma and Marin county to just north of San Francisco. Most of the slip in the event occurred on the sections labeled SAF-N_Coast_Of and SAF-N_Coast_On. The fault off Point Reyes (Pt_Reyes) and the Hat Creek fault (Hat_Creek) which is north-east of Chico were also involved. The surface displacement generated by this event is shown in Figures 3.10 and 3.11.

Event 522851. Magnitude 7.669

1 SAF-Mendo_Offs

(40.356, -124.897)		(40.249, -124.423)	
0	4	8	12
1	5	9	13
2	6	10	14
3	7	11	15
4	12	16	20
5	17	21	25
6	22	26	30
7	27	31	35
8	39	43	47
9	50	54	58
10	59	63	67
11	70	74	78
12	75	79	83
13	87	91	95
14	99	103	107
15	111	115	119
16	117	121	125
17	129	133	137
18	141	145	149
19	153	157	161
20	165	169	173
21	177	181	185
22	189	193	197
23	197	201	205
24	213	217	221
25	225	229	233
26	237	241	245
27	249	253	257
28	261	265	269
29	273	277	281
30	285	289	293
31	297	301	305
32	309	313	317
33	321	325	329
34	331	335	339
35	341	345	349
36	351	355	359
37	361	365	369
38	371	375	379
39	381	385	389
40	391	395	399
41	401	405	409
42	411	415	419
43	421	425	429
44	431	435	439
45	441	445	449
46	451	455	459
47	461	465	469
48	471	475	479
49	481	485	489
50	491	495	499
51	501	505	509
52	511	515	519
53	521	525	529
54	531	535	539



2 SAF-N_Mendocin

(40.238, -124.391) (40.014, -124.047)

0	54	88	72	76	80	84	88	92	96	100	104	108	112
1	55	69	73	77	81	85	89	93	97	101	105	109	113
2	66	70	74	78	82	86	90	94	98	102	106	110	114
3	67	71	75	79	83	87	91	95	99	103	107	111	115
4	78	82	86	90	94	98	102	106	110	114	118	122	126
5	89	93	97	101	105	109	113	117	121	125	129	133	137
6	100	104	108	112	116	120	124	128	132	136	140	144	148
7	101	105	109	113	117	121	125	129	133	137	141	145	149
8	112	116	120	124	128	132	136	140	144	148	152	156	160
9	113	117	121	125	129	133	137	141	145	149	153	157	161
10	124	128	132	136	140	144	148	152	156	160	164	168	172
11	125	129	133	137	141	145	149	153	157	161	165	169	173
12	136	140	144	148	152	156	160	164	168	172	176	180	184
13	137	141	145	149	153	157	161	165	169	173	177	181	185
14	148	152	156	160	164	168	172	176	180	184	188	192	196
15	149	153	157	161	165	169	173	177	181	185	189	193	197
16	160	164	168	172	176	180	184	188	192	196	200		
17	161	165	169	173	177	181	185	189	193	197	201		
18	172	176	180	184	188	192	196	200	204	208	212	216	220
19	173	177	181	185	189	193	197	201	205	209	213	217	221
20	184	188	192	196	200	204	208	212	216	220	224	228	232
21	185	189	193	197	201	205	209	213	217	221	225	229	233
22	196	200	204	208	212	216	220	224	228	232	236	240	244
23	207	211	215	219	223	227	231	235	239	243	247	251	255
24	218	222	226	230	234	238	242	246	250	254	258	262	266
25	219	223	227	231	235	239	243	247	251	255	259	263	267
26	230	234	238	242	246	250	254	258	262	266	270		
27	241	245	249	253	257	261	265	269	273	277	281		
28	252	256	260	264	268	272	276	280	284	288	292		
29	263	267	271	275	279	283	287	291	295	299	303		
30	274	278	282	286	290	294	298	302	306	310	314		
31	285	289	293	297	301	305	309	313	317	321	325		
32	296	300	304	308	312	316	320	324	328	332	336		
33	307	311	315	319	323	327	331	335	339	343	347		
34	318	322	326	330	334	338	342	346	350	354	358		
35	329	333	337	341	345	349	353	357	361	365	369		
36	340	344	348	352	356	360	364	368	372	376	380		
37	351	355	359	363	367	371	375	379	383	387	391		
38	362	366	370	374	378	382	386	390	394	398	402		
39	373	377	381	385	389	393	397	401	405	409	413		
40	384	388	392	396	400	404	408	412	416	420	424		
41	395	399	403	407	411	415	419	423	427	431	435		
42	406	410	414	418	422	426	430	434	438	442	446		
43	417	421	425	429	433	437	441	445	449	453	457		
44	428	432	436	440	444	448	452	456	460	464	468		
45	439	443	447	451	455	459	463	467	471	475	479		
46	450	454	458	462	466	470	474	478	482	486	490		
47	461	465	469	473	477	481	485	489	493	497	501		
48	472	476	480	484	488	492	496	500	504	508	512		
49	483	487	491	495	499	503	507	511	515	519	523		
50	494	498	502	506	510	514	518	522	526	530	534		
51	505	509	513	517	521	525	529	533	537	541	545		
52	516	520	524	528	532	536	540	544	548	552	556		
53	527	531	535	539	543	547	551	555	559	563	567		

140 Pt_Reyes

(38.147, -123.222) (37.946, -122.888)

0	102	103	104	105	106	107	108	109	110	111	112	113	114	115	116	117	118	119	120	121	122	123	124	125	126	127	128	129	130	131	132	133	134	135	136	137	138	139	140	141	142	143	144	145	146	147	148	149	150	151	152	153	154	155	156	157	158	159	160	161	162	163	164	165	166	167	168	169	170	171	172	173	174	175	176	177	178	179	180	181	182	183	184	185	186	187	188	189	190	191	192	193	194	195	196	197	198	199	200	201	202	203	204	205	206	207	208	209	210	211	212	213	214	215	216	217	218	219	220	221	222	223	224	225	226	227	228	229	230	231	232	233	234	235	236	237	238	239	240	241	242	243	244	245	246	247	248	249	250	251	252	253	254	255	256	257	258	259	260	261	262	263	264	265	266	267	268	269	270	271	272	273	274	275	276	277	278	279	280	281	282	283	284	285	286	287	288	289	290	291	292	293	294	295	296	297	298	299	300	301	302	303	304	305	306	307	308	309	310	311	312	313	314	315	316	317	318	319	320	321	322	323	324	325	326	327	328	329	330	331	332	333	334	335	336	337	338	339	340	341	342	343	344	345	346	347	348	349	350	351	352	353	354	355	356	357	358	359	360	361	362	363	364	365	366	367	368	369	370	371	372	373	374	375	376	377	378	379	380	381	382	383	384	385	386	387	388	389	390	391	392	393	394	395	396	397	398	399	400	401	402

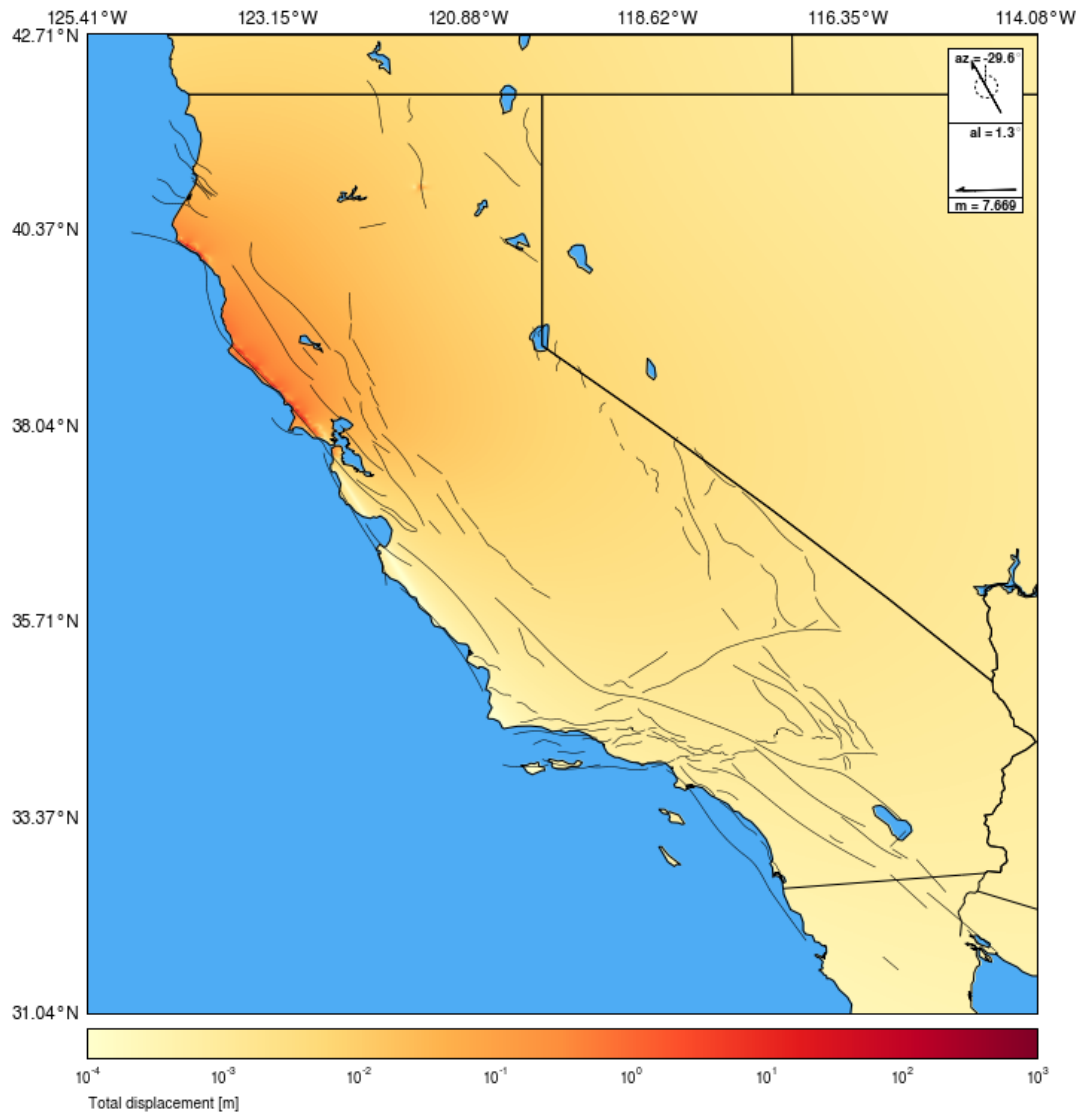


Figure 3.10: The surface displacement caused by the simulated $m \simeq 7.669$ event shown in Figure 3.9. The direction of the plotted displacement is shown in the upper right-hand corner of the figure. The direction is roughly looking north along the fault trace at surface level.

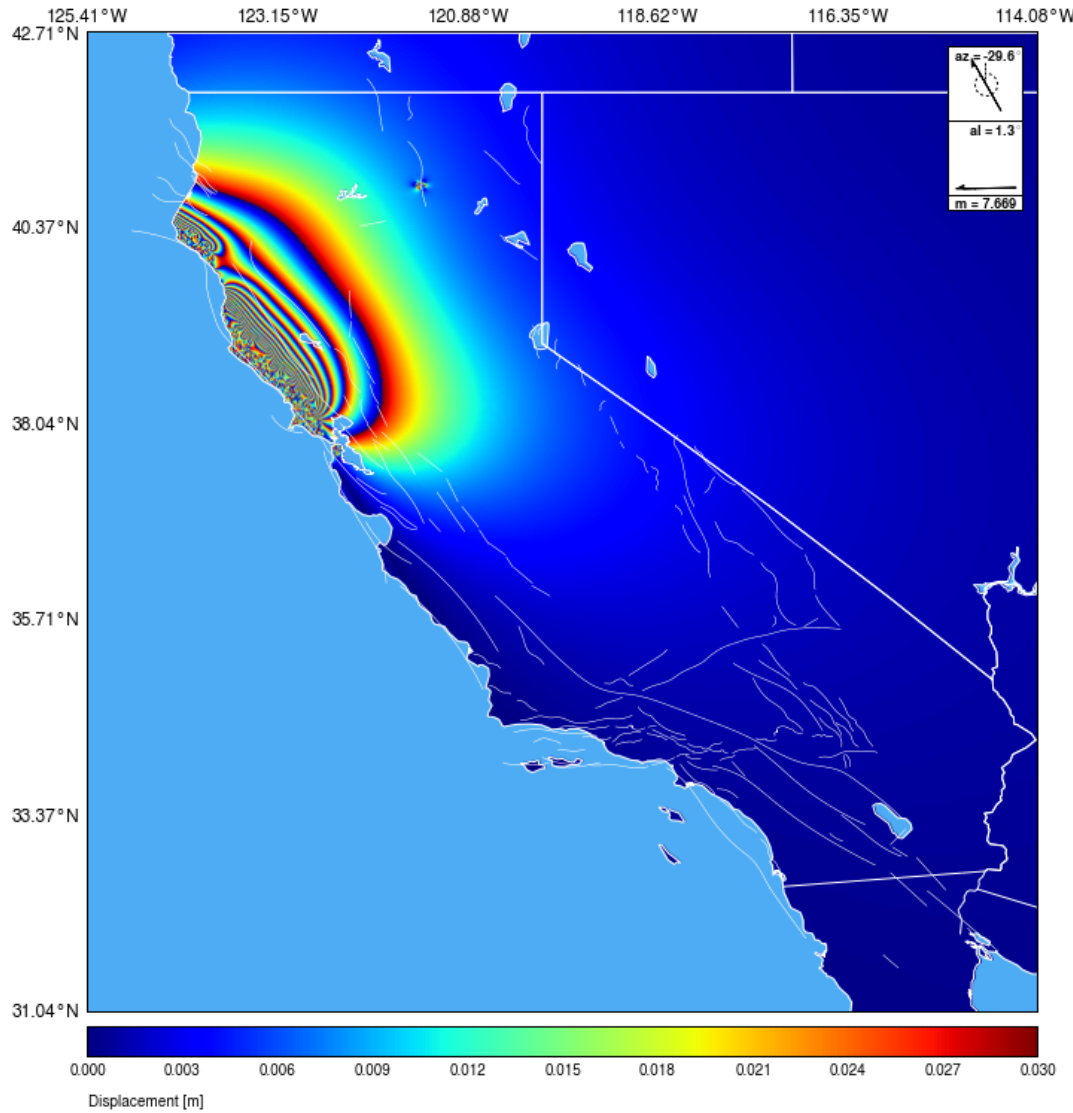


Figure 3.11: The surface displacement caused by the simulated $m \simeq 7.669$ event shown in Figure 3.9 plotted as interference fringes. This is a simulated InSAR interferogram. The direction of the plotted displacement is shown in the upper right-hand corner of the figure. The direction is roughly looking north along the fault trace at surface level.

Although individual events are interesting, it is the statistics of many events that we are after. To get a sense of how the entire system behaves over a long period of time, Figure 3.12 shows a magnitude histogram of all events, distributed across the fault sections on which they occurred. The timeframe represented in Figure 3.12 is 30,000 years, much longer than observed catalogs. There is a great deal of activity on the San Andreas fault (the bottom of the plot), but there are

some faults that never rupture. This is either because their slip rates are very low, their breaking stresses are very high, or some coincidental alignment with other fault sections causes very slow stress accumulation. All three of these factors could also be involved simultaneously. There is also a curious shape to the histogram that persists across all faults in the system. Most of the events that occurred in the simulation were either smaller (below about $m \simeq 5.5$) or larger (above about $m \simeq 6.4$). The reason for this stems from the fact that the magnitude of an event (m) is directly proportional to the surface area that ruptures [8]:

$$m = \frac{2}{3} \log(\mu S A) - 10.7 \quad (3.7)$$

where S is the average slip during the rupture, A is the surface area, μ is the shear modulus of the material and the logarithm is base 10. At the lower end of the magnitude scale in Figure 3.12, the events are comprised of a few isolated elements, each element having a surface area of 9km^2 . However, as the events become larger, they begin to become fault section sized events. Figure 3.13 shows a histogram of the surface areas of all the sections in the model (right) and histograms of the average slips for each event (left). Most events are small and have small average slip; in order to get a better sense of the average slip in larger events the bottom-left histogram only counts events in which 10 or more elements ruptured. The average surface area of fault sections in the model is $\sim 7.058 \times 10^8 \text{ m}^2$ and the average of the average slips of larger events is $\sim 1.17 \text{ m}$. If we plug these numbers into Equation 3.7 we get $m \simeq 6.9$, which roughly corresponds to the high magnitude region in Figure 3.12 where there is an increased number of events. Therefore, the relatively large number of larger events is due to a characteristic section size in the model. We will encounter this phenomena again when we compare the simulated catalog to observed seismicity in California.

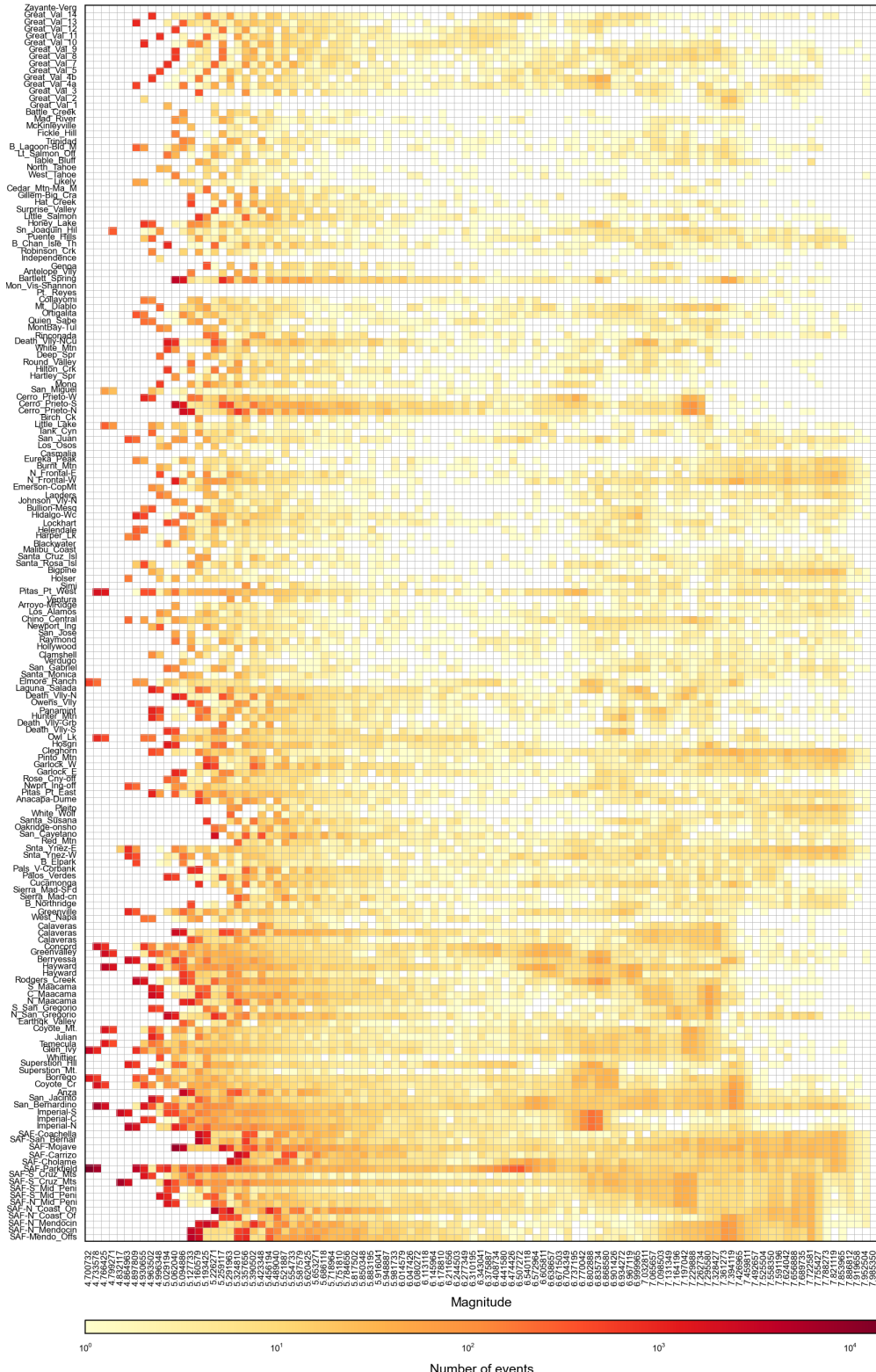


Figure 3.12: Histogram of event magnitude by fault section. The fault model used is the ALLCAL2 model described in Section 3.3.1. The simulation was run for 50,000 years with dynamic triggering $\eta = 0.8$ and slip-scaling threshold $S_t = 10$. The first and last 10,000 years were discarded leaving 30,000 years of events.

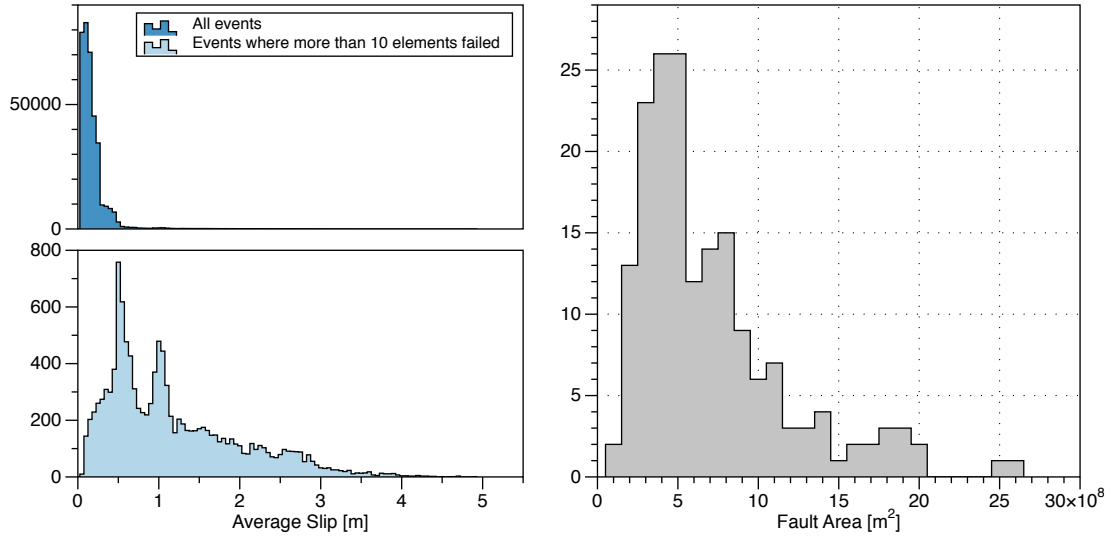


Figure 3.13: **Left** Histogram of average slip for events in a simulation of the ALLCAL2 model described in Section 3.3.1. The simulation was run for 50,000 years with dynamic triggering $\eta = 0.8$ and slip-scaling threshold $S_t = 10$. The first and last 10,000 years were discarded leaving 30,000 years of events. **Top left** All events. **Bottom left** Events that involved 10 or more elements. **Right** Histogram of fault areas for all fault sections in the ALLCAL2 model.

Another useful way to visualize the dynamics of the simulation is shown in Figure 3.14. This space-time plot shows time increasing on the vertical axis, and fault sections lined up along the horizontal axis. In Figure 3.14 we focus on only the sections that comprise the San Andreas fault. Each horizontal line on the plot represents the portions of a section that failed in an event. Large events are red while smaller events are yellow. The time-frame shown in Figure 3.14 is 500 years. There is a certain amount of periodicity in the rupture pattern – especially on the Parkfield section of the fault. It is interesting to note that, for all of the sections, large events are preceded by many smaller events that increase in frequency as the larger event is approached. This behavior – as well as the periodicity – is a result of the gradual stress buildup that can also be seen in Figure 3.5 top. Another consequence of the stress buildup and release cycle is that the model produces no aftershocks. This is encouraging because it is widely believed that aftershocks do not occur on main faults but in regions of small secondary fracture surrounding main faults [55]. Since Virtual California is a model of main faults only, the lack

of aftershocks is the expected behavior.

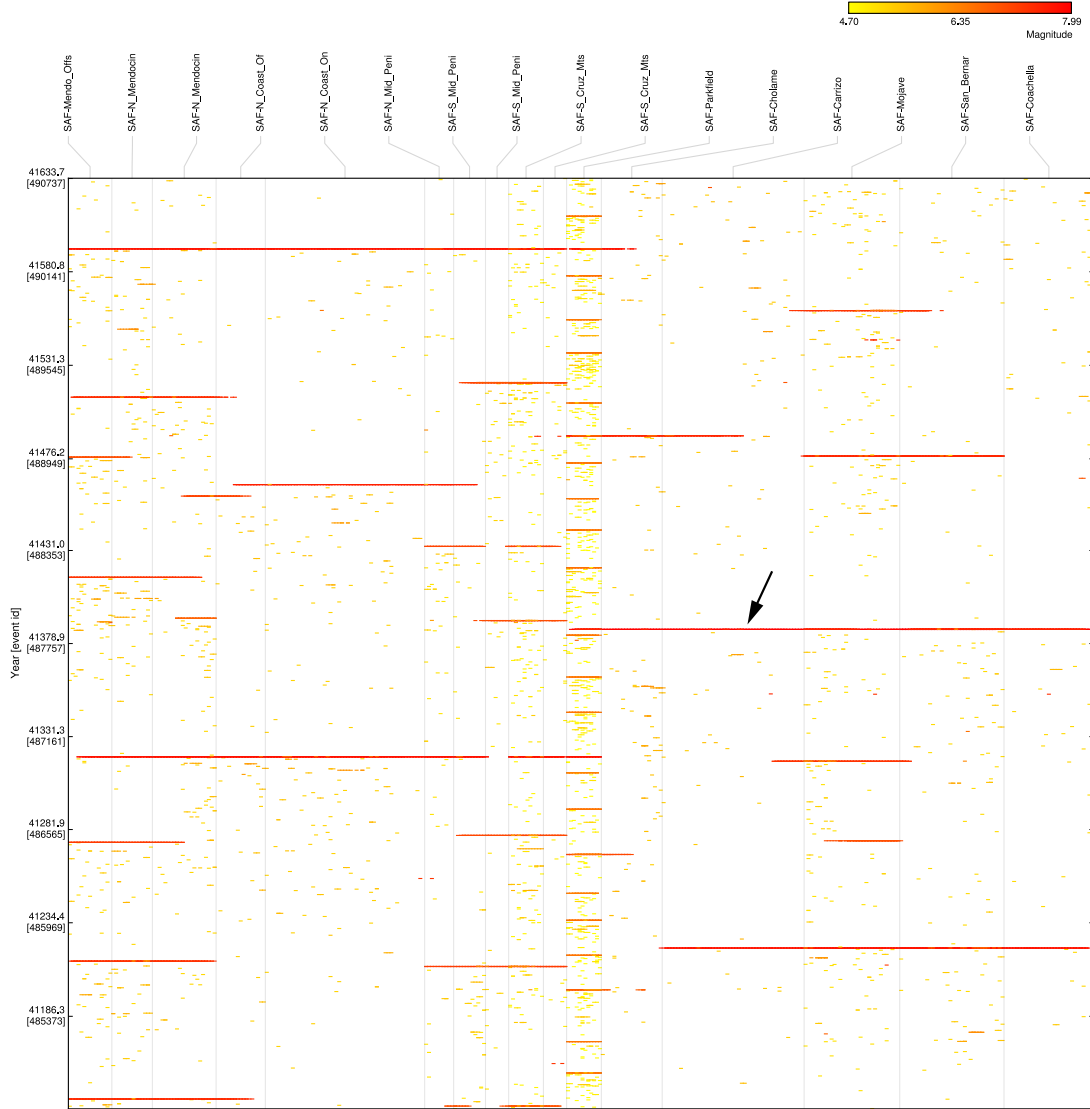


Figure 3.14: Space-time diagram of 500 years of activity on the San Andreas fault. The fault model used is the ALLCAL2 model described in Section 3.3.1. The simulation was run for 50,000 years with dynamic triggering $\eta = 0.8$ and slip-scaling threshold $S_t = 10$. The first and last 10,000 years were discarded leaving 30,000 years of events. This particular 500 years was selected because of the $m = 7.985$ event on the southern San Andreas at year 41384 (marked with the arrow). This is the largest event in the simulation.

The utility of any model of a physical system is dependent on how well the model reproduces the observed properties of the system. To test how well Virtual California reproduces the observed seismicity in California, a simulation using the

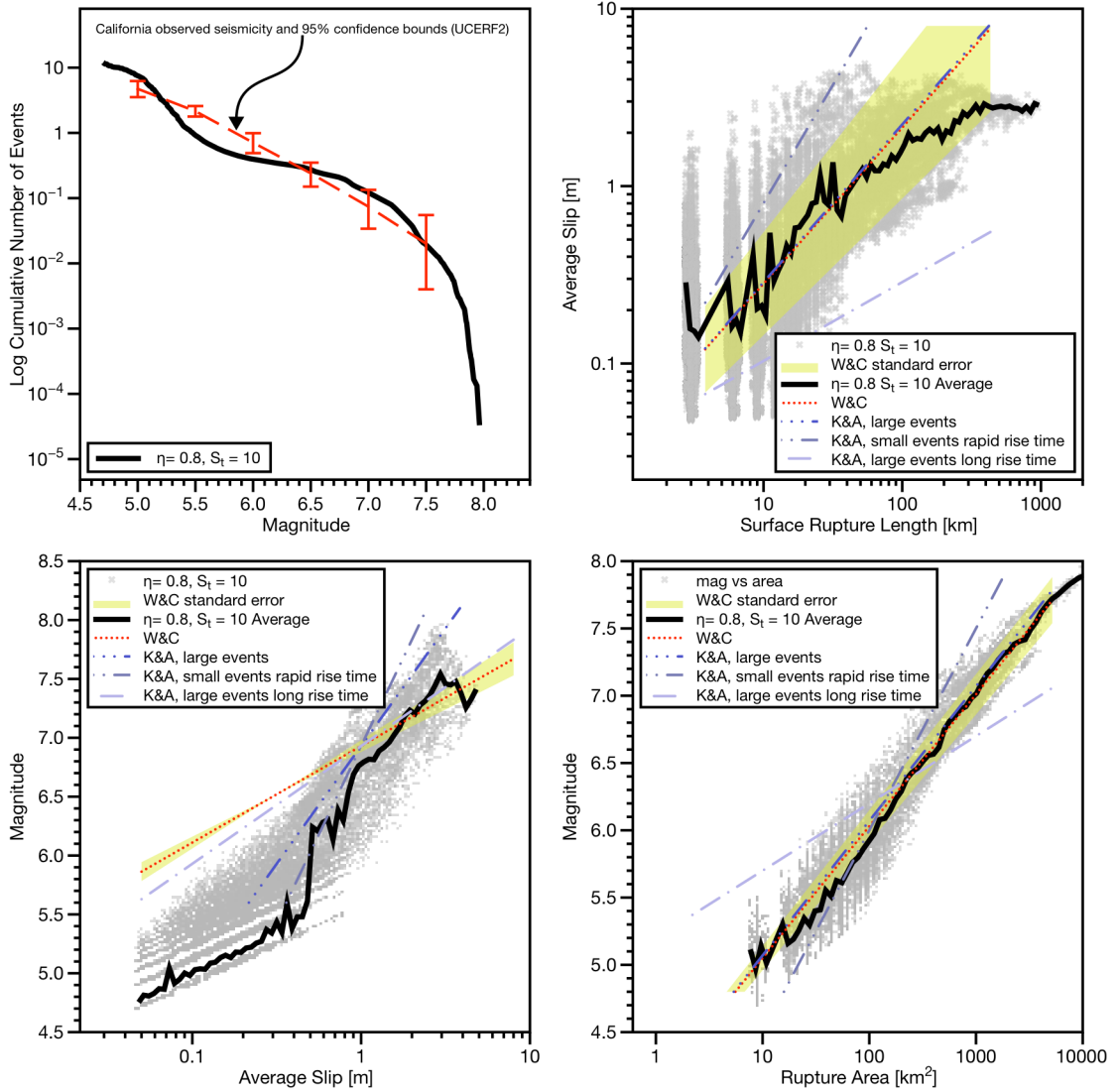


Figure 3.15: Scaling relations from a Virtual California simulation of the ALLCAL2 model described in Section 3.3.1. The simulation was run for 50,000 years with dynamic triggering $\eta = 0.8$ and slip-scaling threshold $S_t = 10$. The first and last 10,000 years were discarded leaving 30,000 years of events. In the figures, W&C are observed relations as reported by Wells and Coppersmith [7], and K&A are theoretical relationships as reported by Kanamori and Anderson [8]. UCERF2 are observations of seismicity in California as reported by Field et al. [6]. The scaling relationships are: **top left** frequency-magnitude, **top right** average slip-surface rupture length, **bottom left** magnitude-average slip, and **bottom right** magnitude-rupture area. In all of the plots except the frequency-magnitude plot, the heavy dark line is a binned average of the Virtual California events.

ALLCAL2 model described in Section 3.3.1 was run with a dynamic-triggering (Equation 3.6) of $\eta = 0.8$ and a slip-scaling threshold (Equation 3.5) of $S_t = 10$.

The simulation was run for 50,000 years and the first and last 10,000 years were thrown away resulting in a total of 30,000 years of events. Several different observations were used as basis for comparison. The first is the relationship between the number and magnitude of observed events, the Gutenberg-Richter frequency-magnitude relation [49]:

$$\log N_c = a - bM. \quad (3.8)$$

In Equation 3.8, N_c is the total number of earthquakes with magnitude greater than M , b is a near universal constant in the range $0.8 < b < 1.1$, and a is a measure of the level of seismicity. What Equation 3.8 tells us is that for every $\sim 10 M = 5.0$ earthquakes, for example, one can expect $\sim 1 M = 6.0$ earthquake. The Gutenberg-Richter relation for the results of the Virtual California simulations are shown in the top left frame of Figure 3.15. This figure shows that a $M \sim 7.6$ or larger earthquake is expected about every 100 years. Also shown in this figure is the observed seismicity in California as reported by UCERF2 [6]. Virtual California does well for events above $m \sim 6.3$, but here again we see the characteristic section size effect that was described above. The bulge at $m \sim 7.0$ is due to this effect, as is the dip at $m \sim 5.8$.

The next three quantities that Virtual California is compared against are the relationships between average slip and surface rupture length (top right frame in Figure 3.15), magnitude and average slip (bottom left frame in Figure 3.15), and magnitude and rupture area (bottom right frame in Figure 3.15). In each case the observations used are reported by Wells and Coppersmith (W&C) [7]. Also shown are comparisons to theoretically derived values as reported by Kanamori and Anderson (K&A) [8]. The Virtual California results (heavy black line in Figure 3.15) are the binned average of the events in the simulated catalog. In the case of the average slip vs. rupture length (top right frame in Figure 3.15) and magnitude vs. rupture area (bottom right frame in Figure 3.15) Virtual California compares well to both the observed (W&C) values and the theoretical (K&A) results for large

events – which according to [8] are the type of events that Virtual California should produce. In the case of the magnitude vs. average slip relationship (bottom left frame in Figure 3.15) both Virtual California and the theoretical results for large events differ from the observations. The reasons for this are not clear, however differences in how average slip is measured could be the cause.

The last comparison of Virtual California output to observed seismicity is a comparison of earthquake recurrence times, shown in Figure 3.16. In each case Virtual California events occur slightly more frequently than observations would suggest but are generally within the margin of error.

3.6 Virtual California on the Web

A major goal of the Virtual California project from the beginning, has been to make earthquake simulations available to researchers from all over the world. The Virtual California Web Interface (VCWI) was designed to meet this goal. A beta version is available here: http://mathewson.physics.ucdavis.edu/vc_browser/. A user interaction diagram which outlines all of the functionality of the VCWI is shown in Figure 3.17. The VCWI presents users with two ways to explore Virtual California simulations. The first is a view of the faults in the model (Figure 3.18). Users can either select fault sections from the map or from the searchable list. Once fault sections are selected, all of the scaling relations in Figure 3.15 and space-time plots like the one in Figure 3.14 can be produced for any time range in the simulation.

The second way to explore Virtual California simulations is through a list of all events in the simulation (Figure 3.19). From the list, rupture maps like the one in Figure 3.9 can be produced for each event in the system.

3.7 Conclusion

Understanding earthquake behavior is crucial to disaster prevention and management. The Virtual California program helps perform ensemble domain simulations which are statistically similar to actual earthquakes and will aid in prediction and understanding of earthquakes in the future.

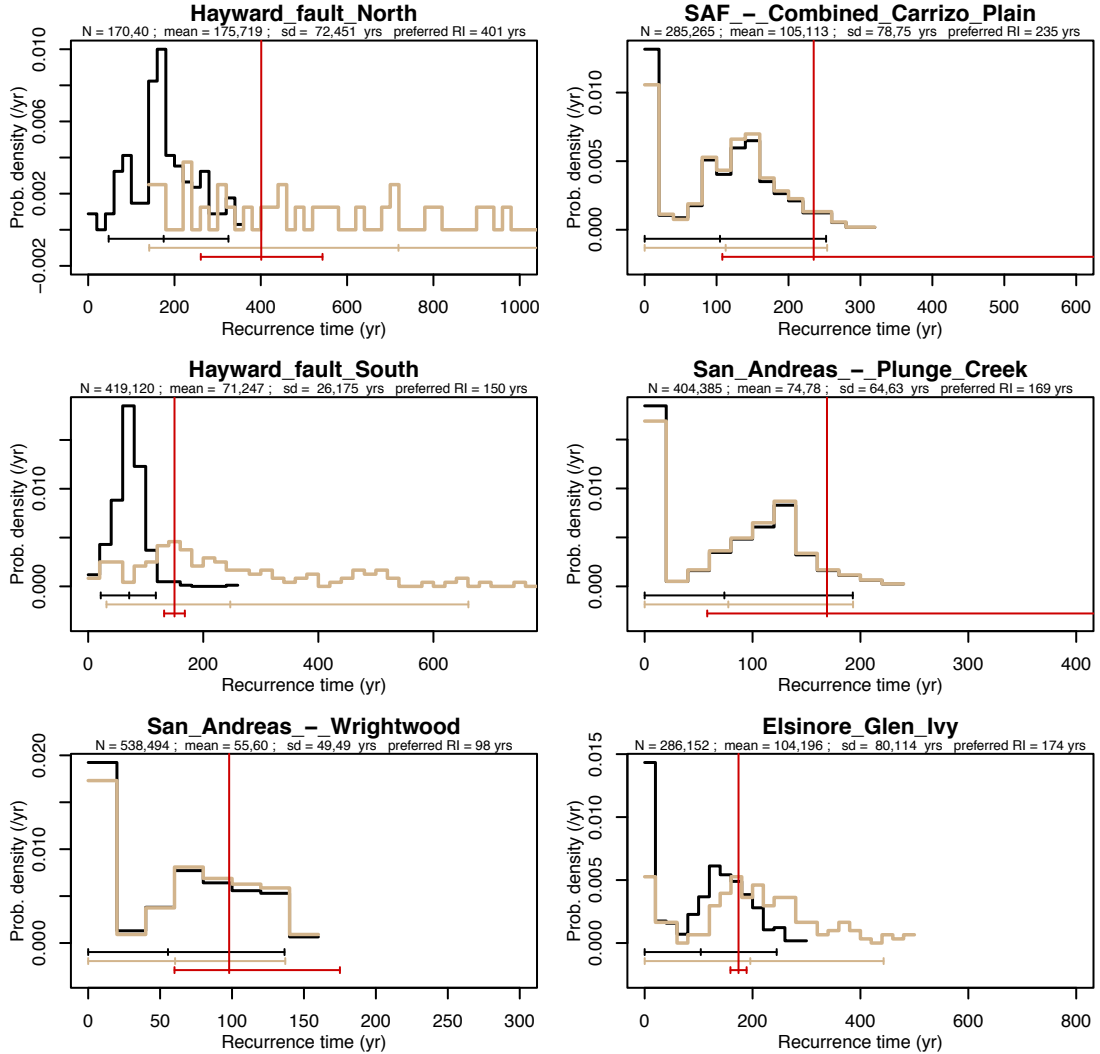


Figure 3.16: Observed recurrence intervals compared to simulated recurrence intervals for the ALLCAL2 model described in Section 3.3.1. The simulation was run for 50,000 years with dynamic triggering $\eta = 0.8$ and slip-scaling threshold $S_t = 10$. The first and last 10,000 years were discarded leaving 30,000 years of events. The observed intervals are taken from a compilation of observations in [6].

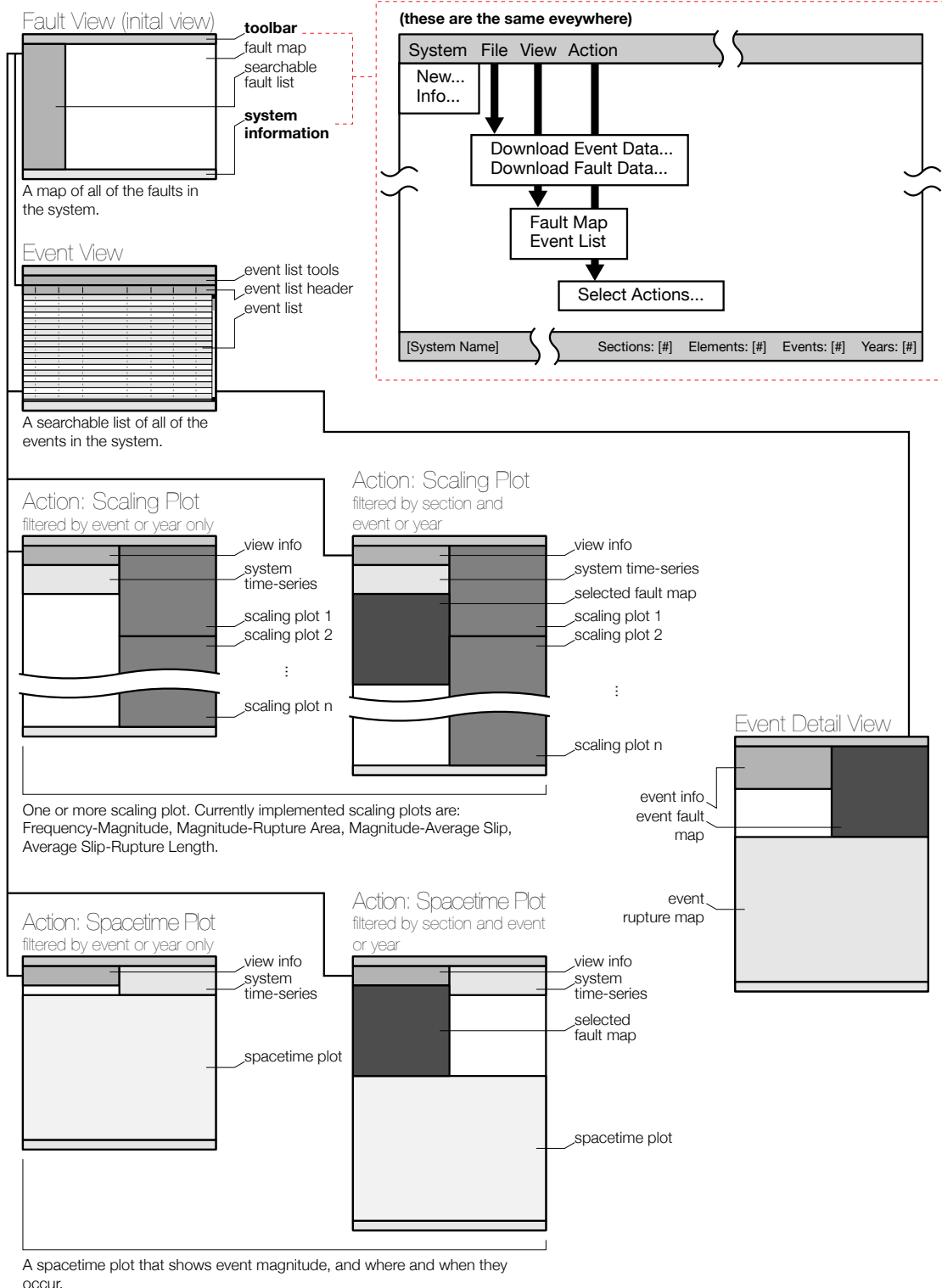


Figure 3.17: The user interaction diagram showing the functionality of the Virtual California Web Interface.

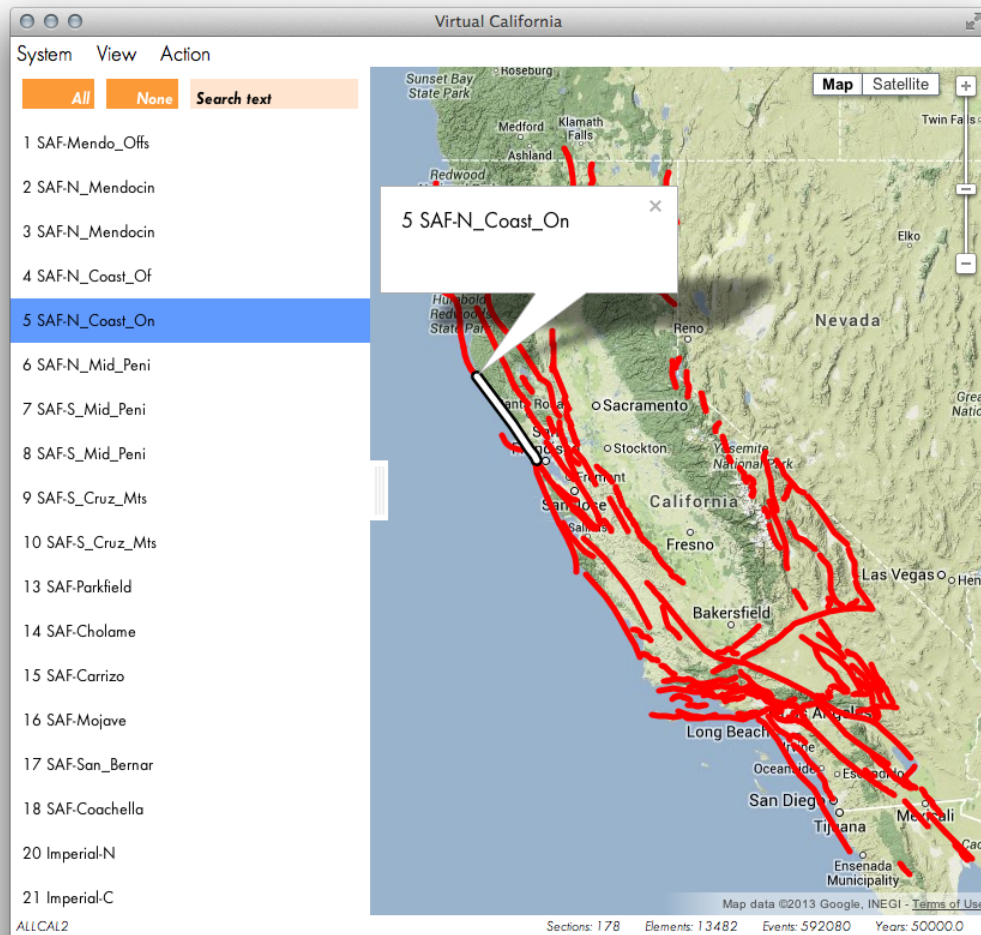


Figure 3.18: The fault view from the Virtual California Web Interface.

Virtual California

All None 1 2 3 4 5 6 7 8 9 10 11 12 13 14 15 16 17 18 19 20 21 22 ... ► ► 1000 ▾

Number	Year	Magnitude	Trigger Section	Trigger Element	# of Sections Involved	# of Elements Involved	Average Slip [m]
487847	41384.766	7.985	SAF-Cholame	828	25	1391	2.820
15567	1939.663	7.977	SAF-Mojave	1148	23	1421	2.748
340149	29122.535	7.964	SAF-Mojave	1093	33	1239	3.003
219715	19031.117	7.963	SAF-Mojave	1048	32	1264	2.934
244191	21078.275	7.951	SAF-Cholame	768	29	1094	3.287
145047	12812.516	7.945	SAF-Mojave	1057	26	1208	2.836
189845	16546.021	7.941	SAF-S_Cruz_Mts	643	30	1238	2.773
437591	37203.906	7.913	SAF-Mojave	1144	32	1175	2.583
564069	47661.301	7.910	SAF-N_Coast_On	377	27	979	3.191
473522	40197.730	7.907	SAF-Mojave	1069	31	1187	2.510
184914	16129.831	7.907	SAF-S_Cruz_Mts	614	26	1094	2.814
285158	24517.592	7.905	SAF-Mojave	1106	28	1132	2.647
546971	46289.242	7.904	SAF-Cholame	824	22	1048	2.819
376258	32146.684	7.902	SAF-Mojave	1060	27	1022	2.881
576752	48713.059	7.897	SAF-Mojave	1085	25	1060	2.731
201684	17550.422	7.896	SAF-Mojave	1112	27	1124	2.579
571167	48253.125	7.894	SAF-Mojave	1148	22	1063	2.692
367306	31392.236	7.893	SAF-Carrizo	972	23	1059	2.677
85203	7851.097	7.887	SAF-Mojave	1100	21	995	2.820
153069	13485.552	7.887	SAF-Mojave	1150	30	1052	2.644
238319	20602.855	7.884	SAF-San_Bernar	1348	22	1047	2.651
321552	27578.883	7.881	SAF-N_Coast_On	396	22	1087	2.608
172087	15058.176	7.876	SAF-Carrizo	977	23	978	2.754
ALLCAL2							

Sections: 178 Elements: 13482 Events: 592080 Years: 50000.0

Figure 3.19: The list view from the Virtual California Web Interface.

Chapter 4

Forecast Verification

Earthquake forecasts have long lagged behind forecasts of other extreme natural events like hurricanes and tornados. As mentioned in previous chapters, this is largely due to the difficulties involved in observing the forces that cause earthquakes. However, the hazard posed by earthquakes is of serious concern, so some type of reliable forecasting is needed. In 2006 the first competitive test of earthquake forecasts – the Regional Earthquake Likelihood Models (RELM) test – began. The forecasts were to be of the period between 2006 and 2010 for all of California. After the time-period was over, some technique of evaluating the success of the forecasts was needed. Several different approaches were proposed [94–96]. The approach outlined here was borrowed from meteorologic (particularly tornado) forecast verification. It has the advantage of separating the number of events forecast from their locations. This work is a compilation of papers published in several places between 2011 and 2012 [97–100].

4.1 Introduction

Prospective forecasts of earthquakes are forecasts of earthquakes that may occur in the future. Retrospective forecasts are forecasts of earthquakes that have already occurred. In principal, a retrospective forecast can be carried out fairly. However, in many cases, the retrospective forecasts are based implicitly or explicitly on the occurrence of the forecast earthquakes.

An example of successful retrospective forecasts are those based on accelerated moment release (AMR). A systematic increase in Benioff strain is observed prior to an earthquake. Examples of AMR have been given by Bufe and Varnes [101] and Bowman et al. [102] among others. However, the epicenters of the subsequent earthquakes are used to define the regions in which AMR occurs. Hardebeck et al. [103] have argued that it is not possible to establish AMR without knowing the locations of the subsequent earthquakes, thus AMR cannot be used for prospective forecasting.

A primary example of prospective forecasts has been the sequence of forecasts issued by the International Institute for the Theory of Prediction and Theoretical Geophysics in Moscow. Their forecast algorithms are based on pattern recognition of regional seismicity [104, 105]. Increased rates of occurrence of intermediate magnitude earthquakes are the primary components of their forecasts, thus they have a similarity to AMR. When a threshold of anomalous behavior is reached, a time of increased probability (TIP) is issued. These are alarm based forecasts. TIPs were released prior to the $m = 6.9$ Armenian earthquake on 7 December 1988 and prior to the $m = 6.9$ Loma Prieta earthquake on 17 October 1989. Over a period of some 25 years successful TIPs were issued prior to 42 of 47 targeted earthquakes [106]. However, the results have been subject to criticism. Notable earthquakes were not predicted and there were too many false alarms [107].

Another example of a prospective forecast of earthquake occurrence was made for $m > 5$ earthquakes in California for the period 2000 - 2010 by Rundle et al. [108]. This was also an alarm based forecast. Earthquakes were forecast to occur in specified “hot spots”. Holliday et al. [109] reported that 16 of 18 $m \geq 5$ earthquakes that occurred during the period 2000 - 2005 occurred in hot spot regions. This forecast was based on the pattern informatics (PI) approach. Precursory seismic activation and quiescence were quantified and when variations exceeded a prescribed threshold “hot spots” were specified. Forecasts were made for $0.1^\circ \times 0.1^\circ$ cells (about $11 \text{ km} \times 11 \text{ km}$) which corresponded roughly to the rupture

length of an $m \simeq 6$ earthquake. Precursory seismicity included in the PI approach included $m \geq 3$ earthquakes. The size of the cells and magnitudes of earthquakes scale with AMR studies [110].

A closely related forecasting technique is the relative intensity (RI) approach. The RI forecast is based on the direct extrapolation of the rate of occurrence of small earthquakes using Gutenberg-Richter frequency-magnitude scaling. Shcherbakov et al. [111] tested the RI method globally. The success of the PI method described above led to a discussion as to whether the PI method is significantly better than the RI method. Comparisons of these approaches have come to different conclusions regarding their validity [112, 113].

Earthquakes are complex phenomena but they obey several scaling laws. One example is Gutenberg-Richter frequency-magnitude scaling. The cumulative number of earthquakes $N_{cumulative}$ with magnitudes greater than M in a region over a specified time are well approximated by the relation

$$\log N_{cumulative} = a - bM \quad (4.1)$$

where b is a near universal constant in the range $0.8 < b < 1.1$ and a is a measure of the level of seismicity. Equation 4.1 can be used to estimate the risk of large earthquakes based on the rate of occurrence of small earthquakes. This is a primary basis for the time independent seismic risk assessment. It is also the basis for the RI forecasts described above. An essential question is the role of the time dependance of the background seismicity in forecasting future earthquakes.

In order to test earthquake forecasts it is clearly desirable to use prospective forecasts. In order for a prospective forecast test to be useful it should be carried out in a reasonable length of time, say five years, and a reasonable number of earthquakes should be expected to occur. In order to meet these criteria the Regional Earthquake Likelihood Models (RELM) test was developed and carried out. The test region was California and adjacent regions.

Forecasts were solicited for $M > 5$ earthquakes during the period 2006 to

2010. It is the purpose of this chapter to discuss these forecasts in terms of the earthquakes that actually occurred. The forecasts involve both the number of earthquakes that will occur during the test period and their locations. We present a method that separates these two aspects of the forecasts. Forecasts were required to give the numbers of earthquakes that were expected to occur in 7682 $0.1^\circ \times 0.1^\circ$ spatial cells and 41 magnitude bins. We convert these forecast numbers to a conditioned probability that an earthquake would occur in a specified spatial cell and magnitude bin in the test region during the test period. Forecasts were solicited for main shock only and for main shocks plus aftershocks. We will show that the submitted forecasts for the two cases gave the same conditional probabilities. We will also show that the conditional probabilities have either no dependence or a weak dependence on the magnitude of the forecast earthquakes.

In Section 4.2 of this chapter we give the details of the RELM test. In Section 4.3 we discuss the earthquakes that occurred in the test region during the test period. The $M = 7.2$ El Mayor-Cucapah earthquake on 4 April 2010 was particularly important. In Section 4.4 we discuss the submitted forecasts. In Section 4.5 we evaluate the performance of the forecasts. We conclude that no single performance measure can be used to measure the success of a submitted forecast. In Section 4.6 we compare the performance of the submitted forecasts on the basis of the submitted probability that an earthquake would occur in a specified cell. The sum of these probabilities is unity so that the allocation of the probabilities between cells distinguishes the good forecasts from the bad forecasts. Finally, in Section 4.7 we summarize our results.

4.2 RELM test

In order to test methods for forecasting future earthquakes the Southern California Earthquake Center (SCEC) formed the working group for Regional Earthquake Likelihood Models (RELM) in 2000 [114]. For the first time a competitive test of prospective earthquake forecasts was to be carried out. Research groups were

encouraged to submit forecasts of future earthquakes in California. At the end of the test period, the forecasts would be compared with the actual earthquakes that occurred.

The ground rules for the RELM test were as follows:

1. The test region to be studied was the state of California, however the selected region extended somewhat beyond the boundaries of the state as shown in Figure 4.1.
2. A five year time period for the test was selected extending from 1 January 2006 to 31 December 2010. Earthquakes with $M \geq 4.95$ were to be forecast. For California, in years with major aftershock sequences, the level of seismicity is well approximated by GR scaling from Equation 4.1 taking $b = 1$ and $a = 5.4$ per year [110]. The number of $m > 5$ earthquakes expected per year would be 2.5 or 12.5 for 5 years. For $M \geq 6$, only about one earthquake would be expected, so the 5 year period would be much too short. The applicable magnitudes were taken from the Advanced National Seismic System (ANSS) on-line catalog <http://www.ncedc.org/anss/anss-detail.html>.
3. Participants were required to submit the number of earthquakes expected to occur in specified spatial cells and magnitude bins during the test period. The test region was subdivided into $N_c = 7682$ spatial cells with dimensions $0.1^\circ \times 0.1^\circ$ (approximately 11 km \times 11 km). These spatial cells were further divided into 41 magnitude bins: $4.95 \leq M < 5.05$, $5.05 \leq M < 5.15$, $5.15 \leq M < 5.25$, ..., $8.85 \leq M < 8.95$, $8.95 \leq M < \infty$. The participants were required to specify the expected number of earthquakes N_{emi} in magnitude bin m that would occur during the test period in cell i .
4. Participants could submit forecasts that included all earthquakes in the test region as well as forecasts that excluded aftershocks.

Seventeen forecasts were submitted by eight groups. Before discussing these

forecasts in some detail we will discuss the earthquakes that occurred in the test region during the test period with $M \geq 4.95$.

4.3 The Earthquakes

During the test period 1 January 2006 to 31 December 2010, there were $N_e = 31$ earthquakes in the test region with $M \geq 4.95$. The times of occurrence, locations, and magnitudes of these earthquakes are given in Table 4.1. The locations of the test earthquakes are also shown in Figures 4.1 - 4.4. The earthquakes are identified by the event numbers given in Table 4.1.

Table 4.1: Times of occurrence, locations, and magnitudes of the 31 earthquakes in the test region with $M \geq 4.95$ from 1 January 2006 until 31 December 2010. The $M = 7.2$ El Mayor-Cucapah earthquake is in bold.

No.		Origin Time (UTC)	Lat.	Long.	M
1	2006/05/24	04:20:26.01	32.3067	-115.2278	5.37
2	2006/07/19	11:41:43.46	40.2807	-124.4332	5.00
3	2007/02/26	12:19:54.48	40.6428	-124.8662	5.40
4	2007/05/09	07:50:03.83	40.3745	-125.0162	5.20
5	2007/06/25	02:32:24.62	41.1155	-124.8245	5.00
6	2007/10/31	03:04:54.81	37.4337	-121.7743	5.45
7	2008/02/09	07:12:04.55	32.3595	-115.2773	5.10
8	2008/02/11	18:29:30.53	32.3272	-115.2568	5.10
9	2008/02/12	04:32:39.24	32.4475	-115.3175	4.97
10	2008/02/19	22:41:29.66	32.4325	-115.3130	5.01
11	2008/04/26	06:40:10.60	39.5253	-119.9289	5.00
12	2008/04/30	03:03:06.90	40.8358	-123.4968	5.40
13	2008/07/29	18:42:15.71	33.9530	-117.7613	5.39
14	2008/11/20	19:23:00.19	32.3288	-115.3318	4.98
15	2008/12/06	04:18:42.85	34.8133	-116.4188	5.06
16	2009/09/19	22:55:17.84	32.3707	-115.2612	5.08

17	2009/10/01	10:01:24.67	36.3878	-117.8587	5.00
18	2009/10/03	01:16:00.31	36.3910	-117.8608	5.19
19	2009/12/30	18:48:57.33	32.4640	-115.1892	5.80
20	2010/01/10	00:27:39.32	40.6520	-124.6925	6.50
21	2010/02/04	20:20:21.97	40.4123	-124.9613	5.88
22	2010/04/04	22:40:42.15	32.2587	-115.2872	7.20
23	2010/04/04	22:50:17.08	32.0972	-115.0467	5.51
24	2010/04/04	23:15:14.24	32.3000	-115.2595	5.43
25	2010/04/04	23:25:06.95	32.2462	-115.2978	5.38
26	2010/04/05	00:07:09.07	32.0180	-115.0172	5.32
27	2010/04/05	03:15:24.46	32.6282	-115.8062	4.97
28	2010/04/08	16:44:25.92	32.2198	-115.2760	5.29
29	2010/06/15	04:26:58.48	32.7002	-115.9213	5.72
30	2010/07/07	23:53:33.53	33.4205	-116.4887	5.43
31	2010/09/14	10:52:18.00	32.0485	-115.1982	4.96

The major earthquake that occurred during the test period was the $M = 7.2$ El Mayor-Cucapah earthquake on 4 April 2010 (event #22 in Table 4.1). This earthquake was on the plate boundary between the North American and Pacific plates. The epicenter was about 50 km south of the Mexico-United States border, and the aftershocks indicate a rupture zone with a length of about 75 km. Both the epicenter and the aftershock sequence are illustrated in Figure 4.2.

The earthquakes within a $0.5^\circ \times 0.5^\circ$ region centered on the epicenter are illustrated in Figure 4.3. The El Mayor earthquake and the test earthquakes that occurred later, 4 April 2010 to 31 December 2010 are given in Figure 4.3b. Because of their proximity to the El Mayor earthquake in both space and time, events 23, 24, 25, 26, 28, and 31 are almost certainly aftershocks. The El Mayor earthquake and the test earthquakes that occurred earlier, 1 January 2006 to 3 April 2010 are

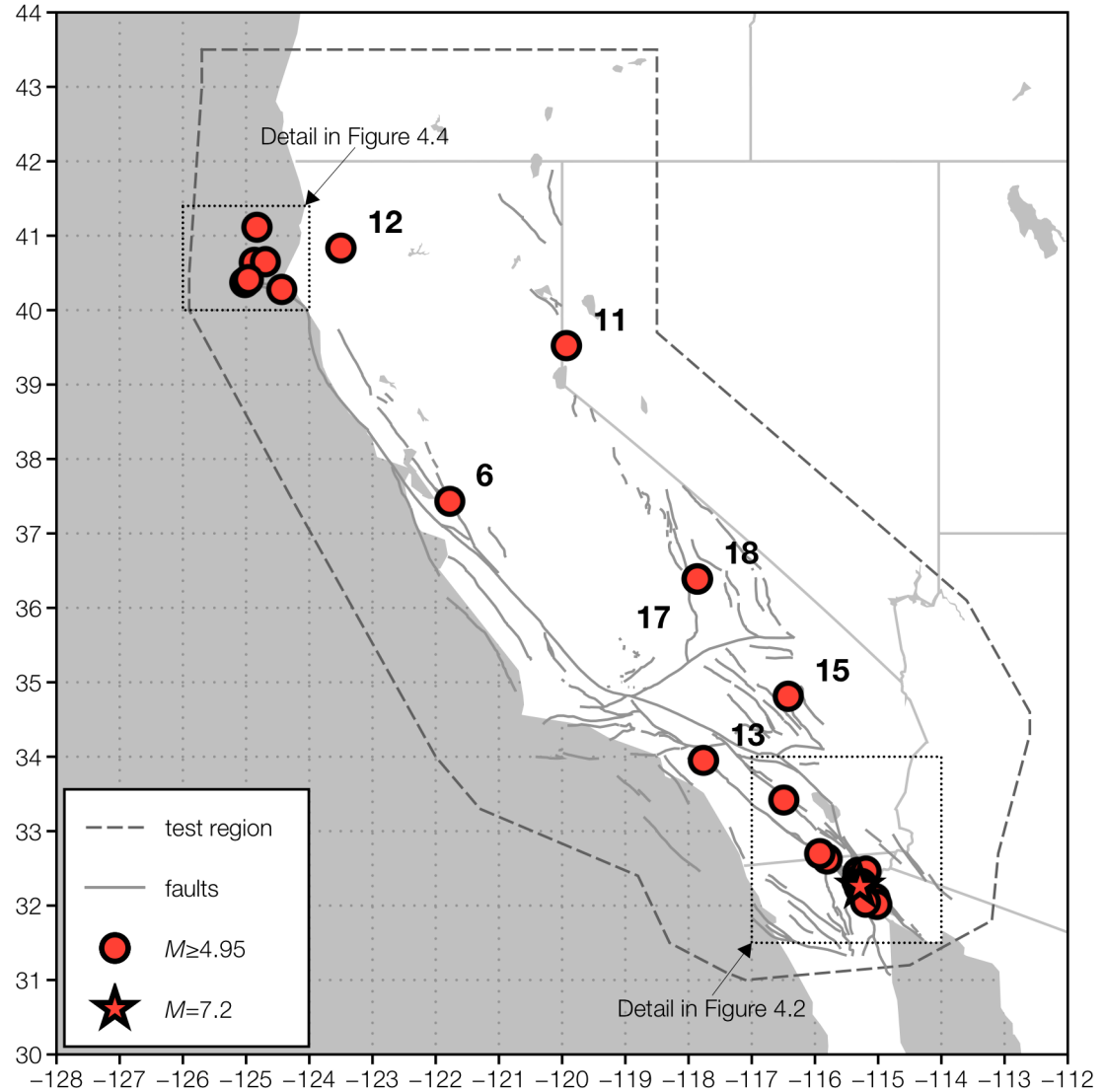


Figure 4.1: Map of the test region, the coast of California, major faults, and the 31 earthquakes with $M \geq 4.95$ that occurred in the test region. The earthquakes are listed in Table 4.1. Also shown are the square regions where large scale maps are given in Figures 4.2 to 4.4.

given in Figure 4.3a. Events 1, 7, 8, 9, 10, 14, 16, and 19 constitute a precursory swarm of eight test earthquakes in this region in the magnitude range 4.97 to 5.80, including four in the 10 day period between 9 February and 19 February 2008 (events 7—10). These events are located some 5 km to 20 km north of the subsequent epicenter of the El Mayor-Cucapah earthquake and lie outside the primary aftershock region of that event, as illustrated in Figure 4.3a. This swarm

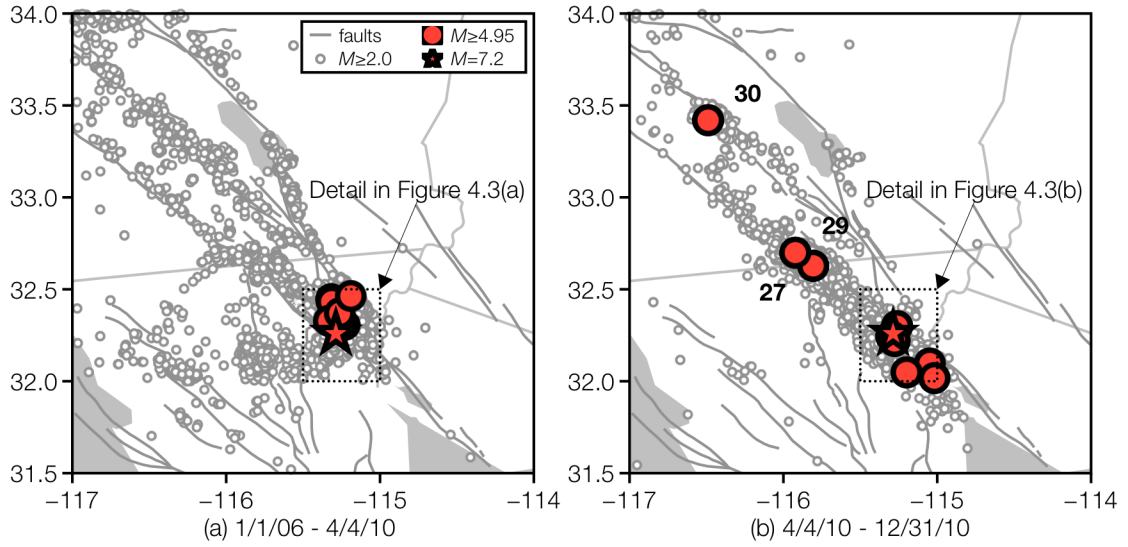


Figure 4.2: Map of the southeast region around the epicenter of the $M = 7.2$ El Mayor-Cucapah earthquake that occurred on 4 April 2010 (event #22 in Table 4.1, shown as a star). (a) Earthquakes during the period 1 January 2006 through 3 April 2010. (b) Earthquakes during the period 4 April 2010 through 31 December 2010 (includes aftershocks). Included are the test earthquakes given in Table 4.1 as well as background earthquakes with $M \geq 2.0$. More details in the square region are given in the larger scale maps in Figure 4.3.

of earthquakes certainly cannot be considered foreshocks, due to their relatively small magnitudes and early occurrence, but may represent a seismic activation. Foreshocks are by definition main shocks followed by a larger triggered aftershock [115]. Thus foreshocks have magnitudes that are statistically close to the following main shock [116].

The locations of the earthquakes given in Table 4.1 identify the $0.1^\circ \times 0.1^\circ$ cells in which the earthquakes occurred. These cells are illustrated in Figure 4.3. Cells in which earthquakes occurred are identified by capital letters. Earthquakes in Figure 4.3a occurred in cells A, G, N, K, and Q. Earthquakes in Figure 4.3b occurred in cells A, Q, R, and V. The association of earthquake event numbers with cell letters is given in Table 4.2. The occurrence of five test earthquakes in cell A is not surprising since this is the Cerro Prieto geothermal area that is recognized as having a high level of seismic activity.

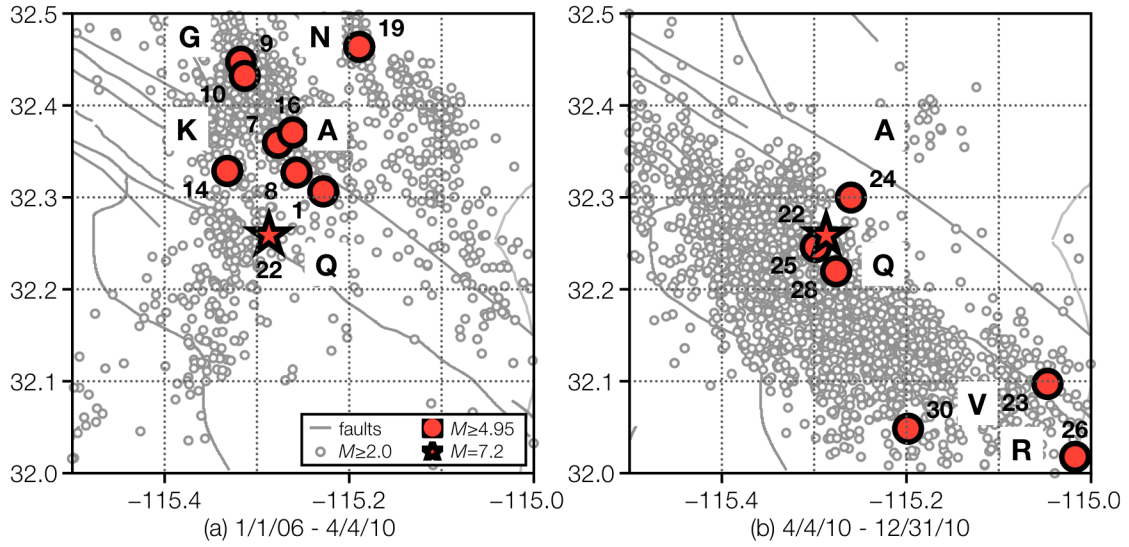


Figure 4.3: Map of the region in the immediate vicinity of the epicenter of the $M = 7.2$ El Mayor-Cucapah earthquake. (a) Earthquakes during the period 1 January 2006 through 3 April 2010. (b) Earthquakes during the period 4 April 2010 through 31 December 2010. Included are the test earthquakes given in Table 4.1 as well as background earthquakes with $M \geq 2.0$. The association of lettered $0.1^\circ \times 0.1^\circ$ cells in which earthquakes occurred with the numbered earthquakes is illustrated.

We next turn to the somewhat larger region ($3.0^\circ \times 2.5^\circ$) illustrated in Figure 4.2. The El Mayor earthquake and the test earthquakes that occurred later, 4 April 2010 to 31 December 2010 are given in Figure 4.2b. The aftershock region of the El Mayor-Cucapah earthquake is clearly illustrated, and events 27 and 29 are almost certainly aftershocks. Event 30 may or may not be an aftershock. The El Mayor earthquake and the test earthquakes that occurred earlier, 1 January 2006 to 3 April 2010 are given in Figure 4.3a. During this period no test earthquakes occurred outside the smaller region considered in Figure 4.3a.

We next consider the $2^\circ \times 1.4^\circ$ region adjacent to Cape Mendocino, illustrated in Figure 4.4. Six test earthquakes occurred in this region (events 2, 3, 4, 5, 20, and 21) in the magnitude range 5.0 to 6.5. This is a region of high seismicity, and this concentration of events is expected. Event 21 may or may not be an aftershock of event 20.

There were seven test earthquakes that occurred outside of the regions considered above. These are illustrated in Figure 4.1, and their magnitudes ranged

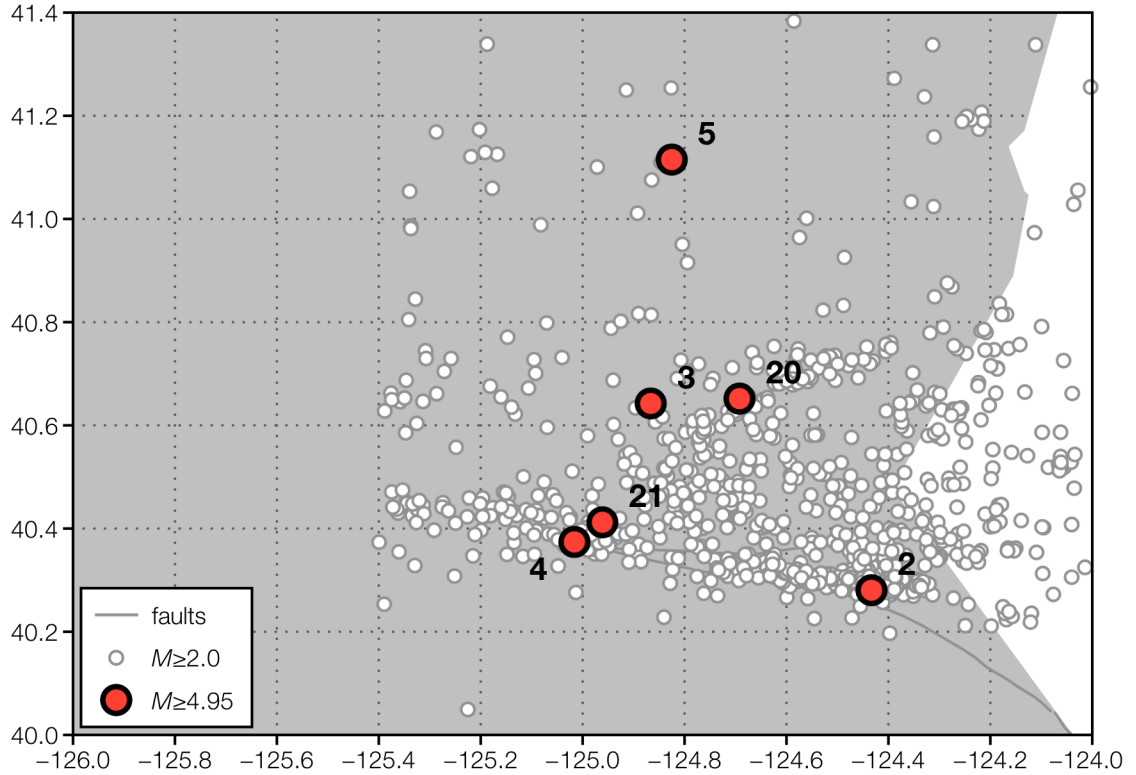


Figure 4.4: Map of the northwest region near Cape Mendocino. Test earthquakes given in Table 4.1 are shown as well as background earthquakes with $M \geq 2.0$.

from 5.0 to 5.45. The pair of earthquakes #17 and #18 are very close in location, magnitude, and time of occurrence. It is very likely that the $M = 5.0$ earthquake on 1 October 2009 was a foreshock of the $M = 5.19$ earthquake on 3 October 2009.

4.4 Submitted Forecasts

The submitted forecasts have been discussed in some detail [114]. The nineteen forecasts submitted by eight groups are available on the RELM website (<http://relm.cseptesting.org/>). In order to have a common basis for comparison, we will only consider forecasts that cover the entire test region. Thirteen forecasts were submitted that gave forecast numbers, N_{emi} , of $M \geq 4.95$ earthquakes in 0.1 magnitude bins during the five year test period for all $N_c = 7682$ $0.1^\circ \times 0.1^\circ$ cells.

The submitted forecasts are based on a variety of approaches. The Bird and Liu forecast [9] was based on a kinematic model of neotectonics. The Ebel et al. forecast [10] was based on the average rate of $M \geq 5$ earthquakes in $3^\circ \times 3^\circ$

cells for the period 1932 to 2004. The Helmstetter et al. forecast [11] was based on the extrapolation of past seismicity. The Wiemer and Schorlemmer forecast [14] was based on the asperity-based likelihood model (ALM). Ward [13] submitted six forecasts. His seismicity submission was based on the extrapolation of past seismicity (Ward seis.), his geologic submission was based on fault slip data (Ward geol.). Two geodetic based simulations were made, one with a maximum magnitude of 8.1 (Ward geod.) and one with a maximum magnitude of 8.5 (Ward geol. 8.5). His simulation submission was based on a fault based simulation of earthquakes in California (Ward sim.). His final submission was an average of the first three submissions (Ward combo).

We will now discuss the Holliday et al. [12] forecast in somewhat greater detail. The basis of this RELM forecast followed the format introduced in the PI forecast methodology [108, 117]. The magnitude range $M \geq 5$ and the cell dimensions $0.1^\circ \times 0.1^\circ$ were the same. However, the PI method was alarm based. Earthquakes were forecast to either occur or not occur in specified regions (hot spots) in a specified time period. In the PI based RELM forecast, all hot spot cells are given equal probabilities of an earthquake. Instead of being alarm based, the RELM test was based on numbers of occurrence of earthquakes in each cell in the test region. This required a continuous assessment of earthquake occurrence rather than a binary, alarm based assessment. To do this, the Holliday et al. [12] forecast introduced a uniform probability of occurrence for hotspot regions and added smaller probabilities for non-hotspot regions based on the RI of seismicity in the region. As a result the distribution of risk in this forecast was very different from the other forecasts. We will quantify this difference in Section 4.6.

As stated in our description of the RELM test, each participant submitted the forecast for the number of earthquakes N_{emi} in magnitude bin m that would occur in cell i . Thus $41 \times 7682 = 314,962$ values of N_{emi} were submitted in each forecast. In this paper we emphasize that there are two aspects to the RELM forecasts:

- (1) How many earthquakes will occur in the test region during the test period?

(2) Where will the forecast earthquakes occur? The number of earthquakes N_e expected is certainly variable but an extrapolation from past seismicity is straight forward. We believe the primary focus of earthquake forecasting is to specify the spatial risk of an earthquake. In this paper we focus our attention on the conditional probability λ_{emi} that a test earthquake will occur in spatial cell i with a magnitude in magnitude bin m .

The submitted forecasts give the number N_{emi} of earthquakes forecast to occur in spatial cell i and in magnitude bin m . The sum of the N_{emi} over all $N_c = 7682$ cells is the total number of earthquakes N_{em} forecast to occur in magnitude bin m during the test period

$$N_{em} = \sum_{i=1}^{N_c} N_{emi}. \quad (4.2)$$

The total number of earthquakes N_e forecast to occur during the test period is given by

$$N_e = \sum_{m=5}^9 N_{em}. \quad (4.3)$$

The number of earthquakes N_e forecast to occur in magnitude bins during the test period are given in Table 4.2. The discussion of these values and their relation to the actual number of test earthquakes that occurred $N = 31$ will be given in the next section.

The forecast conditional probability λ_{emi} that a test earthquake will occur in spatial cell i with a magnitude in magnitude bin m is given by

$$\lambda_{emi} = \frac{N_{emi}}{N_{em}}. \quad (4.4)$$

From Equations 4.2 and 4.4 we see that

$$\sum_{i=1}^{N_c} \lambda_{emi} = 1. \quad (4.5)$$

Table 4.2: Values of the submitted conditional probabilities λ_{emi} that an earthquake that has a magnitude in magnitude bin m will occur in spatial cell i . Values are given for the 31 test earthquakes listed in Table 4.1. The first column is the magnitude bin m , the second column is the spatial cell i , and the third column is the earthquake number. Forecast conditional probabilities λ_{emi} are given for 13 forecasts. These are Bird and Liu [9] (B-L), Ebel et al. [10] main shocks+aftershocks (Ebel) and main shock only (Ebel ms), Helmstetter et al. [11] main shocks+aftershocks (Helm) and main shock only (Helm ms), Holliday et al. [12] (Holl), Ward [13] seismic model with $M_{max} = 8.1$ (Ward seis.), Ward geologic model with $M_{max} = 8.1$ (Ward geol.), Ward geodetic model with $M_{max} = 8.1$ (Ward geod.), Ward combined model with $M_{max} = 8.1$ (Ward combo), Ward geodetic model with $M_{max} = 8.5$ (Ward geod. 8.5), Ward simulation model (Ward sim.), Wiemer and Schorlemmer [14] (W-S). The highest (best) forecast probabilities are in bold. The number of winning forecasts and the mean forecast probabilities for all test earthquakes $\bar{\lambda}_{emi}$ are given for each forecast. Also given are the total number of earthquakes forecast N_e .

m	i	No.	B-L	Ebel	Ebel ms	Helm	Helm ms	Holl	Ward seis.	Ward geol.	Ward geod.	Ward combo	Ward geod. 8.5	Ward sim.	W-S
5	E	5	3.29e-04	4.99e-05	4.99e-05	1.04e-04	1.04e-04	4.42e-06	5.41e-14	2.94e-11	7.24e-05	4.20e-05	7.24e-05	1.16e-29	7.09e-09
5	B	2	6.45e-04	1.55e-03	1.55e-03	3.27e-03	3.27e-03	1.51e-03	6.93e-11	2.94e-11	8.44e-05	4.90e-05	8.44e-05	1.16e-29	2.49e-03
5	H	11	1.58e-05	2.49e-04	2.49e-04	4.16e-05	4.16e-05	7.36e-06	1.12e-07	3.29e-19	2.95e-05	1.72e-05	2.95e-05	1.16e-29	1.22e-05
5	M	17	7.73e-05	9.98e-05	9.98e-05	2.63e-04	2.63e-04	1.51e-03	1.54e-04	1.00e-04	2.10e-04	1.76e-04	2.10e-04	2.82e-06	3.39e-05
5	S	27	9.77e-04	2.49e-04	2.49e-04	5.74e-04	5.74e-04	1.51e-03	6.32e-04	4.17e-04	3.61e-04	4.34e-04	3.61e-04	1.11e-03	6.44e-04
5	K	14	1.43e-03	9.98e-04	9.98e-04	1.50e-03	1.50e-03	1.51e-03	1.49e-03	1.19e-03	5.32e-04	8.76e-04	5.32e-04	3.06e-04	2.80e-03
5	G	9.10	4.19e-04	2.49e-04	2.49e-04	1.16e-03	1.16e-03	1.51e-03	1.86e-03	1.37e-03	5.78e-04	1.02e-03	5.78e-04	5.13e-04	1.23e-03
5	V	31	3.09e-04	6.99e-04	6.99e-04	2.52e-04	2.52e-04	1.51e-03	8.89e-04	6.23e-04	6.49e-04	6.99e-04	6.49e-04	3.41e-05	1.18e-04
5.1	L	15	9.54e-05	2.49e-04	2.49e-04	3.15e-04	3.15e-04	1.51e-04	2.51e-04	8.76e-05	2.48e-04	2.18e-04	2.48e-04	7.76e-06	1.49e-04
5.1	A	7.8,16	9.03e-04	9.98e-04	9.98e-04	5.30e-03	5.30e-03	1.51e-03	1.14e-03	1.31e-03	5.82e-04	8.50e-04	5.82e-04	8.99e-05	5.92e-03
5.2	D	4	1.60e-03	1.50e-03	1.50e-03	3.17e-03	3.17e-03	1.51e-03	4.82e-12	4.45e-11	7.43e-05	4.32e-05	7.43e-05	1.02e-29	1.77e-03
5.2	M	18	7.82e-05	9.98e-05	9.98e-05	2.63e-04	2.63e-04	1.51e-03	1.54e-04	1.00e-04	2.10e-04	1.76e-04	2.10e-04	3.95e-05	2.89e-05
5.3	Q	28	1.31e-03	9.98e-04	9.98e-04	1.29e-03	1.29e-03	1.51e-03	9.25e-04	1.05e-03	5.91e-04	7.55e-04	5.91e-04	7.89e-05	2.40e-03
5.3	R	26	1.40e-03	6.99e-04	6.99e-04	6.52e-04	6.52e-04	7.85e-06	1.25e-03	8.27e-04	6.27e-04	8.08e-04	6.27e-04	1.85e-05	7.26e-04
5.4	C	3	3.34e-04	2.99e-04	2.99e-04	3.37e-04	3.37e-04	1.51e-03	1.61e-12	6.74e-11	6.99e-05	4.06e-05	6.99e-05	5.69e-30	3.65e-04
5.4	I	12	9.72e-05	4.99e-05	4.99e-05	1.66e-04	1.66e-04	9.33e-06	2.29e-11	6.74e-11	8.91e-05	5.18e-05	8.91e-05	5.69e-30	4.56e-04
5.4	F	6	4.26e-04	1.30e-03	1.30e-03	1.40e-03	1.40e-03	1.51e-03	1.13e-04	4.30e-09	3.69e-04	2.41e-04	3.69e-04	8.27e-09	2.11e-03
5.4	J	13	7.64e-05	3.99e-04	3.99e-04	5.06e-04	5.06e-04	1.51e-03	3.63e-04	7.96e-04	2.33e-04	3.69e-04	2.33e-04	1.08e-03	5.30e-04
5.4	U	30	5.72e-04	1.40e-03	1.40e-03	4.68e-03	4.68e-03	1.51e-04	1.25e-03	1.60e-03	2.48e-04	7.34e-04	2.48e-04	5.39e-03	2.41e-03
5.4	Q	25	1.31e-03	9.98e-04	9.98e-04	1.29e-03	1.29e-03	1.51e-03	9.25e-04	1.05e-03	5.91e-04	7.55e-04	5.91e-04	2.26e-04	2.41e-03
5.4	A	1,24	9.06e-04	9.98e-04	9.98e-04	5.30e-03	5.30e-03	1.51e-03	1.14e-03	1.31e-03	5.82e-04	8.50e-04	5.82e-04	4.24e-04	5.78e-03
5.5	R	23	1.39e-03	6.99e-04	6.99e-04	6.52e-04	6.52e-04	7.85e-06	1.25e-03	8.27e-04	6.27e-04	8.08e-04	6.27e-04	5.64e-04	7.33e-04
5.7	T	29	8.25e-04	5.99e-04	5.99e-04	1.11e-03	1.11e-03	1.51e-03	4.72e-04	4.09e-04	1.77e-04	2.89e-04	1.77e-04	9.06e-04	2.32e-03
5.8	N	19	2.62e-03	2.99e-04	2.99e-04	6.78e-04	6.78e-04	1.51e-03	8.94e-04	1.17e-03	5.59e-04	7.52e-04	5.59e-04	3.05e-03	2.81e-04
5.9	P	21	2.97e-04	1.50e-03	1.50e-03	1.23e-03	1.23e-03	1.51e-03	3.87e-12	1.90e-10	7.06e-05	4.10e-05	7.06e-05	1.34e-29	2.73e-04
6.5	O	20	5.64e-04	6.49e-04	6.49e-04	4.30e-04	4.30e-04	1.51e-03	3.23e-12	6.59e-10	7.28e-05	4.23e-05	7.28e-05	3.52e-29	7.30e-04
7.2	Q	22	1.27e-03	9.98e-04	9.98e-04	1.29e-03	1.29e-03	1.51e-03	9.25e-04	1.05e-03	5.91e-04	7.55e-04	5.91e-04	3.12e-04	2.12e-03
number of wins		3		1		3		8	1	0	0	0	0	2	9
$\bar{\lambda}_{emi}$		7.51e-04		6.99e-04		1.38e-03		1.13e-03	5.95e-04	5.67e-04	3.38e-04	4.41e-04	3.38e-04	5.24e-04	1.44e-03
N_e (= 31.00 actual)		55.90		114.75		28.19		35.40	21.13	30.00	22.20	18.13	55.91	32.08	32.20
														8.20	23.71

For all submitted forecasts the sum of the conditional probabilities over all cells is one. Thus the forecasts differ only in the allocation of the conditional probability between the $N_c = 7682$ spatial cells. This allocation will be discussed in some detail in Section 4.6.

The forecast conditional probabilities λ_{emi} for the spatial cells in which test earthquakes occurred are given in Table 4.2. For each of the 31 earthquakes (identified by number in Table 4.1) the appropriate cell i and magnitude bin m are given. The lettering of i for cells has been illustrated in Figure 4.3. Note that earthquakes 9 and 10 occurred in magnitude bin $m = 5$ and cell $i = G$, earthquakes 7, 8 and 16 occurred in magnitude bin $m = 5.1$ and cell $i = A$. Thus we consider 27 cells i and magnitude bins m which we refer to as mi cells. Ebel et al. [10] and Helmstetter et al. [11] submitted separate forecasts for all earthquakes and for only main shocks. From Table 4.2 we see that the forecast numbers N_{em} are substantially higher when aftershocks are considered. However, from Table 4.2 we see that the conditional probabilities λ_{emi} are identical with and without aftershocks. Because of our rescaling approach, we eliminate the difference between these two types of forecasts in terms of forecast locations.

It would be desirable to identify whether the single forecasts were for all earthquakes or for only main shocks. Unfortunately the submissions were ambiguous on this subject. Based on the equality of the values of λ_{emi} for the Ebel et al. [10] and Helmstetter et al. [11] forecasts we will hypothesize that the results for the other forecasts are not significantly dependent on whether they were for all earthquakes or for main shocks only.

4.5 Evaluation of Results

During the formulation of the RELM project a comprehensive testing strategy was also developed [94]. A suite of likelihood tests were proposed which would be implemented through a testing center [95]. The approach utilized an L-test, N-test, and R-test. These tests were applied to the raw submitted data. This approach

was applied to the first $2\frac{1}{2}$ years of RELM results by Schorlemmer et al. [118]. Zechar et al. [96] recognized a problem with the original proposed likelihood tests and proposed a modification. We note that in the testing approach given by Schorlemmer et al. [94] it was suggested that the declustering algorithm given by Reasenberg [119] be used to separate aftershocks from main shocks. Unfortunately the single submission forecasts were not clearly defined to include all earthquakes or just main shocks.

The primary purpose of this paper is to present a complementary approach. Our approach has the advantage that the evaluation of the numbers of earthquakes forecast can be separated from the forecast of their locations. A preliminary version of our approach has been given by Lee et al. [97].

We first consider the forecasts of the number of test earthquakes that would occur during the test period given in Table 4.2. The total number of test earthquakes was 31. Based on the discussion given in Section 4.4 we concluded that 9 - 11 earthquakes were aftershocks, which means there were 20 - 23 main shocks. Thus there were 29 - 35% aftershocks and 65 - 71% main shocks. For the two sets of forecasts that distinguished aftershocks, Ebel et al. [10] had 86 (75%) aftershocks and 29 (25%) main shocks and Helmstetter et al. [11] had 14 (40%) aftershocks and 21 (60%) main shocks. The latter values were reasonably close to the actual values. For the single submissions Holliday et al. [12] forecast 30 earthquakes and Wiemer and Schorlemmer [14] forecast 24 earthquakes, both reasonable values. The 55 earthquakes forecast by Bird and Liu [9] was high and Ward [13] had values from 8 to 56 earthquakes for his 6 forecasts.

The probability λ_{emi} is the forecast conditional probability that a test earthquake will occur in spatial cell i and magnitude bin m . These probabilities, given in Table 4.2, can be used to compare the spatial aspect of RELM forecasts. We first discuss two aspects of the forecast values of λ_{emi} :

1. Values of λ_{emi} have been given for both main shock and main shock plus aftershock forecasts by Ebel et al. [10] and Helmstetter et al. [11]. In both

cases the values of λ_{emi} are identical with and without aftershocks. Thus 13 submitted forecasts are reduced to 11 when considering forecast locations.

2. It is of interest to compare the forecast probabilities for two earthquakes that occur in a cell with different magnitudes. As a specific example we consider two earthquakes that occurred in cell Q, # 22 with $m = 7.2$ and # 28 with $m = 5.3$. For seven of the 11 forecasts the values of λ_{emi} are identical. The others have relatively close values. By normalizing the conditional probabilities with the number of earthquakes N_{em} in magnitude bin m we have isolated the frequency-magnitude (b value) statistics.

We now address the question, which forecast is best at specifying the location of future earthquakes. As a specific example, we consider the $M = 7.2$ El Mayor-Cucapah earthquake (event # 22). The 13 submitted values of λ_{emi} are given in Table 4.2. They range from $\lambda_{emi} = 2.12 \times 10^{-3}$ for the Wiemer and Schorlemmer [14] forecast to $\lambda_{emi} = 3.12 \times 10^{-4}$ for the Ward [13] simulation forecast. The Wiemer and Schorlemmer [14] forecast was the best forecast in that it gave the highest probability of occurrence in this spatial cell and magnitude bin. Using this criteria the “best” forecasts are highlighted in bold in Table 4.2.

There were three spatial-magnitude bins that had multiple earthquakes. These were G-5 with two (earthquakes 9 and 10), A-5.1 with three (earthquakes 7, 8, and 16) and A-5.4 with two (earthquakes 1 and 24). Earthquakes occurred in 27 spatial-magnitude bins. Wiemer and Schorlemmer [14] forecast the largest λ_{emi} for 9 bins, Holliday et al. [12] for 8 bins, Helmstetter et al. [11] and Bird and Liu [9] for 3 bins, Ward [13] simulation model 2 bins, Ward [13] seismic model 1 bin, and Ebel et al. [10] 1 bin.

There are other ways to evaluate the results of the forecasts. One forecast might do very well (high λ_{emi}) for some test earthquakes and do poorly (low λ_{emi}) for other test earthquakes. The overall validity of a forecast can be quantified using the mean forecast probability $\bar{\lambda}_{emi}$ for the 27 spatial-magnitude bins. These values are also given in Table 4.2. The best overall forecast by this measure was

Wiemer and Schorlemmer [14] with $\bar{\lambda}_{emi} = 1.44 \times 10^{-3}$ and Helmstetter et al. [11] with $\bar{\lambda}_{emi} = 1.38 \times 10^{-3}$. It is also of interest to compare the submitted forecasts to a random forecast. Consider an earthquake in magnitude bin m , the sum of all conditional probabilities λ_{emi} is unity as given by Equation 4.5. A random forecast would give equal probabilities to all cells λ_{emi}^{rand} . From Equation 4.5 this value is given by

$$\lambda_{emi}^{rand} = \frac{1}{N_c} = \frac{1}{7682} = 1.30 \times 10^{-4}. \quad (4.6)$$

The best mean forecasts exceed this value by about a factor of 50. All the winning forecasts given in Table 4.2 exceed this random forecast.

4.6 Distribution of Cell Probabilities

The basic purpose of this paper is to better understand the physics and statistics of earthquake forecasts. We have concentrated our discussion on the relative probabilities of where earthquakes will occur. In order to do this we have introduced the conditional probability λ_{emi} that an earthquake in magnitude bin m will lie in spatial cell i . The sum of λ_{emi} over all bins i is unity. Thus the allocation of conditional probabilities λ_{emi} between cells is the essential feature of a successful forecast. To explore this we will consider the forecast probability λ_{ei} that an earthquake with magnitude $m \geq 4.95$ will occur in cell i . The definition of this probability is

$$\lambda_{ei} = \frac{\sum_m N_{emi}}{\sum_i \sum_m N_{emi}}. \quad (4.7)$$

Once again we have

$$\sum_i \lambda_{ei} = 1. \quad (4.8)$$

The values of the probability λ_{ei} are similar to the values of the conditional probability λ_{emi} , but the sum over magnitude bins eliminates the weak dependence of λ_{emi} on m due to different values of the b-value used in the forecasts. We rank

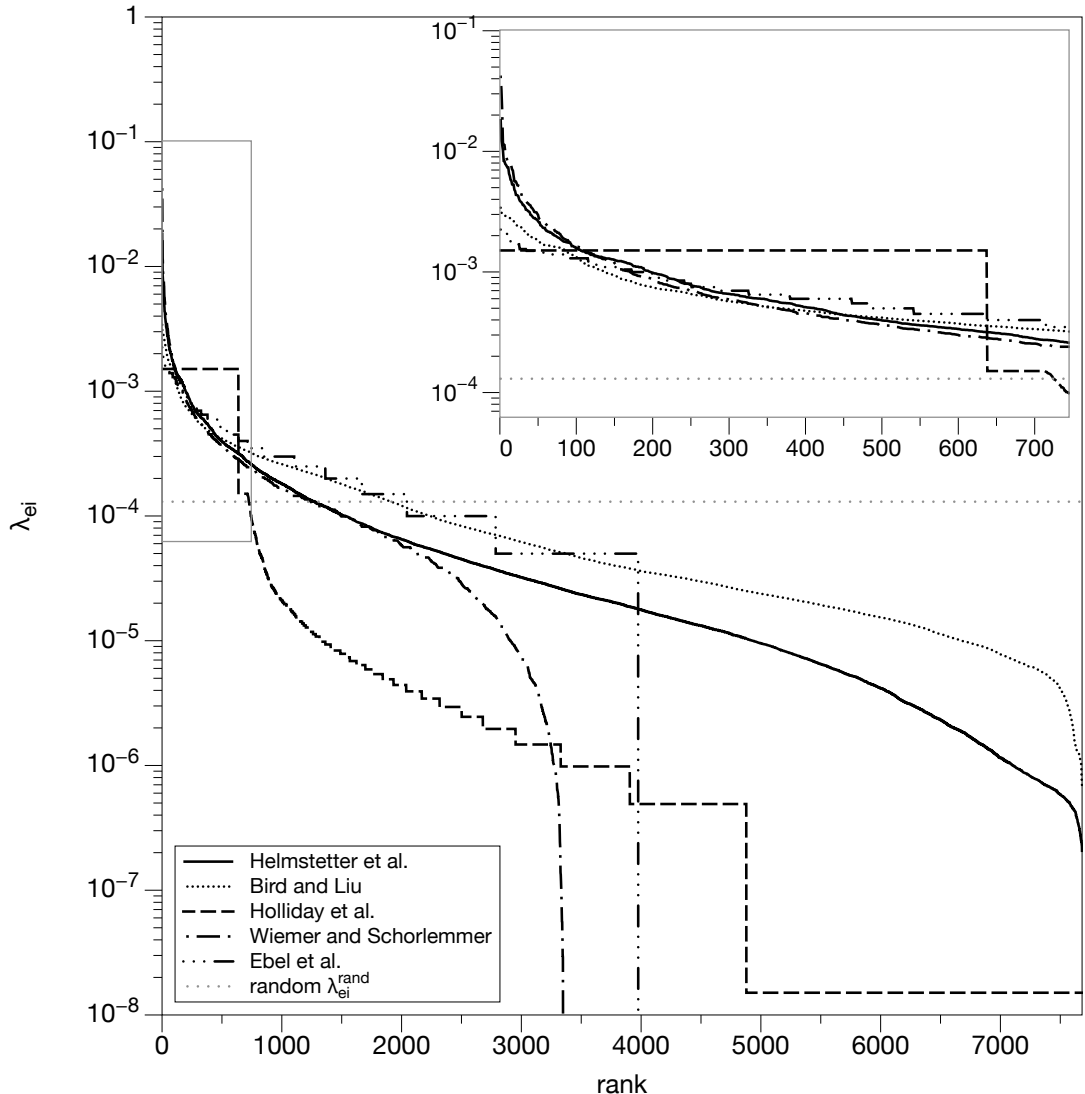


Figure 4.5: Distribution of forecast probabilities λ_{ei} that an earthquake with $m \geq 4.95$ will occur in cell i . The 7682 forecast cell probabilities are ranked from highest to lowest. In each forecast the sum of the probabilities is unity. The no skill forecast λ_{emi}^{rand} is also included.

these probabilities λ_{ei} in a forecast from the highest to the lowest. The highest forecast probability is N_1 and the lowest forecast probability is N_{7682} .

In Figure 4.5 we give the distribution of forecast probabilities λ_{ei} for the forecasts of Bird and Liu [9], Ebel et al. [10], Helmstetter et al. [11], Holliday et al. [12], and Wiemer and Schorlemmer [14] are given in Figure 4.5. The areas under the curves are equal to 1. For the highest probabilities $0 < N_c < 100$ the forecasts of

Helmstetter et al. and Wiemer and Schorlemmer forecast the highest probabilities λ_{in} , however the forecasts of Wiemer and Schorlemmer are slightly higher because they gave reduced probabilities for large N_c . In the range of $100 < N_c < 637$ the forecast by Holliday et al. gave the highest probabilities of occurrence. This behavior can be attributed to the alarm basis of the PI forecast. The highest probability cells, $0 < N_c < 637$ were given the same probability values. For the range $637 < N_c < 7682$ the forecast probabilities were much lower. In the range $637 < N_c < 4000$ the forecast probabilities given by Bird and Liu and Ebel et al. were the highest and were approximately equal. For the range $400 < N_c < 7682$ the forecast probabilities given by Bird and Liu were the highest. The forecast by Wiemer and Schorlemmer gave the largest range of values and the forecast by Bird and Liu gave the smallest range of values. If a range of low probabilities are given in order to enhance the values of the highest probabilities the risk is that an unexpected earthquake will occur in the cells with a low forecast probability. An example is the forecast (Table 4.2) $\lambda_{emi} = 7 \times 10^{-9}$ given by Wiemer and Schorlemmer [14] for test earthquake # 1. The highest forecast for this earthquake was $\lambda_{emi} = 7.29 \times 10^{-4}$ by Bird and Liu [9].

A no skill forecast would assign a probability $\lambda_{emi}^{rand} = 7.29 \times 10^{-4}$ to all cells (Equation 4.6). Out of the 7682 cells the Helmstetter et al. [11] and the Wiemer and Schorlemmer [14] forecasts had 1400 cells with higher than no skill probabilities, Bird and Liu [9] had 1900 and Ebel et al. [10] 2100.

As we have previously discussed earthquake forecasts can be either probabilistic or alarm based. The submission rules for RELM were probabilistic. The only forecast that had an alarm based distribution of forecasts was Holliday et al. [12]. In the probabilities λ_{emi} listed in Table 4.2, the “hot spot” (alarm) cells had values $\lambda_{emi} = 1.15 \times 10^{-3}$. Of the 27 cells in which earthquakes occurred, 20 occurred in hot spot cells. In 8 of the 20 cells, the hot spot forecasts had the highest probabilities of occurrence. The hot spot cells comprised 8.3% of the test region (637 of the 7682 cells). This alarm based behavior is clearly illustrated in Figure

4.5.

4.7 Discussion

The RELM test provided a well defined set of prospective earthquake forecasts and a well defined set of test earthquakes. In this chapter we present a method for evaluating the RELM forecasts. We believe our approach has significant advantages but look forward to comparing our results with those obtained by other authors.

RELM forecasts provide the numbers N_{emi} of earthquakes expected to occur in magnitude bins m and spatial cells i . The basis of our approach is:

1. To use Equation 4.2 to determine the forecast number N_{em} of earthquakes expected to occur in magnitude bin m .
2. To use Equation 4.4 to determine the conditional probability λ_{emi} that an earthquake with magnitude in magnitude bin m will occur in cell i . In addition Equation 4.4 is used to determine the total number N_e of forecast earthquakes.

The conditional probability λ_{emi} is the forecast probability that an earthquake with magnitude m will occur in cell i . The sum of the λ_{emi} over all cells is unity. The allocation of the λ_{emi} to cells is the forecast of where earthquakes are expected to occur. When separate forecasts were submitted for all earthquakes and for only main shocks the values of λ_{emi} were identical. In addition the values of λ_{emi} were either independent of m or only weakly dependent on m .

A random (no skill) forecast would have assigned equal values of λ_{emi} to all cells. The success (skill) of a forecast is measured by the forecasters ability to assign large values of λ_{emi} to the cells where test earthquakes occurred and small values where they did not occur.

During the test period 31 earthquakes occurred with $M > 4.95$. These earthquakes occurred in 27 different combinations of spatial cell i and magnitude bin

m as shown in Table 4.2. The largest forecast values of λ_{emi} for each of these 27 values of m and i were the best forecasts, these are highlighted in Table 4.2. The largest values ranged from $\lambda_{emi} = 5.92 \times 10^{-3}$ for earthquakes 7, 8 and 16 in magnitude bin $m = 5.1$ and in cell A to $\lambda_{emi} = 2.49 \times 10^{-4}$ for earthquake 11 in magnitude bin $m = 5$ and cell H. All the largest values exceeded the random (no skill) value $\lambda_{emi}^{rand} = 1.30 \times 10^{-4}$ given in Equation 4.6. One measure of the “best” forecast is the forecast with the largest number of highest λ_{emi} . From Table 4.2 the winner by this measure is the Wiemer and Schorlemmer [14] forecast with 9 highest values followed by Holliday et al. [12] with 8 highest values. An alternative measure of the “best” forecast is the highest mean value of λ_{emi} for the 27 values of m and i . The values of $\bar{\lambda}_{emi}$ for the forecasts are given in Table 4.2. The winner by this measure is again the forecast by Wiemer and Schorlemmer [14] with $\bar{\lambda}_{emi} = 1.44 \times 10^{-3}$ followed by Helmstetter et al. [11] with $\bar{\lambda}_{emi} = 1.38 \times 10^{-3}$. These values are about one order of magnitude better than the random (no skill) value $\lambda_{emi}^{rand} = 1.30 \times 10^{-4}$.

The success of a RELM forecast is dependent on the allocation of the probabilities λ_{emi} between the 7682 cells. In Figure 4.5 we give the distribution of forecast probabilities λ_{ei} for five forecasts. The variability is clearly illustrated. It is interesting to compare the forecast by Wiemer and Schorlemmer [14] to the forecast by Helmstetter et al. [11]. Wiemer and Schorlemmer [14] had slightly higher values of λ_{ei} in the high probability regions. This is the reason that Wiemer and Schorlemmer [14] had the best forecasts for earthquakes 1, 6, 7, 8, 14, 16, 22, 24, 25 and 29. In order to have these higher values of λ_{ei} , Wiemer and Schorlemmer [14] had very low values of λ_{ei} in low probability regions. The consequence of the balance was the very poor forecast ($\lambda_{ei} = 7.09 \times 10^{-9}$) for earthquake number 5. It is a matter of choice how this poor forecast should be penalized.

The forecast by Holliday et al. [12] differed from the other forecasts since it was alarm based. This is clearly seen in Figure 4.5 where the 637 high probability cells had equal forecast probabilities, $\lambda_{ei} = 1.51 \times 10^{-3}$. The consequence was

that this forecast was not highest in high probability regions but was the highest in moderate probability regions. Thus this forecast had the highest probabilities ($\lambda_{ei} = 1.51 \times 10^{-3}$) for earthquakes 3, 13, 17, 18, 20, 21, 27 and 31. Overall 23 of the 31 earthquakes occurred in hot spot regions that included 637 out of 7682 (8.3%) of the cells. However, the Holliday et al. [12] forecast had very low forecast probabilities ($2 - 9 \times 10^{-6}$) for four of the earthquakes.

4.8 Conclusion

In summary we conclude that the RELM test was extremely useful in providing an understanding of the trade offs in forecasting the locations of future earthquakes. The RELM forecasts were primarily based on the extrapolation of the rates of earthquake activity to forecast where future earthquakes occur. The results quantified the statistical validity of this approach. It should be noted that there were two important limitations to the RELM test approach. The first is that prospective test earthquakes have considerable statistical variability. The RELM test earthquakes were dominated by events associated with the $M = 7.2$ El Mayor-Cucapah earthquake. The second is the relevance of the test earthquakes to the occurrence of larger earthquakes. The minimum magnitude earthquake in the RELM test was $M = 4.95$. From Table 4.1 we see that 29 of the 31 earthquakes have magnitudes $M < 6$. This activity certainly correlated quite well with pre-existing background seismicity. Earthquakes with $M > 7.0$ are likely to occur on mapped faults. Many of these faults (i.e. the San Andreas) have low levels of seismicity on them. The implications of this low level of seismicity are not clear.

4.9 Glossary

M earthquake magnitude

m bin magnitude $m - 0.05 \leq M \leq m + 0.05$

N_e number of forecast earthquakes

N number of actual earthquakes

N_{em} number of earthquakes in magnitude min m

N_{emi} number of earthquakes in magnitude bin m and cell i

λ_{emi} probability that an earthquake will occur in magnitude bin m and cell i

λ_{ei} probability that an earthquake with $M \geq 4.95$ will occur in cell i

REFERENCES

- [1] B. D. Malamud, G. Morein, and D. L. Turcotte. Forest fires: An example of self-organized critical behavior,. *Science*, 281:1840–1842, 1998.
- [2] T. J. Brown, B. L. Hall, C. R. Mohrle, and H. J. Reinbold. 2002: Coarse assessment of federal wildland fire occurrence data, report for the national wildfire coordinating group. *CEFA Report 02-04*, 2002.
- [3] Bruce D. Malamud, Donald L. Turcotte, Fausto Guzzetti, and Paola Reichenbach. Landslide inventories and their statistical properties. *Earth Surface Processes and Landforms*, 29(6):687, 2004.
- [4] Bruce D. Malamud and Donald L. Turcotte. The applicability of power-law frequency statistics to floods. *Journal of Hydrology*, 322(1-4):168 – 180, 2006. ISSN 0022-1694. doi: DOI:10.1016/j.jhydrol.2005.02.032. Hydrofractals '03.
- [5] J. E. O'Connor, L. L. Ely, W. E. Wohl, L. E. Stevens, T. S. Melis, V. S. Kale, and V. R. Baker. A 4500-year record of large floods on the colorado river in the grand canyon, arizona. *Journal of Geology*, 102:1–9, 1994.
- [6] E. H. Field, T. E. Dawson, K. R. Felzer, A. D. Frankel, V. Gupta, T. H. Jordan, T. Parsons, M. D. Petersen, R. S. Stein, R. J. Weldon II, and C. J. Wills. The uniform california earthquake rupture forecast, version 2 (ucerf 2). Technical report, Southern California Earthquake Center, <http://pubs.usgs.gov/of/2007/1437/>, 2007.
- [7] D. L. Wells and K. J. Coppersmith. New empirical relationships among magnitude, rupture length, rupture width, rupture area, and surface displacement. *Bull. Seis. Soc. Am.*, 84(4):974–1002,, 1994.
- [8] H. Kanamori and D. L. Anderson. Theoretical basis of some emperical relations in seismology. *Bull. Seis. Soc. Am.*, 65(5):1073–1095, October 1975.
- [9] P. Bird and Z. Liu. Seismic hazard inferred from tectonics: California. *Seis. Res. Lett.*, 78:37–48, 2007.
- [10] J. E. Ebel, D. W. Chambers, A. L. Kafka, and J. A. Baglivo. Non-poissonian earthquake clustering and the hidden Markov model as bases for earthquake forecasting in California. *Seis. Res. Lett.*, 78:57–65, 2007.
- [11] A. Helmstetter, Y. Y. Kagan, and D. D. Jackson. High-resolution time-independent grid-based forecast for $m \geq 5$ earthquakes in California. *Seis. Res. Lett.*, 78:78–86, 2007.

- [12] J. R. Holliday, C. C. Chen, K. F. Tiampo, J. B. Rundle, D. L. Turcotte, and A. Donnellan. A RELM earthquake forecast based on pattern informatics. *Seis. Res. Lett.*, 78(1):87–93, 2007.
- [13] S. N. Ward. Methods for evaluating earthquake potential and likelihood in and around California. *Seis. Res. Lett.*, 78(1):87–93, 2007.
- [14] S. Wiemer and D. Schorlemmer. ALM: An asperity-based likelihood model for California. *Seismol. Res. Letts.*, 78(1):134–140, 2007.
- [15] M. Able, N. Kemper, and T. Rosenthal. Review of natural catastrophes in 2011: Earthquakes result in record loss. http://www.munichre.com/en/media_relations/press_releases/2012/2012_01_04_press_release.aspx, January 2012.
- [16] U.S. Geological Survey. Earthquake facts and statistics. <http://earthquake.usgs.gov/earthquakes/eqarchives/year/eqstats.php>, June 2012.
- [17] B. Ehrhart, S. Mildenhall, K. Campion, S. Jakubowski, A. Podlaha, and S. Bowen. Annual global climate and catastrophe report. http://thoughtleadership.aonbenfield.com/Documents/20120110_if_annual_global_climate_cat_report.pdf, January 2012.
- [18] U.S. Geological Survey. Earthquakes with 1,000 or more deaths since 1900. http://earthquake.usgs.gov/earthquakes/world/world_deaths.php, June 2012.
- [19] The Economist online. Counting the cost. http://www.economist.com/blogs/dailychart/2011/03/natural_disasters, March 2011.
- [20] World Bank. Haiti earthquake pdna: Assessment of damage, losses, general and sectoral needs. http://siteresources.worldbank.org/INTLAC/Resources/PDNA_Haiti\discretionary{-}{}{}2010_Working_Document_EN.pdf, 2010.
- [21] R. Chen, D. Branum, and C. J. Wills. California geological survey - 2009 earthquake loss estimation. http://www.conservation.ca.gov/cgs/rghm/loss/Pages/2009_analysis.aspx, June 2009.
- [22] C. Covey, S. L. Thompson, P. R. Weissman, and M. C. MacCracken. Global climatic effects of atmospheric dust from an asteroid or comet impact on earth. *Global and Planetary Change*, 9:263 – 273, 1994. ISSN 0921-8181. doi: 10.1016/0921-8181(94)90020-5.
- [23] CBS News. Earth's day length shortened by japan earthquake. <http://www.cbsnews.com/stories/2011/03/13/scitech/main20042590.shtml>, March 2011.

- [24] N. Metropolis, A.W. Rosenbluth, M.N. Rosenbluth, A.H. Teller, and E. Teller. Equations of state calculations by fast computing machines. *Journal of Chemical Physics*, 21(6):1087–1092, 1953.
- [25] G. Yakovlev, D. L. Turcotte, J. B. Rundle, and P. B. Rundle. Simulation-based distributions of earthquake recurrence times on the San Andreas fault system. *Bull. Seis. Soc. Am.*, 96:1995–2007, 2006.
- [26] M. B. Yikilmaz, D. L. Turcotte, G. Yakovlev, J. B. Rundle, and L. H. Kellogg. Virtual california earthquake simulations: simple models and their application to an observed sequence of earthquakes. *Geophys. J. Int.*, 180:734–742, 2010.
- [27] M. B. Yikilmaz, E. M. Heien, D. L. Turcotte, J. B. Rundle, and L. H. Kellogg. A fault and seismicity based composite simulation in northern california. *Nonlinear Processes in Geophysics*, 18(6):955–966, 2011. doi: 10.5194/npg-18-955-2011. URL <http://www.nonlin-processes-geophys.net/18/955/2011/>.
- [28] J. B. Rundle, J. R. Holliday, M. Yoder, M. K. Sachs, A. Donnellan, D. L. Turcotte, K. F. Tiampo, W. Klein, and L. H. Kellogg. Earthquake precursors: activation or quiescence? *Geophysical Journal International*, 187(1):225–236, October 2011.
- [29] Per Bak, Chao Tang, and Kurt Wiesenfeld. Self-organized criticality. *Phys. Rev. A*, 38(1):364–374, Jul 1988. doi: 10.1103/PhysRevA.38.364.
- [30] Bruce D. Malamud, James D. A. Millington, and George L. W. Perry. Characterizing Wildfire Regimes in the United States. *Proceedings of the National Academy of Sciences of the United States of America*, 102(13):4694–4699, 2005. doi: 10.1073/pnas.0500880102.
- [31] B. D. Malamud, G. Morein, and D. L. Turcotte. Log-periodic behavior in a forest-fire model. *Nonlinear Processes in Geophysics*, 12(5):575–585, 2005. doi: 10.5194/npg-12-575-2005.
- [32] Benoit B Mandelbrot. *The fractal geometry of nature*. W.H. Freeman, New York, updated and augm edition, 1983.
- [33] M. K. Sachs, M. R. Yoder, D. L. Turcotte, J. B. Rundle, and B. D. Malamud. Black swans, power laws, and dragon-kings: Earthquakes, volcanic eruptions, landslides, wildfires, floods, and SOC models. *Eur. Phys. J. Special Topics*, 205:167–182, 2012.
- [34] M. K. Sachs, J. B. Rundle, J. R. Holliday, J. Gran, M. Yoder, and W. Graves. *Self-Organized Criticality Systems*, chapter 9. Self-Organizing Complex Earthquakes: Scaling in Data, Models, and Forecasting. Open Academic Press, 2013.

- [35] R. R Kinnison. *Applied Extreme Value Statistics*. Battelle Press, Columbus, Ohio, 1985. ISBN 0029476305.
- [36] Nassim Taleb. *The Black Swan: The Impact of the Highly Improbable*. Random House, New York, 1st ed edition, 2007. ISBN 9781400063512.
- [37] Donald Lawson Turcotte. *Fractals and Chaos in Geology and Geophysics*. Cambridge University Press, Cambridge, U.K., 2nd ed edition, 1997. ISBN 0521561647 (hardback).
- [38] D. Sornette. Dragon-kings, black swans and the prediction of crises. *International Journal of Terraspace Science and Engineering*, 2:1, 2009.
- [39] A. Guarino, A. Garcimartín, and S. Ciliberto. An experimental test of the critical behaviour of fracture precursors. *The European Physical Journal B - Condensed Matter and Complex Systems*, 6:13–24, 1998. ISSN 1434-6028. 10.1007/s100510050521.
- [40] M. Alava, P. Nukala, and S. Zapperi. Statistical models of fracture. *Advances in Physics*, 55(3):349 – 476, 2006.
- [41] J. M. Carlson and J. S. Langer. Mechanical model of an earthquake fault. *Phys. Rev. A*, 40(11):6470–6484, Dec 1989. doi: 10.1103/PhysRevA.40.6470.
- [42] R. Burridge and L. Knopoff. Model and theoretical seismicity. *Bull. Seism. Soc. Am.*, 57(3):341–371, June 1967.
- [43] S. Abaimov, D. Turcotte, R. Shcherbakov, J. Rundle, G. Yakovlev, C. Goltz, and W. Newman. Earthquakes: Recurrence and interoccurrence times. *Pure and Applied Geophysics*, 165:777–795, 2008. ISSN 0033-4553. 10.1007/s00024-008-0331-y.
- [44] D. Sornette. Les phénomènes critiques auto-organisés. *Images de la Physique 1993*, édition du CNRS:9–14, (CNRS, Paris,1994).
- [45] D. Sornette, P. Miltenberger, and C. Vanneste. Statistical physics of fault patterns self-organized by repeated earthquakes: synchronization versus self-organized criticality. In P. Bouwknegt, P. Fendley, J. A. Minahan, D. Nemeschansky, K. Pilch, H. Saleur, and N. P. Warner, editors, *Recent progress in statistical mechanics and quantum field theory. Proceedings, Conference, Los Angeles, USA, May 16-21, 1994.*, pages 313–332, Singapore, 1995. World Scientific.
- [46] I. Osorio, M. G. Frei, D. Sornette, J. Milton, and Y. C. Lai. Epileptic seizures, quakes of the brain? *Phys. Rev. E*, 82(2):021919, 2010.
- [47] B. Drossel and F. Schwabl. Self-organized critical forest-fire model. *Phys. Rev. Lett.*, 69(11):1629–1632, Sep 1992. doi: 10.1103/PhysRevLett.69.1629.

- [48] S. F. Tebbens and S. M. Burroughs. Forest fire burn areas in Western Canada modeled as self-similar criticality. *Physica D*, 211:221–234, 2005.
- [49] B. Gutenberg and C. F. Richter. *Seismicity of the Earth and Associated Phenomena*. Princeton University Press, Princeton, NJ, 1954.
- [50] A. M. Dziewoński, T. A. Chou, and J. W. Woodhouse. Determination of earthquake source parameters from waveform data for studies of global and regional seismicity. *J. Geophys. Res.*, 86(B4):2825–2852, 1981.
- [51] G. Ekström, A. M. Dziewoński, N. N. Maternovskaya, and M. Nettles. Global seismicity of 2003: centroid-moment-tensor solutions for 1087 earthquakes. *Phys. Earth Planet. Inter.*, 148:327–351, 2005.
- [52] E. R. Engdahl, R. van der Hilst, and R. Buland. Global teleseismic earthquake relocation with improved travel times and procedures for depth determination. *Bull. Seis. Soc. Am.*, 88(3):722–743, 1998.
- [53] J. B. Rundle. Derivation of the complete gutenbergrichter magnitude-frequency relation using the principle of scale invariance. *J. Geophys. Res.*, 94 (B9):12337–12342, 1989.
- [54] D. Sornette, L. Knopoff, Y. Kagen, and C. Vanneste. Rankordering statistics of extreme events: Application to the distribution of large earthquakes. *J. Geophys. Res.*, 101(B6):13883–13893, 1996.
- [55] Steven G. Wesnousky. The gutenberg-richter or characteristic earthquake distribution, which is it? *Bull. Seis. Soc. Am.*, 84(6):1940–1959, 1994.
- [56] G. P. Biasi, R. J. Weldon, T. E. Fumal, and G. G. Seitz. Paleoseismic event dating and the conditional probability of large earthquakes on the southern san andreas fault, california. *Bull. Seis. Soc. Am.*, 92(7):2761–2781, 2002.
- [57] M. Ando. Source mechanisms and tectonic significance of historical earthquakes along the nankai trough, japan. *Tectonophys.*, 27:119–140, 1975.
- [58] W. H. Bakun, B. Aagaard, B. Dost, W. L. Ellsworth, J. L. Hardebeck, R. A. Harris, C. Ji, M. J. S. Johnston, J. Langbein, J. J. Lienkaemper, A. J. Michael, J. R. Murray, R. M. Nadeau, P. A. Reasenberg, M. S. Reichle, E. A. Roeloffs, A. Shakal, R. W. Simpson, and F. Waldhauser. Implications for prediction and hazard assessment from the 2004 Parkfield earthquake. *Nature*, 437:969–974, 2005.
- [59] Robert Shcherbakov, Donald L. Turcotte, and John B. Rundle. Scaling properties of the parkfield aftershock sequence. *Bull. Seis. Soc. Am.*, 96 (4B):S376–384, 2006. doi: 10.1785/0120050815.

- [60] Renner B. Hofmann. Individual faults can't produce a gutenberg-richter earthquake recurrence. *Engineering Geology*, 43(1):5 – 9, 1996. ISSN 0013-7952. doi: DOI:10.1016/0013-7952(95)00085-2.
- [61] T. Ishibe and K. Shimazaki. Seismicity in source regions of large interplate earthquakes around japan and the characteristic earthquake model. *Earth Planets and Space*, 61(9):1041 – 1052, 2009.
- [62] Richard B. Stothers. The great tambora eruption in 1815 and its aftermath. *Science*, 224(4654):1191–1198, 1984.
- [63] N. I. Deligne, S. G. Coles, and R. S. J. Sparks. Recurrence rates of large explosive volcanic eruptions. *J. Geophys. Res.*, 115:B06203, 2010.
- [64] C. A. Chesner, W. I. Rose, A. Deino, R. Drake, and J. A. Westgate. Eruptive History of Earth's Largest Quaternary Caldera (Toba, Indonesia) Clarified. *Geology*, 19(3):200–203, 1991. doi: 10.1130/0091-7613(1991)019<0200:EHOESL>2.3.CO;2.
- [65] M. R. Rampino and S. Self. Bottleneck in Human Evolution and the Toba Eruption. *Science*, 262(5142):1955, 1993. doi: 10.1126/science.8266085.
- [66] James D. A. Millington, George L. W. Perry, and Bruce D. Malamud. Models, data and mechanisms: Quantifying wildfire regimes. *Geological Society, London, Special Publications*, 261(1):155–167, 2006. doi: 10.1144/GSL.SP.2006.261.01.12.
- [67] Richard A. Minnich. Fire Mosaics in Southern California and Northern Baja California. *Science*, 219(4590):1287–1294, 1983. doi: 10.1126/science.219.4590.1287.
- [68] Richard A. Minnich. An integrated model of two fire regimes. *Conservation Biology*, 15:1549, 2001.
- [69] C. Philip Weatherspoon and Carl N. Skinner. Landscape-Level Strategies for Forest Fuel Management. Technical report, UC Davis, Centers for Water and Wildland Resources, 1996. Sierra Nevada Ecosystem Project: Final report to Congress, vol. II, Assessments and scientific basis for management options.
- [70] Alan H. Taylor and Carl N. Skinner. Fire history and landscape dynamics in a late-successional reserve, klamath mountains, california usa. *Forest Ecol. Manag.*, 111:285–301, 1998. doi: 10.1016/S0378-1127(98)00342-9.
- [71] James K. Agee and Carl N. Skinner. Basic principles of forest fuel reduction treatments. *Forest Ecol. Manag.*, 211:83–96, 2005. doi: 10.1016/j.foreco.2005.01.034.

- [72] Mark R. Yoder, Donald L. Turcotte, and John B. Rundle. A forest-fire model with natural fire resistance. *Phys. Rev. E*, 83(046118), 2011.
- [73] David R Maidment. *Handbook of Hydrology*. McGraw-Hill, New York, 1993. ISBN 0070397325.
- [74] Bruce D. Malamud, Donald L. Turcotte, and Christopher C. Barton. The 1993 mississippi river flood; a one hundred or a one thousand year event? *Environmental and Engineering Geoscience*, 2(4):479–486, 1996.
- [75] M. K. Sachs, E. M. Heien, D. L. Turcotte, M. B. Yikilmaz, J. B. Rundle, and L. H. Kellogg. Virtual California earthquake simulator. *Seis. Rev. Lett.*, 83(6), November/December 2012.
- [76] T. E. Tullis, K. Richards-Dinger, M. Barall, J. H. Dieterich, E. H. Field, E. M. Heien, L. H. Kellogg, F. Pollitz, J. B. Rundle, M. K. Sachs, D. L. Turcotte, S. N. Ward, and M. B. Yikilmaz. Generic earthquake simulator. *Seis. Rev. Lett.*, 83(6):959–963, November/December 2012.
- [77] T. E. Tullis, K. Richards-Dinger, M. Barall, J. H. Dieterich, E. H. Field, E. M. Heien, L. H. Kellogg, F. Pollitz, J. B. Rundle, M. K. Sachs, D. L. Turcotte, S. N. Ward, and M. B. Yikilmaz. A comparison among observations and earthquake simulator results for the allcal2 california fault model. *Seis. Rev. Lett.*, 83(6):994–1006, November/December 2012.
- [78] P. B. Rundle, J. B. Rundle, K. F. Tiampo, A. Donnellan, and D. L. Turcotte. Virtual California: fault model, frictional parameters, applications. *Pure Ap. Geophys.*, 163:1819–1846, 2006.
- [79] J. B. Rundle. A physical model for earthquakes. 1. fluctuations and interactions. *J. Geophys. Res.*, 93:6237–6254, 1988.
- [80] J. B. Rundle. A physical model for earthquakes. 2. application to southern california. *J. Geophys. Res.*, 93:6255–6274, 1988.
- [81] P. B. Rundle, J. B. Rundle, K. F. Tiampo, J. S. Sá Martins, S. McGinnis, and W. Klein. Nonlinear network dynamics on earthquake fault systems. *Phys. Rev. Lett.*, 87:148501, 2001.
- [82] J. B. Rundle, P. B. Rundle, W. Klein, J. S. Sá Martins, K. F. Tiampo, A. Donnellan, and L. H. Kellogg. Gem plate boundary simulations for the plate boundary observatory: A program for understanding the physics of earthquakes on complex fault networks via observations, theory, and numerical simulation. *Pure Ap. Geophys.*, 159:2357–2381, 2002.
- [83] J. B. Rundle, P. B. Rundle, A. Donnellan, and G. Fox. Gutenberg-Richter statistics in topologically realistic system-level earthquake stress-evolution simulations. *Earth, Planets and Space*, 55(8):761–771, 2004.

- [84] J. B. Rundle, P. B. Rundle, A. Donnellan, P. Li, W. Klein, G. Morein, D. L. Turcotte, and L. Grant. Stress transfer in earthquakes, hazard estimation and ensemble forecasting: Inferences from numerical simulations. *Tectonophys.*, 413:109–125, 2006.
- [85] S. N. Ward. A synthetic seismicity model for southern California: cycles, probabilities, and hazard. *J. Geophys. Res.*, 101(B10):22393–22418, 1996.
- [86] J. Dieterich and K. B. Richards-Dinger. Earthquake recurrence in simulated fault systems. *Pure and Applied Geophysics*, 167:1087–1104, 2010. ISSN 0033-4553. URL <http://dx.doi.org/10.1007/s00024-010-0094-0>. 10.1007/s00024-010-0094-0.
- [87] F. F. Pollitz. Epistemic uncertainty in california-wide synthetic seismicity simulations. *Bulletin of the Seismological Society of America*, 101(5):2481–2498, 2011. doi: 10.1785/0120100303. URL <http://www.bssaonline.org/content/101/5/2481.abstract>.
- [88] J. B. Rundle and D. D. Jackson. Numerical simulation of earthquake sequences. *Bull. Seism. Soc. Am.*, 67(5):1363–1377, Oct. 1977.
- [89] W. Klein, M. Anghel, C. D. Ferguson, J. B. Rundle, and J. S. Sá Martins. Statistical analysis of a model for earthquake faults with long-range stress transfer. volume 120 of *Geophysical Monograph*, pages 43–71. American Geophysical Union, Washington D.C., 2000.
- [90] Y. Okada. Internal deformation due to shear and tensile faults in a half-space. *Bull. Seism. Soc. Am.*, 82:1018–1040, 1992.
- [91] D. L. Turcotte and G. Schubert. *Geodynamics*. Cambridge University Press, second edition, 2002.
- [92] C. H Scholz. *The mechanics of earthquakes and faulting*. Cambridge University Press, Cambridge, UK, 2nd ed edition, 2002. ISBN 0521652235 (hardback). URL <http://www.loc.gov/catdir/samples/cam033/2001043297.html>.
- [93] E. M. Heien and M. K. Sachs. Understanding long term earthquake behavior through simulation. *Computing in Science and Engineering*, 14(5):10, September/October 2012.
- [94] D. Schorlemmer, M. C. Gersterberger, S. Wiemer, D. D. Jackson, and D. A. Rhoades. Earthquake likelihood model testing. *Seismol. Res. Lett.*, 78:17–29, 2007.
- [95] D. Schorlemmer and M. C. Gersterberger. RELM testing center. *Seismol. Res. Lett.*, 78:31–36, 2007.

- [96] J. D. Zechar, M. C. Gersterberger, and D. A. Rhoades. Likelihood-based tests for evaluating space-rate-magnitude earthquake forecasts. *Bull. Seis. Soc. Am.*, 100:1184–1195, 2010.
- [97] Y. T. Lee, D. L. Turcotte, J. R. Holliday, M. K. Sachs, J. B. Rundle, C. C. Chen, and K. F. Tiampo. Results of the regional earthquake likelihood models (RELM) test of earthquake forecasts in California. *Proc. Nat. Acad. Sci. (USA)*, 108(40):16533–16538, 2011. doi: 10.1073/pnas.1113481108.
- [98] M. K. Sachs, Y. T. Lee, D. L. Turcotte, J. R. Holliday, and J. B. Rundle. Evaluating the RELM test results. *Int. J. Geophys.*, 2012(543482), 2012.
- [99] M. K. Sachs, Y. T. Lee, D. L. Turcotte, J. R. Holliday, and J. B. Rundle. Implications of the RELM test of earthquake forecasts in California. *Res. Geophys.*, 2(2):e10, 2012.
- [100] M. K. Sachs, D. L. Turcotte, J. R. Holliday, and J. B. Rundle. Forecasting earthquakes: The RELM test. *Computing in Science and Engineering*, 14(5):43, September/October 2012.
- [101] C. G. Bufe and D. J. Varnes. Predictive modeling of the seismic cycle of the greater San Francisco Bay region. *J. Geophys. Res.*, 98:9871–9883, 1993. doi: 10.1029/93JB00357.
- [102] D. D. Bowman, G. Ouillon, C. G. Sammis, A. Sornette, and D. Sornette. An observational test of the critical earthquake concept. *J. Geophys. Res.*, 103: 24359–24372, 1998.
- [103] J. L. Hardebeck, K. R. Fetzer, and A. J. Michael. Improved tests reveal that the accelerating moment release hypothesis is statistically insignificant. *J. Geophys. Res.*, 113 B08310, 2008. doi: 10.1029/2007JB005410.
- [104] V. I. Keilis-Borok. The lithosphere of the earth as a nonlinear system with implications for earthquake prediction. *Rev. Geophys.*, 28:19–34, 1990.
- [105] V. I. Keilis-Borok and V. G. Kossobokov. Premonitory activation of earthquake flow–algorithm m8. *Physics of the Earth and Planetary Interiors*, 61(1-2):73–83, 1990.
- [106] V. G. Kossobokov and P. Shebalin. Earthquake prediction. In V. I. Keilis-Borok and A. A. Soloviev, editors, *Nonlinear Dynamics of the Lithosphere and Earthquake Prediction*, pages 141–207, Berlin, 2003. Springer-Verlag.
- [107] J. B. Minster and N. Williams. Systematic global testing of intermediate-term earthquake prediction algorithm. In P. Mora, editor, *1st ACES Workshop Proceedings*, Brisbane, 1999. GOPRINT.

- [108] J. B. Rundle, K. F. Tiampo, W. Klein, and J. S. S. Martins. Self-organization in leaky threshold systems: The influence of near-mean field dynamics and its implications for earthquakes, neurobiology, and forecasting. *Proc. Natl. Acad. Sci. U. S. A.*, 99:2514–2521: Suppl. 1, 2002.
- [109] J. R. Holliday, J. B. Rundle, K. F. Tiampo, and D. L. Turcotte. Using earthquake intensities to forecast earthquake occurrence times. *Nonlinear Processes in Geophysics*, 13:585–593, 2006.
- [110] J. B. Rundle, D. L. Turcotte, R. Shcherbakov, W. Klein, and C. Sammis. Statistical physics approach to understanding the multiscale dynamics of earthquake fault systems. *Rev. Geophys.*, 41(4):1019, 2003. doi: 10.1029/2003RG000135.
- [111] R. Shcherbakov, D. L. Turcotte, J. B. Rundle, K. F. Tiampo, and J. R. Holliday. Forecasting the locations of future large earthquakes: An analysis and verification. *Pure and Applied Geophysics*, 167(6-7):743–749, June 2010. doi: DOI10.1007/s00024-010-0069-1.
- [112] J. D. Zechar and T. H. Jordan. Testing alarm-based earthquake predictions. *Geophys. J. Int.*, 172:715–724, 2008. doi: 10.1111/j/1365-246X.2007.03676.x.
- [113] J. R. Holliday, K. Z. Nanjo, K. F. Tiampo, J. B. Rundle, and D. L. Turcotte. Earthquake forecasting and its verification. *Nonlinear Processes in Geophysics*, 12:965–977, 2005.
- [114] E. H. Field. Overview of the working group for the development of regional earthquake likelihood models (RELM). *Seis. Res. Lett.*, 78:7–16, 2007.
- [115] M. K. Savage and D. M. dePolo. Foreshock probabilities in the western great-basin eastern sierra nevada. *Seis. Soc. Am. Bull.*, 83:1910–1938, 1993.
- [116] A. Helmstetter and D. Sornette. Foreshocks explained by cascades of triggered seismicity. *J. Geophys. Rev.*, 108(B10):2457, 2003.
- [117] K. F. Tiampo, J. B. Rundle, S. McGinnis, S. J. Gross, and W. Klein. Eigenpatterns in southern California seismicity. *J. Geophys. Res.*, 107(B12):2354, 2002. doi: 10.1029/2001JB000562.
- [118] D. Schorlemmer, J. D. Zechar, M. J. Werner, E. H. Field, D. D. Jackson, and T. H. Jordan. First results of the regional earthquake likelihood models experiment. *Pure Ap. Geophys.*, 167:859–876, 2010.
- [119] P. A. Reasenberg. Second-order moments of central california seismicity 1969 - 1982. *J. Geophys Res.*, 90(5):479 – 495, 1985.

Michael Karl Sachs
June 2013
Graduate Program Name

Earthquake Scaling, Simulation and Forecasting

Abstract

Earthquakes are among the most devastating natural events faced by society. In 2011, just two events, the magnitude 6.3 earthquake in Christchurch New Zealand on February 22, and the magnitude 9.0 Tōhoku earthquake off the coast of Japan on March 11, caused a combined total of \$226 billion in economic losses [15]. Over the last decade, 791,721 deaths were caused by earthquakes [16]. Yet, despite their impact, our ability to accurately predict when earthquakes will occur is limited. This is due, in large part, to the fact that the fault systems that produce earthquakes are non-linear. The result being that very small differences in the systems now result in very big differences in the future, making forecasting difficult. In spite of this, there are patterns that exist in earthquake data. These patterns are often in the form of frequency-magnitude scaling relations that relate the number of smaller events observed to the number of larger events observed. In many cases these scaling relations show consistent behavior over a wide range of scales. This consistency forms the basis of most forecasting techniques. However, the utility of these scaling relations is limited by the size of the earthquake catalogs which, especially in the case of large events, are fairly small and limited to a few 100 years of events.

In this dissertation I discuss three areas of earthquake science. The first is an overview of scaling behavior in a variety of complex systems, both models and natural systems. The focus of this area is to understand how this scaling behavior breaks down. The second is a description of the development and testing of an earthquake simulator called Virtual California designed to extend the observed catalog of earthquakes in California. This simulator uses novel techniques borrowed from statistical physics to enable the modeling of large fault systems over long

periods of time. The third is an evaluation of existing earthquake forecasts, which focusses on the the Regional Earthquake Likelihood Models (RELM) test: the first competitive test of earthquake forecasts in California.